COMPARISON AND EXTENSION OF FREE DENDRITIC GROWTH MODELS THROUGH APPLICATION TO SILVER-15 MASS PERCENT COPPER ALLOY

A Thesis Presented

by

Selis Önel

to

The Department of Mechanical and Industrial Engineering

in partial fulfillment of the requirements for the
degree of

Doctor of Philosophy

in

Mechanical Engineering

in the field of

Materials Science and Engineering

Northeastern University
Boston, Massachusetts

July 2006

ProQuest Information and Learning Company
300 North Zeeb Road
P.O. Box 1346
Ann Arbor, MI 48106-1346

NORTHEASTERN UNIVERSITY

Graduate School of Engineering

Thesis Title: Comparison and Extension of Free Dendritic Growth Models Through Application to Ag-15 Mass % Cu Alloy

Author: Selis Önel

Department: Mechanical and Industrial Engineering

Approved for Thesis Requirement of the Doctor of Philosophy Degree

7/31/06

Thesis Advisor: Teiichi Ando — Date

7/31/06

Thesis Committee Member — Date

07/31/06

Thesis Committee Member — Date

Hameed M — 8/18/06

Department Chair: Hameed Metghalchi — Date

8/22/06

Director of the Graduate School: Yaman Yener — Date

Abstract

Modeling free dendritic growth in supercooled alloys is a critical requirement in controlling the microstructure of materials during rapid solidification processing of materials. Recent models developed to predict the growth of a dendrite in a highly supercooled melt adopt modifications that account for the interface kinetics and thermodynamics at high interface velocities, but the assumptions necessary to simplify the mathematical problem impose inherent restrictions. The assumption of straight phase boundaries adopted in early models often loses validity at high supercoolings, where phase boundaries are often curved. The use of equations with Henrian restrictions, such as the Baker-Cahn equation for the interfacial driving force and the Aziz equation for solute trapping confine these models to dilute solutions. Turnbull's collision-limited linear kinetic equation for interface growth may not apply to large interfacial driving forces. Therefore, a useful application and modification of free dendritic growth models require a thorough understanding of their limitations in producing consistent results.

One of the objectives of this research is to numerically compare the free dendritic growth models derived from the earlier LGK model developed by Lipton et al. The subsequent LKT model by Lipton et al., the TLK model by Trivedi et al., and the BCT model by Boettinger et al., together with a modification of the TLK model, and the DA model by DiVenuti and Ando are compared through application to an Ag-15 mass % Cu alloy. In addition, a new model to extend the DA model is developed by incorporating a thermodynamic solution model for the calculation of the interfacial driving force, thereby eliminating the Baker-Cahn equation that limits the use of the correct BCT and DA models to dilute solutions. Direct computation of the interfacial driving force by calculating a metastable phase diagram for the Ag-Cu system using a temperature dependent subregular solution model is carried out. Comparison of the results of the new model with the DA model confirms that the Baker-Cahn equation is applicable at low solute concentrations. As a future research direction, the new model can be extended to apply to higher concentration alloys by using a new solute trapping equation to further eliminate the dilute solution limitations.

Author: Selis Önel
Adviser: Teiichi Ando

Acknowledgements

First and foremost, I want to thank my thesis adviser Professor Teiichi Ando for giving me guidance and motivation during the course of my doctoral study. My experience from working with him and in his lab will be a torch lighting my future wherever I go. While teaching and advising, he has always imposed self-learning and hard working to reach excellence in research. I highly appreciate his endless efforts to create a family-like atmosphere in the multicultural environment of the Advanced Materials Processing Laboratory (AMPL) and, at the same time, to maintain the professional environment required to produce quality work in every aspect.

I would like to extend my gratitude to my thesis committee members, Professor Peter Wong of Tufts University and Professor Yung Joon Jung of Northeastern University for their constructive comments. I would also like to thank Professor Welville Nowak for his useful advise.

I am indebted to the Department of Mechanical and Industrial Engineering for providing the research and teaching assistantships throughout my doctoral studies. Being a TA has been a great experience of learning as well as teaching that I have tremendously enjoyed. I would like to thank the Department Chair Dr. Hameed Metghalchi and the Ex-Chair Dr. John Cipolla for all their support.

Without the great guidance and support from the Graduate School of Engineering, my studies would not have been possible and, therefore, it is my most enjoyable duty to present my thanks and sincere appreciation to the Director of Research and Graduate Studies, Dr. Yaman Yener.

I was lucky to work in a large research group. I would like to thank all the members of AMPL: My officemates Olga Bialiauskaya, Yuanwei Song and Hui Lu, my old friend from the American Collegiate Institute in İzmir and Middle East Technical University in Ankara İ. Emre Gündüz, my TA colleague Rajesh Ranganathan, and my lab-mates and friends Hiroki Fukuda, Suresh Kumar Pillai, Sudesna Roy and Gökçe Gülsoy for all their support. I am also grateful to AMPL visiting scholars Dr. Yoshinori Nishida and Dr. Kozo Nakazawa for very useful interactions and their friendship.

I am thankful to Dr. Bora Eryılmaz of Mathworks, Dr. A. Ümit Coşkun of Northeastern University, and Dr. Orhan Karslıgil of MIT and The Exeter Group for all the technical

discussions regarding computations with Matlab and other softwares.

My gratitude goes to all my friends at Northeastern University and in Boston. I have been very lucky to be surrounded by very wise, talented and gifted friends, whom I have been privileged to know: Feridun Özgören, the Director of the Cambridge Society for Turkish Music whom I highly respect, and each and every one of my chorus friends, who have become a part of my family and turned all the difficulties to soothing notes of music for me. I have inexplicable appreciation for Dr. Güliz Pamukoğlu, who has been there for me whenever I needed and has never hesitated to give her help and support even during her busiest and physically most difficult times.

My sincere thanks goes to all the members of my family back in Türkiye, who have always thought of me, missed me, and prayed for me. I am grateful to M. Berker Evren, who has made his way to the USA with me and has run in the PhD marathon with me. The start and the course of this thesis have made great impacts and its successful completion has definitely taken its place as an important milestone in our lives.

Table of Contents

Abstract 1

Acknowledgements 2

Table of Contents 6

List of Tables 7

List of Figures 8

1 Introduction 11
- 1.1 Research Background 11
- 1.2 Free Dendritic Growth: Overview 12
- 1.3 Overview of Free Dendritic Growth Models and Their Limitations 13
- 1.4 Research Objectives and Methodology 16
- 1.5 Overview of Thesis 18

2 Literature Review of Selected Models 20
- 2.1 Early Models 21
  - 2.1.1 Ivantsov's Analytic Solution for a Binary Alloy 21
  - 2.1.2 LGK Model, 1984 and 1987 25
- 2.2 Later Models 32
  - 2.2.1 LKT Model, 1987 32
  - 2.2.2 TLK Model, 1987 34
  - 2.2.3 BCT Model, 1988 36
- 2.3 Modifications to the Later Models 42
  - 2.3.1 A Modified TLK Model Adopting a Kinetic Liquidus 43

2.3.2 An Extended BCT Model Employing Curved Phase Boundaries: DA Model . . . 51

3 Thermodynamic Calculations 54
3.1 Background . . . 55
3.2 The Ag-Cu System . . . 56
3.3 Phase Diagram Calculation Methods . . . 58
3.4 Application of a Thermodynamic Solution Model to the Ag-Cu System . . 60
3.4.1 Metastable Phase Diagram Calculated by Murray . . . 60
3.4.2 Computation of the Ag-Cu Metastable Phase Diagram . . . 65
3.5 Results and Discussion . . . 68

4 Comparative Computation with Models 74
4.1 Computation Scheme . . . 75
4.2 Numerical Computation Method . . . 83
4.3 Comparison and Analysis of Computation Results . . . 87
4.3.1 General Behavior of Solidification Parameters with Total Melt Supercooling . . . 88
4.3.2 Transition Region . . . 94
4.3.3 Effects of Solute Trapping . . . 95
4.3.4 Effects of Curved Phase Boundaries versus Straight Phase Boundaries 96
4.3.5 Effects of Linear Kinetics and Thermodynamic Driving Force at the Interface . . . 100

5 A Modification of the DA Model 102
5.1 Background for Development of the Model . . . 102
5.2 Modification Scheme . . . 105
5.3 Calculation of the Interfacial Driving Force . . . 107
5.4 Computation Results and Comparison With Those From the BCT and DA Models . . . 110

6 A Review of Models for Solute Trapping 127

7 Conclusions 136

8 Future Research Direction 140

Appendices 142

A Formulation of the Excess Free Energy 143

A.1 Using Free Energy Interaction Coefficients 146
A.2 Using Polynomial Coefficients 148

B Phase Boundary Equations **153**
B.1 Verification of the Temperature Dependent Subregular Solution Model . . . 153
B.2 Derivation of the Phase Boundary Equations Using the Temperature Dependent Subregular Solution Model 155

C Ivantsov Equation Approximation **159**

D Nomenclature **161**

References **169**

List of Tables

3.1 Properties of Ag and Cu atoms 57
3.2 Comparison of the Thermodynamic Functions of Solution Models 60
3.3 Interaction Parameters Calculated by Murray 64

5.1 Free Dendritic Growth Models for a Paraboloidal Tip 104

List of Figures

2.1 Equilibrium phase diagram as used by the LGK model. 26

3.1 Calculated metastable phase diagram of Ag-Cu alloy system using a temperature dependent subregular solution model. 70
3.2 Calculated Gibbs free energies for the Ag-Cu system at the eutectic temperature 1052.1 K 71
3.3 Calculated Gibbs free energies for the Ag-Cu system below the eutectic temperature at 900 K 72
3.4 Calculated Gibbs free energies for the Ag-Cu system above the eutectic temperature at the melting temperature of Ag at 1234 K 72
3.5 Calculated Gibbs free energies for the Ag-Cu system above the eutectic temperature at the melting temperature of Cu at 1358 K 73
3.6 Calculated Gibbs free energies for the Ag-Cu system above the melting temperatures of Ag and Cu at 1500 K 73

4.1 Simple flowchart of the computer program for the free dendritic growth models. 85
4.2 Multiple root region showing a jump bifurcation. 86
4.3 Results of free dendritic growth calculations showing the variation of the interface velocity with melt supercoling for Ag-15 mass % Cu. 89
4.4 Results of free dendritic growth calculations showing the variation of the tip radius with melt supercooling for Ag-15 mass % Cu. 90
4.5 Results of free dendritic growth calculations showing the variation of the interface temperature with melt supercoling for Ag-15 mass % Cu. 91
4.6 Results of free dendritic growth calculations showing the variation of the interface concentrations of the liquid and the solid with melt supercoling for Ag-15 mass % Cu. 92
4.7 Results of free dendritic growth calculations showing the variation of the solute partition coefficient with melt supercooling for Ag-15 mass % Cu. . . 93

4.8 Ag-rich part of the Ag-Cu metastable phase diagram showing curved and straight liquidus and solidus. 97
4.9 Comparison of the BCT and DA model solutions with respect to the curved and straight liquidus and solidus on the Ag-rich part of the Ag-Cu metastable phase diagram. 99

5.1 Flowchart showing the computation of the new model with the modification for the interfacial free energy calculation. 112
5.2 Molar Free energy curves for the liquid and solid phases at T^* showing the interfacial free energy ΔG^*. 113
5.3 Part of the free energy curves given in Figure 5.2 showing the calculation of the interfacial free energy ΔG^*. 114
5.4 Results of free dendritic growth calculations showing the variation of interface velocity with total supercooling for Ag-15 mass % Cu. 115
5.5 Results of free dendritic growth calculations showing the variation of tip radius with total supercooling for Ag-15 mass % Cu. 116
5.6 Results of free dendritic growth calculations showing the variation of partition coefficient with total supercooling for Ag-15 mass % Cu. 117
5.7 Results of free dendritic growth calculations showing the variation of interface solid and liquid concentrations with total supercooling for Ag-15 mass % Cu. 118
5.8 Results of free dendritic growth calculations showing the variation of interface temperature with total supercooling for Ag-15 mass % Cu. 119
5.9 Comparison of the new model with the BCT and DA models on the Ag-Cu phase diagram. 120
5.10 Comparison of the new model with the BCT and DA models with respect to the variation of interfacial molar free energy with total supercooling for Ag-15 mass % Cu. 121
5.11 Comparison of the new model with the BCT and DA models with respect to the variation of interfacial molar free energy with interface temperature for Ag-15 mass % Cu. 122
5.12 Comparison of the new model with the BCT and DA models with respect to the variation of interface concentration of the liquid with interfacial free energy for Ag-15 mass % Cu. 123
5.13 Comparison of the new model with the BCT and DA models with respect to the variation of interfacial free energy with interface concentrations of the liquid and the solid for Ag-15 mass % Cu. 124
5.14 Comparison of the BCT and DA models with the new model with respect to the variation of interface concentration of the liquid and the solid with the absolute value of interfacial free energy for Ag-15 mass % Cu. 125

5.15 Comparison of the BCT and DA models with the new model with respect to the variation of partition coefficient with the absolute value of interfacial free energy for Ag-15 mass % Cu. 126

6.1 Schematic diagram of the mass balance at the solid-liquid interface. 129
6.2 Schematic diagram of solid-liquid interface energy on the configurational coordinates for stepwise growth (Reproduced from Aziz). 131

Chapter 1

Introduction

1.1 Research Background

The dendritic growth of crystals into a supercooled melt is a common form of solidification in droplets in a thermal spray. A dendrite is a crystal that typically develops with a multi-branching tree-like morphology. Dendritic morphologies arise when materials solidify under conditions that make plane-front solidification unstable. Dendritic microstructures may be observed in powders and ribbons made by rapid solidification processing as well as in ingots and welds made by conventional processing methods [1]. High supercooling makes it possible to produce finer microstructures with desired phases. The properties and quality of the solidified material and the final product depend on the microstructure that forms during the solidification process. Consequently, a better understanding of crystal growth is crucial in predicting and controlling the microstructure in the solidification processing of advanced materials.

An essential requirement for a dendritic growth model is the ability to predict the size, growth rate and chemical composition of a dendrite growing in a supercooled liquid as these characteristics largely determine the solidification microstructure, and hence, the properties of a solidified material. Most of the current free dendritic growth models [2, 3, 4, 5], however, inherit shortcomings originating from early models developed for slow solidification, and as such are limited to low supercooling and/or dilute solution conditions.

1.2 Free Dendritic Growth: Overview

Most solidification models developed to date are for the prediction of free dendritic crystallization in which a melt, cooled below its equilibrium solidification temperature, solidifies dendritically due to capillary instability [6, 7, 8]. The dynamics involved in the advancement of the solidification front in an alloy melt are more complex than those involved in a pure material due to the occurrence of solutal supercooling (constitutional supercooling) ahead of the solid-liquid interface.

During free dendritic growth in an alloy melt, dendrites proceed by releasing heat and rejecting the solute into the supercooled liquid. The released heat is conducted away from the solid-liquid interface through the liquid. The rejected solute accumulated in the liquid ahead of the interface must also be removed by diffusion in the liquid. The solid-liquid interface gets supercooled below the liquidus temperature by the amount determined by the curvature of the solidification front, the diffusion of latent heat of solidification from the solid to the liquid, and the rejection of the solute into the alloy melt.

The recent models stress the inclusion of the kinetic component in addition to the curvature, thermal, and solutal effects. The kinetic term occurs at high supercoolings due to the high interface velocity and the limited atom mobility for rearrangement at the interface. Depending on the amount of supercooling at the solid-liquid interface and the resultant interface velocity, the relative contributions of the four supercooling components to the total supercooling may drastically vary.

1.3 Overview of Free Dendritic Growth Models and Their Limitations

Typically, a free dendritic growth model predicts the radius of curvature at the dendrite tip, r, and the interface velocity, V, given an alloy composition, C_0, and a total bath supercooling, ΔT. The interface temperature, T^*, needs to be calculated simultaneously with the velocity and radius. The solute concentration of the liquid at the interface, C_L^*, and the solute partition coefficient, k, depend on the interface temperature and velocity. At low supercoolings, the interface concentrations will be close to the local thermodynamic equilibrium concentrations defined by the liquidus and solidus. Therefore, it is appropriate to assume local equilibrium conditions for such cases. On the other hand, for higher values of supercooling, where the dendrite tip attains a high growth rate into the liquid, there will not be sufficient time for atom rearrangement to maintain local equilibrium concentrations at the interface. Therefore, the interface concentrations will deviate from the equilibrium values defined by the solidus and liquidus. The nonequilibrium interfacial concentrations will be determined by the dynamic conditions at the solid-liquid interface, depending on the interfacial driving force and the mobility of the atoms.

The free dendritic growth models discussed in this study are inspired by the earlier model developed by Lipton, Glicksman and Kurz in 1984 [9]. The LGK model depends on Ivantsov's exact solution for heat and mass transfer during crystal growth in a supercooled melt [10, 11, 12]. It addresses the thermal and solutal supercoolings that occur at the dendrite tip from Ivantsov's treatment of a paraboloid of revolution geometry, and the curvature supercooling at the tip from Gibbs-Thomson's treatment of a spherical surface [13]. The LGK model assumes local equilibrium conditions at the solidification front and adopts a morphological stability criterion [14, 13] along with the equation for the total supercooling to predict the radius of curvature and velocity at the tip. The interface temperature is found through solving the thermal and mass diffusion equations separately at the interface with no inclusion of interface thermodynamics. LGK, also, published a dimensionless version of their model in 1987 [15].

The models succeeding the LGK model added modifications to this model to make it applicable to high supercoolings and growth rates. Among these models, the LKT model, developed by Lipton, Kurz, and Trivedi [2], is regarded as still assuming local equilibrium interface conditions as the interface kinetics are omitted in accordance with the stability criterion [16] applied. The TLK model, subsequently developed by the same authors, Trivedi, Lipton, and Kurz [3], included the effect of interface kinetics through a growth rate dependent partition coefficient, but neglected the kinetic effects on the total supercooling as done in the LKT model. The omission of the kinetic supercooling, however, necessitates the use of the equilibrium interfacial composition for the liquid as the interface temperature and velocity that determine the liquid composition do not reflect any kinetic effects.

Boettinger, Coriell and Trivedi [4] modified the LGK model to include nonequilibrium interface conditions. This model is referred to as the BCT model and differs from the LKT and TLK models as it correctly addresses the nonequilibrium interface kinetics. The BCT model introduces an interfacial driving force for dendritic growth, correctly relates it to the interface velocity and includes a kinetic supercooling component in the total supercooling. The interfacial driving force for dendritic growth, ΔG^*, is given by the Baker and Cahn expression, which is restricted to Henrian dilute solutions [17, 18]. The BCT model assumes straight phase boundaries as done in the previous models and defines a nonequilibrium liquidus slope which comes from the use of the Baker-Cahn equation in the collision-limited linear kinetic equation given by Turnbull [19]. Even though the nonequilibrium liquidus slope is a kinetic slope, not intended to replace the equilibrium slope, in some studies it has been misinterpreted and used in the equations that require the equilibrium values [20, 21, 22].

The DA model, developed by DiVenuti and Ando [5], modifies the BCT model successfully by incorporating curved phase boundaries in formulating the interfacial driving force in accordance with the procedure of the BCT model. The DA model defines the total supercooling with four components addressing the kinetic component correctly. In addition, it shows the stability criterion given by Trivedi and Kurz [16] to apply to the dendritic growth in a system with curved phase boundaries, even at a high supercooling, where the kinetic component is significantly large.

The free dendritic growth models discussed above that succeed the earlier LGK model are applicable only to the case of very dilute alloys due to the modifications added to extend the LGK model to apply to high growth rates. Each of these models employs a stability criterion that determines the morphological stability of the solid-liquid interface. Modification of the free dendritic growth models to account for nonequilibrium interfacial conditions is an elaborate task and needs to be done in a manner consistent with the derivation of the model.

1.4 Research Objectives and Methodology

One of the objectives of this doctoral study is to computationally compare the free dendritic growth models and show how some of the restrictions of these models may be removed. The current free dendritic growth models and their modified versions are examined based on the discussions provided by Ando [23]. Models designed for high supercooling conditions are applied to a Ag-15 mass % Cu alloy to provide numerical comparison of the models and their modifications. In addition, an extension of the DA model is developed by incorporating a thermodynamic solution model, also developed in this study, for the calculation of the driving force at the dendrite tip, thereby, eliminating the Henrian restriction of the Baker-Cahn equation that limits the use of the BCT and DA models to dilute solutions. The following order is followed to proceed:

- Verification and comparison of the free dendritic growth models developed for high supercoolings and interface velocities, namely the LKT, TLK, BCT, DA models and others that are referred to in this study as modified TLK models based on the discussions provided by Ando [23]
- Employing an appropriate thermodynamic solution model to calculate the metastable phase diagram for the Ag-Cu system
- Application of the existing free dendritic growth models developed for high supercoolings to a Ag-15 mass % Cu alloy and comparison of the computed results
- Further development of a free dendritic growth model that incorporates a thermodynamic solution model to calculate the interfacial driving force, ΔG^*, rather than using the Henrian condition-limited Baker-Cahn equation
- Discussion of the dilute solution limitation associated with the use of the Aziz equation for solute trapping as a future research direction

1.5 Overview of Thesis

This doctoral thesis, based on the purpose of computationally comparing and extending the free dendritic growth models, starts with an introduction to the theory of free dendritic growth and an overview of the current models with their limitations. It continues with a critical literature review of selected free dendritic growth models. In that respect, Chapter 2 starts with the formulation of Ivantsov's exact solution for a binary alloy and the early LGK model, which serves as the basis of the successive models modified for high growth rates. Studying the early models is useful in understanding the modifications in the subsequent models as well as in verifying the validity of the modifications with the theories and equations involved. Chapter 2 outlines the formulation and the basic equations of the current LKT, TLK, BCT models and their modified versions including a modified TLK model and the DA model, also, providing a discussion for their shortcomings.

One of the goals of this study is to apply the models to the same alloy for computational comparisons. For this purpose, a Ag-15 mass % Cu alloy is selected and the thermodynamic calculations related to this system to obtain a metastable phase diagram are presented in Chapter 3. The metastable phase diagram is especially required for the DA model that employs curved phase boundaries. The existing models and their modified versions are applied to the same alloy over a range of high supercoolings. Chapter 4 presents the formulation and methodology used computational comparisons of the free dendritic growth models as well as the computation results.

A new model, which is an extension of the DA model, is presented in Chapter 5. This model adopts a thermodynamic solution model to calculate the interfacial driving force and, therefore, highly depends on the thermodynamic calculations presented in Chapter 3. Chapter 5 also shows the modification scheme for the new model and addresses the direct calculation of the interfacial driving force. The computation results for this model are compared with those of the DA and BCT models that employ the Baker-Cahn equation for the interfacial driving force.

After a brief review of the recent models for solute trapping, the conclusion chapter provides an overview of the thesis and summary of all the discussion and results obtained from dendritic growth models. The thesis ends with suggestions for future directions for improving the dendritic growth models to apply to solutions of all ranges of composition by further eliminating the Henrian restrictions that arise from the use of the Aziz solute trapping equation and the collision-limited linear kinetic law of Turnbull adopted in the BCT and DA models. All the necessary data, formulation, or information related to the calculations presented in this thesis are given in the appendices.

Chapter 2

Literature Review of Selected Free Dendritic Growth Models

The dendritic growth of crystals in supercooled melts has long been receiving the attention of scientists. Exact solutions to the thermal balance equations for free dendritic growth of pure materials for various geometries was presented by Ivantsov in 1947 [10]. These solutions include only the thermal supercooling due to the heat diffusion into the melt.

The dynamics involved in the enhancement of the solidification front in an alloy melt are more complex than those involved in a pure material due to the inclusion of solutes and their accumulation ahead of the interface, which causes the solutal supercooling of the interface. Free dendritic growth in an alloy melt occurs with latent heat release and solute rejection into the supercooled liquid.

The exact solutions of Ivantsov [11, 12, 24] for various geometries extended to binary alloys have been used to solve for the thermal and solutal supercooling components.

An early model by Lipton et al. [9] uses Ivantsov's treatment together with the Gibbs-Thomson supercooling of the curved interface and a marginal stability criterion for tip radius. Yet, addressing the heat and mass transport phenomena alone is not enough to understand and solve the problem. It is necessary to, also, include the interfacial thermodynamics and kinetics especially for high supercooling conditions, where high growth rates may be achieved.

The current free dendritic models discussed in this thesis, all inspired by the earlier models, are intended to apply to high growth rates, but with some restrictions and, even, inconsistencies in some of the models. The following sections will present a review of the early and the current models together with their modifications.

2.1 Early Models

2.1.1 Ivantsov's Analytic Solution for a Binary Alloy

The Ivantsov solution for a needle-like crystal is an exact solution of heat and mass transport equations obtained for an interfacial geometry represented by a paraboloid of revolution [10, 11, 12]. The isothermal and isosolutal interface is assumed to migrate into a uniformly supercooled homogeneous binary melt at a constant rate, V, and a constant temperature, T^*. Given the alloy composition C_0, the melt temperature T_∞ (or the total bath supercooling ΔT), and an equation relating the interface solid and liquid concentrations, the Ivantsov solution can be used to find the interface temperature T^*, the corresponding interface concentrations C_S^* and C_L^* and a product of the tip velocity and radius Vr. For a given set of physical properties, this solution shows that dendrites can grow with sharp tips at high rates or with blunt tips at low rates as the product Vr is constant.

In Ivantsov's treatment, the transport equations are obtained through solving the steady state heat and mass transfer equations for the paraboloidal tip. Stationary conditions are assumed while the coordinate frame at the needle tip moves with a constant velocity along the axis of revolution into an infinitely large melt. The system is axisymmetric making the equations independent of the angular axis θ. Diffusion is assumed to be the dominant transport mechanism while the convective effects are neglected. The thermal and solutal diffusion phenomena are assumed to be independent. The density and thermal conductivity of the solid and the liquid are assumed to be constant and independent of temperature and position.

In the solid, the temperature and concentration gradients are assumed to be negligible as heat and mass diffusion in the solid are neglected due to the relatively smaller diffusion coefficient of the solid. At the interface, the temperatures of the solid and the liquid are the same defining the interface temperature, whereas the solute concentration of the solid and the liquid are related through an equation such that $C_S^* = f(C_L^*)$. In the liquid, the energy and mass transport equations on the cylindrical coordinates (ρ, θ, ζ) are given by:

$$-\frac{V}{\alpha}\frac{\partial T_l}{\partial \zeta} = \frac{\partial^2 T_l}{\partial \rho^2} + \frac{1}{\rho}\frac{\partial T_l}{\partial \rho} + \frac{\partial^2 T_l}{\partial \zeta^2} \tag{2.1}$$

and

$$-\frac{V}{D}\frac{\partial C_l}{\partial \zeta} = \frac{\partial^2 C_l}{\partial \rho^2} + \frac{1}{\rho}\frac{\partial C_l}{\partial \rho} + \frac{\partial^2 C_l}{\partial \zeta^2} \tag{2.2}$$

respectively, where T_l and C_l are the temperature and concentration profiles in the liquid, V is the growth rate along the ζ axis, α is the thermal diffusion constant of the liquid and D is the mass diffusion constant of the liquid.

The boundary conditions in the liquid at an infinitely large distance from the tip, where $\rho = \infty$ and $\zeta = \infty$, are given as $C_l = C_\infty$ and $T_l = T_\infty$. Ivantsov describes the location of the interface in the growth direction by a parameter g. In this treatment, the surface of the paraboloid of revolution is always located at $g = 1$, where $g < 1$ indicates the solid and $g > 1$ indicates the melt. Consequently, at the interface or at the needle tip, $g = 1$.

In the solid, for $g < 1$, the temperature and concentration distributions, obtained from the same transport equations used for the liquid as shown in equations (2.1) and (2.2), reduce to

$$T_s = T^* \tag{2.3}$$

and

$$C_s = C_S^* \tag{2.4}$$

where T_s and C_s represent the temperature and concentration profiles in the solid.

In the liquid, for $g > 1$, the temperature and concentration distributions from the above transport equations are given by

$$\frac{T_l - T_\infty}{T^* - T_\infty} = \frac{E_i\left(-\frac{Vr}{2\alpha}g\right)}{E_i\left(-\frac{Vr}{2\alpha}\right)} \tag{2.5}$$

and

$$\frac{C_\infty - C_l}{C_\infty - C_L^*} = \frac{E_i\left(-\frac{Vr}{2D}g\right)}{E_i\left(-\frac{Vr}{2D}\right)} \tag{2.6}$$

where

$$g = \frac{\zeta}{r} + \sqrt{\left(\frac{\rho}{r}\right)^2 + \left(\frac{\zeta}{r}\right)^2} \tag{2.7}$$

Since the transport equations considered for both heat and mass transfer are similar, their solutions are also similar as shown above. Using the boundary conditions Ivantsov's treatment gives the dimensionless thermal supercooling

$$\Omega_t = \frac{c_p(T^* - T_\infty)}{\Delta H_f} = -\frac{Vr}{2\alpha}e^{\frac{Vr}{2\alpha}}E_i\left(\frac{Vr}{2\alpha}\right) \tag{2.8}$$

and the dimensionless supersaturation

$$\Omega_c = \frac{C_0 - C_L^*}{C_S^* - C_L^*} = -\frac{Vr}{2D}e^{\frac{Vr}{2D}}E_i\left(\frac{Vr}{2D}\right) \tag{2.9}$$

where c_p is the molar heat capacity and ΔH_f is the molar enthalpy of fusion. E_i is an exponential integral function and it is defined by:

$$E_i(P) = -\int_{-P}^{\infty} \frac{e^{-z}}{z} dz \tag{2.10}$$

The terms on the right hand side of Equations 2.8 and 2.9 give the Ivantsov function, $I_v(P)$, defined by

$$I_v(P) = -Pe^P E_i(P) \tag{2.11}$$

The dimensionless thermal supercooling and the dimensionless supersaturation are used to define the thermal and solutal supercooling, ΔT_t and ΔT_c, as a function of the Péclet number. The Péclet number is a dimensionless function that represents the ratio of a characteristic dimension of the system to the diffusion distance [6]. In the case of thermal diffusion, the thermal Péclet number, P_t, is defined by

$$P_t = \frac{Vr}{2\alpha} \tag{2.12}$$

and in the case of solutal diffusion, the solutal Péclet number, P_c, is defined by

$$P_c = \frac{Vr}{2D} \tag{2.13}$$

The following free dendritic growth models depend on Ivantsov's treatment of a paraboloidal dendrite tip to find the thermal and solutal supercooling components of the total bath supercooling. An early model discussed in this study, the LGK model, adds another equation for the tip radius from a morphological stability criterion.

2.1.2 LGK Model, 1984 and 1987

The LGK model [9, 15], developed and nondimensionalized by Lipton, Glicksman and Kurz (LGK), does not address the thermodynamic driving force at the solid-liquid interface.

It applies only to small Péclet number conditions as it assumes local equilibrium at the solid-liquid interface, i.e., the dendrite tip. The total supercooling, ΔT, as shown in Figure 2.1, is defined as the sum of the thermal, solutal and curvature supercoolings.

$$\Delta T = \Delta T_t + \Delta T_c + \Delta T_r = T_L(C_0, r = \infty) - T_\infty \tag{2.14}$$

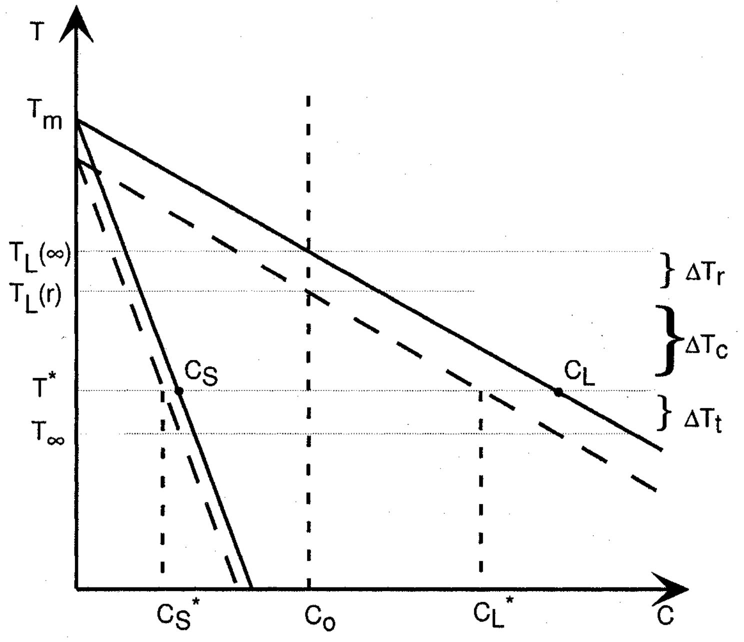

Figure 2.1: Equilibrium phase diagram as used by the LGK model.

LGK define the thermal supercooling, ΔT_t, as the difference between the interface temperature and the melt temperature far from the tip, i.e.,

$$\Delta T_t = T^* - T_\infty \tag{2.15}$$

ΔT_t is calculated from Ivantsov's solution for dimensionless thermal supercooling

$$\Omega_t = \frac{c_p(T^* - T_\infty)}{\Delta H_f} = I_v(P_t) \tag{2.16}$$

and is given by:

$$\Delta T_t = \frac{\Delta H_f}{c_p} I_v(P_t) = f(V, r) \tag{2.17}$$

The solutal supercooling, ΔT_c, is defined as the difference between the liquidus temperature of a curved interface (with tip radius r) in a melt with composition C_0 and the liquidus temperature at the interface given by:

$$\Delta T_c = T_L(r, C_0) - T^* \tag{2.18}$$

By assuming straight phase boundaries and local equilibrium conditions at the interface, the above relation for ΔT_c is written as

$$\Delta T_c = m_L(C_0 - C_L^*) \tag{2.19}$$

where m_L is the liquidus slope. C_L^* is calculated by recalling Ivantsov's dimensionless supersaturation, $\Omega_c = I_v(P_c)$, defined as:

$$\Omega_c = \frac{C_L^* - C_0}{C_L^* - C_S^*} = I_v(P_c) \tag{2.20}$$

and by using the equilibrium partition coefficient k_0 defined as:

$$k_0 = \frac{C_S^*}{C_L^*} \tag{2.21}$$

The dimensionless supersaturation shown in Equation (2.20) is rewritten as

$$\frac{C_L^* - C_0}{C_L^*(1 - k_0)} = I_v(P_c) \tag{2.22}$$

from which the interface solute concentration of the liquid, C_L^*, is pulled out to give:

$$C_L^* = \frac{C_0}{1 - (1 - k_0)I_v(P_c)} \tag{2.23}$$

With Equation (2.23), the solutal supercooling defined in Equation (2.19) is rewritten to involve the Ivantsov function as

$$\Delta T_c = C_0 m_L \left[1 - \frac{1}{1 - (1 - k_0)I_v(P_c)}\right] \tag{2.24}$$

The third term making up the total supercooling defined in the LGK model is the curvature supercooling, ΔT_r, which is given by:

$$\Delta T_r = K\Gamma \tag{2.25}$$

ΔT_r is the supercooling caused by the excess energy of the solid-liquid interface, which is convex toward the liquid. It is also called the Gibbs-Thomson supercooling [13]. Γ is the Gibbs-Thomson coefficient and is defined as the ratio of the solid-liquid interface energy, γ, to the entropy of melting per unit volume, ΔS_f, and is given by:

$$\Gamma = \frac{\gamma}{\Delta S_f} \tag{2.26}$$

For most metals, Γ is of the order of 10^{-7} K·m. The LGK model assumes Γ to be constant and equal to 6.62x10^{-8} K·m for succinonitrile-acetone mixtures. The curvature, K, is defined with the principal radii of the curved surface as

$$K = \frac{1}{r_1} + \frac{1}{r_2} \tag{2.27}$$

For a paraboloidal tip, $r_1 = r_2 = r$, thus, the curvature supercooling is given by:

$$\Delta T_r = \frac{2\Gamma}{r} \tag{2.28}$$

Adding up the three supercooling terms, the total bath supercooling defined in the LGK model is written as:

$$\Delta T_{LGK} = \frac{\Delta H_f}{c_p} I_v(P_t) + C_0 m_L \left[1 - \frac{1}{1-(1-k_0)I_v(P_c)}\right] + \frac{2\Gamma}{r} \tag{2.29}$$

Combination of the thermal, solutal and curvature supercoolings gives only one equation, the total supercooling equation, that has two variables, namely the interface velocity V and the tip radius r. In need of a second equation, the LGK model adopts a marginal stability criterion for the dendrite tip given by Trivedi [14] and Kurz and Fisher [13] instead of extremum conditions. This stability criterion depends on the morphological relation given by Langer and Müller-Krumbhaar [25, 26, 27, 28], which states that the tip radius, r, is equal to the shortest wavelength of perturbation, λ, that keeps the perturbed interface stable.

The marginal stability criterion discussed by Trivedi [14] and Kurz and Fisher [13] expresses the shortest wavelength λ, namely the tip radius, as a function of the concentration and temperature gradients at the solid-liquid interface and defines it as:

$$\lambda = r = \left[\frac{\Gamma}{\sigma^*(m_L G_c - G)}\right]^{\frac{1}{2}} \tag{2.30}$$

where G_c and G represent the concentration gradient in the liquid and the conductivity-weighted average temperature gradient ahead of the tip, respectively. The concentration and temperature gradients in the solid are assumed to be zero and the thermal conductivities of the solid and the liquid are assumed to be the same. λ is a function of both V and r through dependency of G_c and G on the Péclet number.

The LGK model is presented in two papers, one in 1984 [9] and the other in 1987 [15]. The former study uses half of the G_c in Equation (2.30) in order to match the resulting equation for the radius with that presented by Langer and Müller-Krumbhaar [26] for the pure substance case. The latter work uses the actual G_c and the same mean temperature gradient, G, to get the equation for r. The concentration and temperature gradients are functions of the Péclet number given as

$$G_c = \frac{\partial C}{\partial x} = f(P_c) = f(V, r) \tag{2.31}$$

and

$$G = \frac{\partial T}{\partial x} = f(P_t) = f(V, r) \tag{2.32}$$

The variable, r, is obtained by substituting the gradients in Equation (2.30), which gives:

$$r = \frac{\Gamma}{\sigma^*}\left[\frac{\Delta H_f}{c_p}P_t - \frac{2m_L C_0(1-k_0)P_c}{1-(1-k_0)I_v(P_c)}\right] \tag{2.33}$$

In the second paper [15], LGK normalize their model by defining the nondimensional parameter and function, A and $F(A)$, where A represents the ratio of the interface solute concentration in liquid to the alloy composition, C_L^*/C_0. It is a function of the solutal Péclet number and the equilibrium partition coefficient , and is given by:

$$A = \frac{1}{1-(1-k_0)I_v(P_c)} \tag{2.34}$$

$F(A)$ is a stability function as it is equal to $1-m_L G_c/G$ from the extreme velocity criterion and is given by:

$$F(A) = 1 - 2m_L \frac{C_0}{\Theta}\frac{\alpha}{D}A(1-k_0) \tag{2.35}$$

where Θ represents $\Delta H_f/c_p$. LGK transform all the terms into nondimensional forms by normalizing them in such a way that the normalized thermal supercooling would be equal to $I_v(P_t)$.

In their study [9, 15], LGK used an iterative method to solve Equations (2.29) and (2.33) for V and r over a range of compositions of acetone and succinonitrile, C_0, for total melt supercoolings, ΔT, of 0.5 K and 0.9 K. The LGK model applies only to low supercoolings, where the interface advances at a low Péclet number due to the omission of interface kinetic effects. The later models discussed in this study are developed with an intention to modify the LGK model for high supercoolings and growth rates, i.e., large Péclet number conditions, by applying a stability criteria suitable for high interface velocities to determine the radius of the dendrite tip.

2.2 Later Models

2.2.1 LKT Model, 1987

The LKT model developed by Lipton, Kurz and Trivedi (LKT) [2] is an extension of the LGK model developed in need for a model to predict crystal growth at high supercoolings. The LKT model introduces a marginal stability criterion given by Trivedi and Kurz [16]. This marginal stability criterion is an extension of the Mullins-Sekerka criterion [29] to make it applicable to high thermal Péclet numbers and is given by:

$$-\Gamma\omega^2 - (\overline{K}_l G_l \xi_l + \overline{K}_s G_s \xi_s) + m_L G_c \xi_c = 0 \tag{2.36}$$

where Γ is the Gibbs-Thomson coefficient, m_L is the liquidus slope, and ω is the wave number of the perturbation on the interface, which is equal to $2\pi/\lambda$. $\overline{K}_l$ and $\overline{K}_s$ represent the dimensionless thermal conductivity of the solid and liquid and are shown by $\frac{K_l}{K_s+K_l}$ and $\frac{K_s}{K_s+K_l}$, respectively, where K_s and K_l are the thermal conductivities of the solid and the liquid. G_l and G_s are the thermal gradients in the liquid and the solid and G_c is the concentration gradient in the liquid, all defined at the interface in the above equation. ξ_l and ξ_s are the thermal stability parameters for the liquid and the solid and ξ_c is the solutal stability parameter for the liquid.

The LKT model adopts the Trivedi-Kurz criterion [16] to an isothermal tip assuming equal thermal diffusivity and conductivity in the liquid and the solid. The tip radius is then given by

$$r = \frac{\Gamma}{\sigma^*(m_L G_c \xi_c - G\xi_t)} \tag{2.37}$$

where

$$\xi_c = 1 + \frac{2k_0}{1 - 2k_0 - \sqrt{1 + \frac{1}{\sigma^* P_c^2}}} \tag{2.38}$$

and

$$\xi_t = 1 - \frac{1}{\sqrt{1 + \frac{1}{\sigma^* P_t^2}}} \tag{2.39}$$

LKT use the dimensionless parameter and function, A and $F(A)$, defined in the LGK model in Equations (2.34) and (2.35), respectively, to simplify their equations. As described in the previous section, A represents the ratio of the interface solute concentration in liquid to the alloy composition, C_L^*/C_0. The stability function $F(A)$ becomes equal to $\xi_t - \xi_c m_L G_c/G$ with the introduction of the Trivedi-Kurz marginal stability criterion and is more explicitly given by

$$F_{LKT}(A) = \xi_t - 2\xi_c m_L \frac{C_0}{\Theta}\frac{\alpha}{D} A(1 - k_0) = F_2(A) \tag{2.40}$$

Despite the intention to apply the model to high growth rates, the LKT model fails to address the nonequilibrium interface kinetics and continues to assume local equilibrium at the interface. The total bath supercooling, ΔT, consists of the three terms that were shown in the LGK model in Equation (2.29) and is given by:

$$\Delta T_{LKT} = \Delta T_t + \Delta T_c + \Delta T_r \tag{2.41}$$

or

$$\Delta T_{LKT} = \frac{\Delta H_f}{c_p} I_v(P_t) - m_L C_0 \left[\frac{1}{1-(1-k_0)I_v(P_c)} - 1 \right] + \frac{2\Gamma}{r} \tag{2.42}$$

As shown in Equation (2.42), the total supercooling defined in the LKT model is composed of the thermal, solutal and curvature supercoolings and is not different from Equation (2.29), the total supercooling equation proposed in the LGK model.

2.2.2 TLK Model, 1987

The TLK model modifies the LKT model to solve the problem of free dendritic growth into a highly supercooled melt. In order to deal with the high growth rates due to high supercoolings, the TLK model accommodates the Trivedi-Kurz stability criterion as in the LKT model and a growth-rate dependent nonequilibrium partition coefficient, k, developed by Aziz [30]. This expression is referred to as the Aziz equation. It was obtained by combining the reaction rate theory to explain the nonequilibrium kinetics and the phase transformation thermodynamics to explain the equilibrium distribution coefficient. The Aziz equation is only applicable to dilute alloys due to Henrian restrictions and is given by:

$$k = \frac{k_0 + \beta_0 V}{1 + \beta_0 V} \tag{2.43}$$

where V is the growth rate and β_0 is referred to as the solute trapping kinetic coefficient. β_0 is equal to a_0/D, where a_0 is a length scale of the order of interatomic distance and D is the mass diffusion coefficient in the liquid.

TLK claim that the marginal stability criterion applies to high growth rates if an appropriate value for k is calculated from Equation (2.43). Therefore, they replace the equilibrium partition coefficient, k_0, in the stability function, $F(A)$, and in A with the nonequilibrium partition coefficient, k, given by Aziz to obtain:

$$A_k = \frac{1}{1-(1-k)I_v(P_c)} \tag{2.44}$$

and

$$F_{TLK}(A_k) = \xi_t - 2\xi_c m_L \frac{C_0}{\Theta}\frac{\alpha}{D} A_k(1-k) = F_3(A_k) \tag{2.45}$$

Despite the inclusion of nonequilibrium interface kinetics through the Aziz equation, the effect of solute trapping does not reflect to the total bath supercooling in this model. The total supercooling still consists of only three parts, namely the thermal, solutal and curvature supercoolings, and is given by:

$$\Delta T_{TLK} = \Delta T_t + \Delta T_{c,TLK} + \Delta T_r \tag{2.46}$$

or

$$\Delta T_{TLK} = \frac{\Delta H_f}{c_p} I_v(P_t) - m_L C_0 \left[\frac{1}{1-(1-k)I_v(P_c)} - 1\right] + \frac{2\Gamma}{r} \tag{2.47}$$

Therefore, the interfacial kinetics that cause the deviation of k from k_0 is not accounted for in this model.

2.2.3 BCT Model, 1988

The heat and mass diffusion balances at the dendrite tip are not sufficient to uniquely determine the interface temperature, T^* in an alloy melt. The BCT model introduces the thermodynamic driving force at the interface, ΔG^*, to determine T^*. It employs the expression for ΔG^* shown by Baker and Cahn [17] for the advancement of the solid-liquid interface in a dilute binary alloy.

Baker and Cahn expresses the thermodynamic driving force across the interface as the change in free energy per mole of liquid of composition C_L^* that is transformed to solid of composition C_S^* at the interface temperature T^*. In their treatment of the solid and the liquid chemical potentials at the interface, they employ the general thermodynamic equilibrium rule for a closed heterogeneous system, which is also referred to as the tangent-to-tangent rule, given by:

$$\Delta G^* = (1 - C_S^*)(\mu_1^S - \mu_1^L) + C_S^*(\mu_2^S - \mu_2^L) \tag{2.48}$$

where μ_1^S and μ_1^L are the molar chemical potentials of the solvent in the solid and liquid phases, respectively, and μ_2^S and μ_2^L are the chemical potentials of the solute in the solid and liquid phases, respectively.

Assuming dilute solution conditions for both the solid and liquid phases and writing the chemical potentials for the solute using the Henry's law and those for the solvent using the

Raoults's law, Baker and Cahn write the interfacial driving force ΔG^* as:

$$\frac{\Delta G^*}{RT^*} = \ln\left(\frac{1-C_S^*}{1-C_L^*}\frac{1-C_L^{eq}}{1-C_S^{eq}}\right)(1-C_S^*) + \ln\left(\frac{C_S^*}{C_L^*}\frac{C_L^{eq}}{C_S^{eq}}\right)C_S^* \tag{2.49}$$

In the BCT model, ΔG^* is further simplified through the straight liquidus and solidus approximation and the dilute solution approximation, which gives:

$$\frac{\Delta G^*}{RT^*} = C_L^*\left[1-k\left(1-\ln\frac{k}{k_0}\right)\right] + (T_{m1}-T^*)\left(\frac{1-k_0}{m_L}\right) \tag{2.50}$$

Rearranging Equation (2.50) gives:

$$\frac{\Delta G^*}{RT^*} = -\frac{\Delta H_{f1}}{RT_{m1}^2}(T_{m1}+m_LC_L^*-T^*) + C_L^*\left[k_0-k\left(1-\ln\frac{k}{k_0}\right)\right] \tag{2.51}$$

In Equation (2.51), the term $-\frac{\Delta H_{f1}}{RT_{m1}^2}$ is obtained by replacing the $\frac{1-k_0}{m_L}$ term by using the Van't Hoff relation [31] that only applies to very dilute solutions, which introduces another limitation. ΔH_{f1} is the latent heat of fusion per mole of pure component (solvent) represented by 1, R is the universal gas constant and T_{m1} is the melting temperature of pure component.

The BCT model also adopts the collision-limited linear kinetic model discussed by Turnbull et al. [19] that relates the interfacial driving force, ΔG^*, to the velocity at the dendrite tip, V, via:

$$V = -V_0\frac{\Delta G^*}{RT^*} \tag{2.52}$$

where V_0 is a constant representing the maximum crystallization velocity of the alloy at infinite driving force. According to Turnbull's collision limited growth model, V_0 is set to be equal to the speed of sound and ΔG^* is defined to be negative during solidification.

It is important to note that Equation (2.51) states that the growth rate V is uniquely defined by ΔG^* and has nothing to do with the thermal and solutal gradients at the interface.

The collision-limited linear kinetic model may not be appropriate for high supercooling and high growth rate conditions. In such cases, the interfacial driving force, ΔG^*, would be large, whereas in the linear regime, interfacial driving forces should be small compared to RT^*. In Equation (2.52), the mobility of the interface, represented by V_0/RT^*, would be high due to the large value of V_0. Therefore, the interfacial driving force, ΔG^*, would need to be small to make the interface migrate at a finite velocity.

The combination of the thermodynamic driving force with the collision-limited linear kinetic law assumption, i.e., combination of Equations (2.51) and (2.52), gives the interface temperature as a function of the equilibrium and interface concentrations of the solid and the liquid, and the interface velocity shown as:

$$T^* = T_{m1} + m_L C_L^* + \frac{m_L C_L^*}{1-k_0}\left[k_0 - k\left(1 - \ln\frac{k}{k_0}\right)\right] - \frac{RT_{m1}^2}{\Delta H_{f1}}\frac{V}{V_0} \tag{2.53}$$

By reorganizing Equation (2.53), BCT introduced a kinetic slope m'_L defined by

$$m'_L = f(k) m_L \tag{2.54}$$

where

$$f(k) = 1 + \frac{k_0 - k\left(1 - \ln\frac{k}{k_0}\right)}{1-k_0} = \frac{1 - k\left(1 - \ln\frac{k}{k_0}\right)}{1-k_0} \tag{2.55}$$

The interface temperature is shown with the kinetic slope as:

$$T^* = T_{m1} + m'_L C_L^* - \frac{RT_{m1}^2}{\Delta H_{f1}}\frac{V}{V_0} \tag{2.56}$$

Equation (2.56) indicates that the interface composition of the liquid C_L^* is not defined by the kinetic liquidus at T^*, but instead, it is defined by the kinetic liquidus at a higher temperature equal to $T^* + \frac{RT_{m1}^2}{\Delta H_{f1}} \frac{V}{V_0}$. This is better shown by rearranging Equation (2.56) as

$$T^* + \frac{RT_{m1}^2}{\Delta H_{f1}} \frac{V}{V_0} = T_{m1} + m'_L C_L^* \tag{2.57}$$

Rewriting Equation (2.56) by including the curvature supercooling for a tip radius of r defined by

$$\Delta T_r = \frac{2\Gamma}{r} \tag{2.58}$$

gives the final form of T^* as:

$$T^* = T_{m1} + m'_L C_L^* - \frac{RT_{m1}^2}{\Delta H_{f1}} \frac{V}{V_0} - \frac{2\Gamma}{r} \tag{2.59}$$

Combining Equation (2.59) for T^* with the Ivantsov's solution for thermal supercooling and the equation for C_L^* as used in the LGK model gives the total supercooling, ΔT, which is given by the difference between the melting temperature of the alloy for a flat solidification front, where $(r = \infty)$, and the bath temperature as:

$$\Delta T = T_L(C_0, r = \infty) - T_\infty \tag{2.60}$$

where $T_L(C_0, r = \infty)$ is the liquidus temperature of a planar interface at C_0 and is equal to $T_{m1} + m_L C_0$. Recalling from Ivantsov's solution that $T^* - T_\infty$ is equal to the thermal supercooling and replacing T_∞ in Equation (2.60) with $T^* - \Delta T_t$ give:

$$\Delta T = T_{m1} + m_L C_0 - T^* + \Delta T_t \tag{2.61}$$

Substituting Equation (2.59) for T^* and Equation (2.17) for ΔT_t in Equation (2.61) gives the total supercooling shown by BCT as:

$$\Delta T_{BCT} = \frac{\Delta H_f}{c_p} I_v(P_t) - m_L C_0 \left[\frac{m'_L/m_L}{1-(1-k)I_v(P_c)} - 1 \right] + \frac{2\Gamma}{r} + \frac{RT^2_{m1}}{\Delta H_{f1}} \frac{V}{V_0} \tag{2.62}$$

Equation (2.62) can be rearranged and shown as:

$$\Delta T_{BCT} = \Delta T_t + m_L C_0 - m'_L C^*_L + \frac{2\Gamma}{r} + \frac{V}{\mu} \tag{2.63}$$

where μ is the linear kinetic coefficient given by $V_0 \frac{\Delta H_{f1}}{RT_{m1}{}^2}$.

As the interface kinetics are considered and T^* is presented as a function of the kinetic liquidus slope, the BCT model redefines the interface temperature to include a new term for kinetic supercooling, ΔT_k. As a consequence of introducing a new supercooling component, the total supercooling can be shown with four components given by:

$$\Delta T_{BCT} = \Delta T_t + \Delta T_c + \Delta T_r + \Delta T_k \tag{2.64}$$

However, BCT do not specify any part of the total supercooling equation shown in Equations (2.62) and (2.63) as ΔT_k, which has caused some confusion (see Section 2.31). The second term on the right hand side of Equation (2.62) has been mistakenly interpreted as the solutal supercooling leaving the last term as the kinetic supercooling in an attempt to define the the four supercooling terms shown in Equation (2.64).

The inclusion of the kinetic supercooling in the total supercooling satisfies the requirements for the correct use of the Aziz solute trapping model by moving the calculated interface solute concentration away from the local equilibrium value. However, the division between the solutal and kinetic supercooling terms is not clarified. This is due to defining a new effective nonequilibrium liquidus slope through the use of the linear kinetic law and the interfacial thermodynamic driving force. The general definition of the solutal supercooling for models that employ straight liquidus is $m_L(C_0 - C_L^*)$, which requires the use of the constant equilibrium slope, m_L. The second term on the right hand side of the BCT total supercooling in Equation (2.62), therefore, represents not only the solutal supercooling, but, also, part of the kinetic supercooling as discussed in Reference [5].

The BCT model can only be applied to dilute alloys since the expressions for the interfacial driving force and the nonequilibrium partition coefficient depend on Henrian conditions and the Baker-Cahn equation is valid only for dilute solutions. Another flaw of the BCT model is that it applies the Trivedi-Kurz marginal stability criterion, which does not account for the kinetic supercooling term, to conditions, where this term may become significantly large, without verifying its applicability. DA [5] pointed out that the Trivedi-Kurz marginal stability criterion must be used with the liquidus slope determined at C_L^* which may significantly differ from C_L^{eq}. Fortunately, this does not cause any inconsistencies of the BCT model as the liquidus slope in the Trivedi-Kurz marginal stability criterion is constant in the model [5].

2.3 Modifications to the Later Models

The BCT model has received much attention, but it has been interpreted incorrectly by some users [20, 21, 22] of this model resulting in a different treatment that resembles the TLK model more than the BCT model itself. For this reason, such treatments are referred to as "modified TLK models" [23] in this work.

In a typical modified TLK model, a kinetic supercooling component is added to the total supercooling equation and the liquidus slope is replaced with a nonequilibrium or kinetic slope that is shown by BCT. This kinetic slope is derived in the BCT model as part of the combination of the collision-limited growth theory with the interfacial driving force and is not intended to replace the liquidus slope. Thus, even though the modified TLK model defines the total supercooling using the four supercooling terms and applies the interface temperature equation used by BCT, which inherits the Baker-Cahn equation for determining the thermodynamic limits to solidification, it is not the same as the correct BCT model.

Through a correct understanding of the BCT model, DA [5] extends this model by proving the Trivedi-Kurz marginal stability criteria to apply in the presence of kinetic supercooling and correcting this criteria together with the Baker-Cahn equation to apply to curved phase boundaries.

2.3.1 A Modified TLK Model Adopting a Kinetic Liquidus

The BCT model has been appreciated for its correct treatment of the interface kinetics and the thermodynamic driving force along with the other transport and stability equations that form the basis of such free dendritic growth models. However, misinterpretation of the BCT model without considering the derivation of the equations caused the formation of a modified model, which is different from the BCT model as discussed in Reference [23]. This modified model [20, 21, 22], called as "TLK2" in this work, resembles a modified TLK model as it replaces the liquidus slope, m_L, with a nonequilibrium kinetic slope shown by BCT, m'_L, and adds a kinetic supercooling component,V/μ, to the total supercooling equation as if remedying the total supercooling equation of the TLK model for its deficiencies. For this reason, it is referred to as a modified TLK model [23].

The TLK model [3], which was published right after the LKT model [2] in the same year, does not address the kinetic supercooling, but the necessity of including a fourth supercooling component, $\Delta T_k = V/\mu$, for conditions where the interface kinetic effects become important, is suggested in the LKT model. Consequently, one might think that the term V/μ may be added to the formulation of the TLK model as well. Such a version of the TLK model is called as "TLK1" in this work. However, introducing the V/μ term directly in the total supercooling is not enough to make the model complete as it still neglects the effects of the thermodynamic driving force.

In TLK1, the TLK total supercooling equation modified with the additional supercooling term accounting for linear kinetics is shown as:

$$\Delta T_{TLK1} = \Delta T_{TLK} + \frac{V}{\mu} \tag{2.65}$$

By recalling the ΔT_{TLK} from Equation (2.47), the Equation (2.65) is rewritten as:

$$\Delta T_{TLK1} = \frac{\Delta H_f}{c_p} I_v(P_t) - m_L C_0 \left[\frac{1}{1-(1-k)I_v(P_c)} - 1 \right] + \frac{2\Gamma}{r} + \frac{V}{\mu} \tag{2.66}$$

where ΔT_{TLK1} is the total supercooling in the modified TLK model adopting a kinetic supercooling component. The interface temperature for this model given by:

$$T^*_{TLK1} = T_{m1} - \frac{2\Gamma}{r} + m_L C^*_L - \frac{V}{\mu} \tag{2.67}$$

Normalizing the ΔT_{TLK1} given by Equation (2.66) by dividing both sides by Θ as done in the previous models, where

$$\Theta = \frac{\Delta H_f}{c_p} \tag{2.68}$$

gives the dimensionless total supercooling $\overline{\Delta T}_{TLK1}$ as:

$$\overline{\Delta T}_{TLK1} = I_v(P_t) + \frac{m_L}{\Theta}(C_0 - C^*_L) + \frac{2\Gamma}{\Theta r} + \frac{V}{\Theta \mu} \tag{2.69}$$

In TLK2, the liquidus slope, m_L, in the TLK model is replaced with the nonequilibrium kinetic slope m'_L, and the attachment kinetics term, V/μ, is added to the total supercooling equation. The following paragraphs show how TLK2 is different from the BCT model by comparing the total supercooling derived from the modified model with that from the BCT model as discussed by Ando [23].

In general, the total supercooling is defined by:

$$\Delta T = T_L(C_0, r = \infty) - T_\infty \tag{2.70}$$

and, if the liquidus is linear,

$$\Delta T = (T_{m1} + m_L C_0) - T^* + \Delta T_t \tag{2.71}$$

where $T_L(C_0, r = \infty)$ is the liquidus temperature of a plane interface in a melt with composition C_0, T_∞ is the melt temperature far from the interface, T_{m1} is the melting temperature of the pure component (solvent), m_L is the equilibrium liquidus slope, C_0 is the alloy composition, T^* is the interface temperature and ΔT_t is the thermal supercooling.

The nonequilibrium kinetic slope m'_L and the liquidus slope m_L are both negative and $|m'_L| > |m_L|$. When the liquidus temperature of the flat interface, $T_L(C_0, r = \infty)$, is redefined for the kinetic slope, which is not the equilibrium liquidus slope, the total supercooling is reduced. Consequently, the total supercooling defined in the modified models [20, 21, 22], call it ΔT_{TLK2}, should be smaller than the ΔT defined in the LKT, TLK, and BCT models. ΔT_{TLK2} is obtained by substituting the T^* obtained by BCT,

$$T^* = T_{m1} - \frac{2\Gamma}{r} + m'_L C^*_L - \frac{V}{\mu} \tag{2.72}$$

into the total supercooling equation, which gives:

$$\Delta T_{TLK2} = \Delta T_t + m'_L (C_0 - C^*_L) + \frac{2\Gamma}{r} + \frac{V}{\mu} \tag{2.73}$$

In this equation, there still remain terms dependent on the liquidus slope inherited through some functions. The correct way of representing the total supercooling needs to be

$$\Delta T_{correct} = \Delta T_t + m_L C_0 - m'_L C^*_L + \frac{2\Gamma}{r} + \frac{V}{\mu} \tag{2.74}$$

as presented by BCT in Equation (2.63). It can easily be shown that the values of the supercoolings calculated by using Equations (2.73) and (2.74) will not be the same and that $\Delta T_{TLK2} < \Delta T_{correct}$ as $m'_L < m_L$. By remembering $m'_L = f(k) m_L$, Equation (2.73) can be rewritten as:

$$\Delta T_{TLK2} = \Delta T_t + f(k) m_L (C_0 - C^*_L) + \frac{2\Gamma}{r} + \frac{V}{\mu} \tag{2.75}$$

where

$$\Delta T_t = \frac{\Delta H_f}{c_p} I_v(P_t) \tag{2.76}$$

Normalizing the ΔT_{TLK2} equation by dividing both sides by Θ $(= \Delta H_f / c_p)$ gives:

$$\overline{\Delta T}_{TLK2} = I_v(P_t) + \frac{f(k)}{\Theta} m_L (C_0 - C^*_L) + \frac{2\Gamma}{\Theta r} + \frac{V}{\Theta \mu} \tag{2.77}$$

where $\overline{\Delta T}_{TLK2}$ is the dimensionless total supercooling. Pulling out C_0 in the second term on the right hand side of Equation (2.77) gives:

$$\overline{\Delta T}_{TLK2} = I_v(P_t) + \frac{f(k)}{\Theta} m_L C_0 \left(1 - \frac{C^*_L}{C_0}\right) + \frac{2\Gamma}{\Theta r} + \frac{V}{\Theta \mu} \tag{2.78}$$

In Equation (2.78), $C^*_L > C_0$, therefore, C^*_L / C_0 is bigger than 1 making the $(1 - C^*_L / C_0)$ term negative. It should also be noted that the value of m_L is negative, i.e., $m_L < 0$, making the second term in Equation (2.78), the solutal supercooling, positive. Rewriting C_0 in the normalized form as

$$\overline{C}_0 = -\frac{C_0|m_L|}{\Theta} \tag{2.79}$$

the normalized total supercooling equation becomes:

$$\overline{\Delta T}_{TLK2} = I_v(P_t) - \overline{C}_0 f(k)\left(1 - \frac{C_L^*}{C_0}\right) + \frac{2\Gamma}{\Theta r} + \frac{V}{\Theta\mu} \tag{2.80}$$

By remembering the equation for C_L^* obtained from Ivantsov's solution for mass diffusion at the dendrite tip, which is given by

$$C_L^* = \frac{C_0}{1-(1-k)I_v(P_c)} \tag{2.81}$$

Equation (2.80) can be rewritten as:

$$\overline{\Delta T}_{TLK2} = I_v(P_t) - \overline{C}_0 f(k)\left[1 - \frac{1}{1-(1-k)I_v(P_c)}\right] + \frac{2\Gamma}{\Theta r} + \frac{V}{\Theta\mu} \tag{2.82}$$

The bracketed part of the second term on the right hand side of Equation (2.82) was first shown in the LGK model as a function of the equilibrium partition coefficient, k_0, and was represented with a parameter A given by:

$$A = \frac{1}{1-(1-k_0)I_v(P_c)} \tag{2.83}$$

It was, then, redefined by TLK to replace the equilibrium partition coefficient k_0 by the nonequilibrium partition coefficient k. The new A, shown below as A_k, is given by:

$$A_k = \frac{1}{1-(1-k)I_v(P_c)} \tag{2.84}$$

Rewriting the normalized total supercooling equation with A_k gives:

$$\overline{\Delta T}_{TLK2} = I_v(P_t) - \overline{C}_0 f(k)(1 - A_k) + \frac{2\Gamma}{\Theta r} + \frac{V}{\Theta \mu} \tag{2.85}$$

Normalizing V and r by multiplying by $\frac{\Gamma}{2\alpha\Theta}$ and $\frac{\Theta}{\Gamma}$ respectively, gives:

$$\overline{V} = V\frac{\Gamma}{2\Theta\alpha} = \sigma^* P_t^2 F_3(A_k) \tag{2.86}$$

and

$$\overline{r} = r\frac{\Theta}{\Gamma} = \frac{1}{\sigma^* P_t F_3(A_k)} \tag{2.87}$$

The thermal Péclet number is then given as a function of the dimensionless variables $\overline{V}$ and $\overline{r}$ by:

$$P_t = \frac{VR}{2\alpha} = \overline{V}\overline{r} \tag{2.88}$$

In Equations (2.86) and (2.87), $F_3(A_k)$ is the stability function given by:

$$F_3(A_k) = \xi_t + 2\eta\overline{C}_0(1 - k)A_k\xi_c \tag{2.89}$$

where η is the ratio of thermal to solutal diffusivity given by α/D. By remembering that the dimensionless solute concentration, $\overline{C}_0$, is given by $\frac{|m_L|C_0}{\Theta}$ and substituting it in Equation (2.89), $F_3(A_k)$ is written as a function of the equilibrium slope m_L and is given by:

$$F_3(A_k) = \xi_t + 2\eta\frac{|m_L|C_0}{\Theta}(1 - k)A_k\xi_c \tag{2.90}$$

Since the equilibrium slope is replaced with the nonequilibrium slope given as $m'_L = f(k)m_L$, the stability function needs to be rewritten with m'_L to give:

$$F_4(A_k) = \xi_t + 2\eta f(k)\overline{C}_0(1 - k)A_k\xi_c \tag{2.91}$$

$f(k)m_L$, the stability function needs to be rewritten with m_L' to give:

$$F_4(A_k) = \xi_t + 2\eta f(k)\overline{C}_0(1-k)A_k\xi_c \tag{2.91}$$

By using $F_4(A_k)$ instead of $F_3(A_k)$, i.e., using the new stability function dependent on the nonequilibrium slope m_L' instead of the equilibrium slope m_L, the normalized total supercooling is given by:

$$\overline{\Delta T}_{TLK2} = I_v(P_t) - \overline{C}_0 f(k)(1-A_k) + 2\sigma^* P_t F_4(A_k) + \sigma^* P_t^2 F_4(A_k)\frac{2\alpha}{\mu\Gamma} \tag{2.92}$$

or

$$\overline{\Delta T}_{TLK2} = I_v(P_t) - \overline{C}_0 f(k)(1-A_k) + F_4(A_k)\left(2\sigma^* P_t + \sigma^* P_t^2\frac{2\alpha}{\mu\Gamma}\right) \tag{2.93}$$

Writing $F_4(A_k)$ explicitly in the normalized total supercooling equation gives:

$$\overline{\Delta T}_{TLK2} = I_v(P_t) - \overline{C}_0 f(k)(1-A_k) + \left[\xi_t + 2\eta f(k)\overline{C}_0(1-k)A_k\xi_c\right]\left(2\sigma^* P_t + \sigma^* P_t^2\frac{2\alpha}{\mu\Gamma}\right) \tag{2.94}$$

Rearranging and normalizing the total supercooling derived by BCT in Equation (2.62) by dividing both sides by Θ $(= \Delta H_f/c_p)$ gives:

$$\overline{\Delta T}_{BCT} = I_v(P_t) + \overline{C}_0[A_k f(k) - 1] + 2\sigma^* P_t F_3(A_k)\left(1 + P_t\frac{\alpha}{\mu\Gamma}\right) \tag{2.95}$$

The BCT total supercooling involves $F_3(A_k)$, which is dependent on the equilibrium slope m_L and the nonequilibrium partition coefficient, k, given by the Aziz equation. However, trying to adjust the equation to nonequilibrium conditions by replacing the m_L in $F_3(A_k)$

with m_L' is not a correct approach as done in the modified TLK model. Comparing the modified TLK model with the BCT model by subtracting the latter from the former gives:

$$\begin{aligned}\overline{\Delta T}_{TLK2} - \overline{\Delta T}_{BCT} = {} & -\overline{C}_0 f(k) \\ & + 2\eta\overline{C}_0(1-k)A_k\xi_c f(k)2\sigma^* P_t \\ & - 2\eta\overline{C}_0(1-k)A_k\xi_c 2\sigma^* P_t\left(1 + P_t\frac{\alpha}{\mu\Gamma}\right) \\ & + 2\eta\overline{C}_0(1-k)A_k\xi_c f(k)\sigma^* P_t^2\frac{2\alpha}{\mu\Gamma} + \overline{C}_0\end{aligned} \tag{2.96}$$

Rearranging Equation (2.96) gives:

$$\begin{aligned}\overline{\Delta T}_{TLK2} - \overline{\Delta T}_{BCT} = \overline{C}_0 \{ & -[f(k)-1)] + [f(k)-1]\,2\eta(1-k)A_k\xi_c 2\sigma^* P_t \\ & + [f(k)-1]\,2\eta(1-k)A_k\xi_c 2\sigma^* P_t^2\frac{\alpha}{\mu\Gamma}\Big\}\end{aligned} \tag{2.97}$$

or

$$\begin{aligned}\overline{\Delta T}_{TLK2} - \overline{\Delta T}_{BCT} = \overline{C}_0 \Big[& -1 + 2\eta(1-k)A_k\xi_c 2\sigma^* P_t \\ & + 2\eta(1-k)A_k\xi_c 2\sigma^* P_t^2\frac{\alpha}{\mu\Gamma}\Big]\,[f(k)-1]\end{aligned} \tag{2.98}$$

Finally, the difference between the total supercoolings defined by the modified TLK model and the BCT model is verified to be the same as that presented in Reference [23] and can be shown as:

$$\overline{\Delta T}_{TLK2} - \overline{\Delta T}_{BCT} = \overline{C}_0\left[-1 + 4\sigma^* P_t\eta(1-k)A_k\xi_c\left(1 + P_t\frac{\alpha}{\mu\Gamma}\right)\right][f(k)-1] \tag{2.99}$$

The difference shown in Equation (2.99) shows that the modified TLK total supercooling equation is different from the BCT equation by the terms on the right hand side of the equation. Consequently, the TLK, BCT and modified TLK models are all different from each other. The TLK model is not complete since it does not address the interfacial driving force unlike the BCT model. In addition, the approach of the modified TLK model to include the interface kinetics and the thermodynamic driving force by directly inserting the nonequilibrium kinetic slope is not correct.

2.3.2 An Extended BCT Model Employing Curved Phase Boundaries: DA Model

DiVenuti and Ando (DA) [5] recognized the necessity to use nonlinear phase boundaries to calculate the solidification parameters at the interface during free dendritic growth. Claiming the BCT model as the soundest of all, they extended this model to accommodate curved phase boundaries from the actual phase diagram. They emphasized the fact that for high supercooling cases, it would not be appropriate to use the straight solidus and liquidus particularly for systems with severely curved metastable extensions. The DA model rigorously modifies the marginal stability criterion given by Trivedi and Kurz shown in Equation (2.36) to account for the additional kinetic supercooling and the curved boundaries as:

$$-\Gamma\omega^2 - (\overline{K}_L G_L \xi_L + \overline{K}_S G_S \xi_S) + \left(\frac{\partial T_L}{\partial C}\right)_{C=C_L^*} G_C \xi_C = 0 \qquad (2.100)$$

The DA model, as in the BCT model, correctly incorporates the nonequilibrium conditions through use of the nonequilibrium partition coefficient given by Aziz [30] and the linear relationship between the tip velocity and the thermodynamic force given by Baker and Cahn [17]. Both models incorporate a kinetic supercooling term due to the involvement of interface kinetics.

The DA model reduces to the BCT model [4] if used with straight phase boundaries. One important distinction of the DA model is the manner it clearly defines the four parts of the total supercooling. The fact that BCT combine the kinetic terms that arise from the incorporation of a linear relation between the tip velocity and the interfacial thermodynamic force to obtain an effective nonequilibrium slope, m'_L, confused some of the users of the free dendritic growth models. Recalling the expression in the BCT model for the interface temperature given by:

$$T^* = T_{m1} + m'_L C^*_L - \frac{2\Gamma}{r} - \frac{V}{\mu} \tag{2.101}$$

and recalling the BCT total supercooling equation given by:

$$\Delta T_{BCT} = \frac{\Delta H_f}{c_p} I_v(P_t) - m_L C_0 \left[\frac{m'_L/m_L}{1-(1-k)I_v(P_c)} - 1 \right] + \frac{2\Gamma}{r} + \frac{V}{\mu} \tag{2.102}$$

many users of the BCT model perceive the second term on the right hand side of the latter equation, which can also be shown as $m_L C_0 - m'_L C^*_L$, as representing the solutal supercooling even though no such definitions are mentioned in the BCT model. The solutal supercooling for straight phase boundaries is, however, defined by $m_L(C_0 - C^*_L)$. With this misperception of the nonequilibrium liquidus slope, some users of the TLK model rewrote the solutal supercooling equation by replacing m_L by m'_L to get $m'_L(C_0 - C^*_L)$. The new total supercooling equation in the modified TLK model is given by:

$$\Delta T_{TLK2} = \Delta T_t + m'_L(C_0 - C^*_L) + \frac{2\Gamma}{r} + \frac{V}{\mu} \tag{2.103}$$

The DA model, on the other hand, uses the correct definition for the solutal supercooling,

$\Delta T_c = T_L(C_0) - T_L(C_L^*)$, which reduces to $\Delta T_c = m_L(C_0 - C_L^*)$ for a straight liquidus. It collects the terms that arise from the use of interfacial kinetics and thermodynamics in the kinetic supercooling term, which shows that the kinetic supercooling may become significantly important especially at high growth rates.

Chapter 3

Thermodynamic Calculations

This chapter presents the thermodynamic calculations required for the calculation of the curved phase boundaries between the liquid and the solid phases, which can be directly linked to the free dendritic growth models [5, 32, 33, 34, 35]. With the same thermodynamic calculations, the DA model [5] is further extended in this study by replacing the Baker-Cahn equation, which is limited to dilute solutions, with the driving force directly calculated from the free energy curves for the solid and liquid phases.

The chapter starts with background information for using thermodynamic calculations in rapid solidification problems and continues with information on the Ag-Cu system that is investigated followed by an introduction to the phase diagram calculation methods. First, an earlier study that is shown to be inconsistent in itself is addressed. Then, the application of a thermodynamic solution model to the Ag-Cu system to obtain a metastable phase diagram is explained together with results and discussion.

3.1 Background

Many of the current free dendritic growth models assume straight liquidus and solidus, which often works well for low supercoolings, but, the latter assumption may not apply to systems with phase boundaries that are considerably curved [5, 36]. In such systems, the stable phase diagram alone may not give all the information needed in the computation of dendritic growth in a highly supercooled melt. Under such rapid solidification conditions, the use of metastable extensions of phase boundaries, which are often curved, becomes unavoidable. Moreover, such metastable extensions must be used in a dendritic growth model in a thermodynamically consistent manner. Amongst the free dendritic growth models discussed in this study, the DA model successfully incorporates the curved boundaries in formulating the driving force for solidification and derives the equations in accordance with the procedure of the BCT model [4].

In addition to calculating the curved phase boundaries, the thermodynamic solution model can be used to more rigorously address the kinetics of phase transformations especially when the rate of transformations is so high that not enough time is allowed for the system to reach an equilibrium state. In such cases, experimental data that are available from equilibrium measurements do not sufficiently describe the non-equilibrium conditions encountered. Free dendritic growth observed during rapid solidification of metal alloys is one of such cases, where the solidification front attains a higher velocity and different solute compositions from those given by the equilibrium conditions.

The kinetics of solidification determine how fast structural changes may occur during materials processing and it is the free energy change at the solid-liquid interface that drives the growth of the solid.

One of the objectives of this study is to address the direct computation of the interfacial driving force for free dendritic growth, ΔG^*. The DA model is modified to include a ΔG^* calculated with a thermodynamic solution model so that the Henrian restriction of the Baker-Cahn equation [17] is eliminated. The Ag-Cu system was selected for this investigation considering the availability of thermochemical [37] and solidification data [38, 39] as well as the relative simplicity of the phase diagram. The phase diagram calculation for the Ag-Cu system published by Murray [36] is found to be inconsistent in itself. Therefore, a new phase diagram with metastable extensions of the equilibrium phase boundaries is computed using a correct thermodynamic solution model.

The following text provides information on the Ag-Cu system and its properties developed in this study.

3.2 The Ag-Cu System

The Ag-Cu system forms a simple eutectic phase diagram. The equilibrium phases are the liquid phase, and the Ag-rich and Cu-rich solid solutions with some degrees of miscibility, particularly near the eutectic temperature. The Ag-rich fcc solid solution has a maximum solid solubility of 14.1 at.% Cu and the Cu-rich fcc solid solution has a maximum solid solubility of 4.9 at.% Ag. The radius, valence and electronegativity values of the Ag and Cu atoms can be seen in Table 3.1 [39].

Table 3.1: Properties of Ag and Cu atoms

Component	*Crystal Structure*	*Radius*	*Valence*	*Electronegativity*
Ag	fcc	0.144 nm	+1, +2, +3	1.80
Cu	fcc	0.128 nm	+1, +2, +3	1.90

The finite miscibility in the solid solutions can be understood by applying the Hume-Rothery criteria for solid solubility of the Ag-Cu solutions. Silver and copper both belong to the IB group in the periodic table, and have the same crystal structure as well as similar electronegativities as shown in Table 3.1. The difference in atomic radii also is small enough (about 13 %) to permit appreciable solubilities in the fcc solutions.

Experimental studies on the Ag-Cu system to determine the equilibrium liquidus, solidus and solvus data together with studies to determine the metastable phases are reviewed and summarized by Subramanian et al. [39]. Silver and copper are shown to have slightly different lattice parameters of, respectively, 4.09 $\overset{\circ}{A}$ and 3.61 $\overset{\circ}{A}$ at 298 K.

Rapid solidification of this alloy produces solid solutions having a lattice parameter between 3.61 $\overset{\circ}{A}$ and 4.09 $\overset{\circ}{A}$ [40, 39]. The most commonly seen phase is the fcc solution of silver and copper. Most of the other solid solutions that have been observed in the Ag-Cu alloys are thought to be decomposition products of this metastable fcc solution [39]. Experimental data for the lattice parameters versus the composition for the metastable Ag-Cu solid solution indicate a positive deviation (about 1 %) from Vegard's law. This implies that the enthalpy of mixing for this system is positive, i.e., endothermic.

Due to the fact that both silver and copper freeze into the fcc structure, and that mixing is endothermic, a single Gibbs free energy curve with a W-shape connecting the Ag-rich and Cu-rich sides is expected for the solid phase.

3.3 Phase Diagram Calculation Methods

The computation of phase diagrams and free energy curves requires a thermodynamic model appropriate to the system in concern. The accurateness of thermodynamic estimations and predictions depends principally on the correctness, reliability and consistency of the equations that constitute the thermodynamic model employed.

Modeling phase diagrams by physicists has mainly concentrated on using the Helmholtz free energy and finding a good configurational entropy (Quasichemical, CVM-Cluster Variation Model) to describe main features, whereas modeling amongst material scientists have mainly concentrated on finding a good excess Gibbs free energy to reproduce the experimental data. In this study, the latter method is followed.

It is very important in phase diagram calculations that regardless of the model employed, its equations must correctly address the thermodynamic equilibrium. The criterion for equilibrium in a heterogeneous system is that the chemical potential of a component is the same for all the phases in the system given by:

$$\mu_i^I(x_i^I, T, P) = \mu_i^{II}(x_i^{II}, T, P) = ... = \mu_i^\phi \tag{3.1}$$

where x is the mole fraction of the chemical species i, ϕ is the phase, and T and P are the system temperature and pressure. This requirement is a necessary condition for any heterogeneous system at rest. The necessary and sufficient condition for stability for a system in an isothermal and isobaric environment is given by:

$$(dG)_{T,P} \geq 0 \tag{3.2}$$

It can be shown that Equation (3.1) is equivalent to $(dG)_{T,P} = 0$, which is only a part of Equation (3.2).

Solution models, proposed to form physically correct or mathematically apposite analytical expressions for the free energies of the phases present in a system, contain unknown constant parameters, which need to be determined by fitting the equations to the available experimental and/or thermochemical data. A description of thermodynamic models for ideal and real solutions is presented in Section A.2 in Appendix A and the thermodynamic functions for various models are summarized in Table 3.2.

To calculate the metastable phase diagram of the Ag-Cu system, a temperature dependent subregular solution model [44, 43] is employed to define the Gibbs free energy for both the liquid and solid phases in which the free energy is given by (see Appendix A):

$$\begin{aligned} G^{\phi} = G_1^{0,\phi} x_1 + G_2^{0,\phi} x_2 + RT(x_1 \ln x_1 + x_2 \ln x_2) \\ + (A^{\phi} + B^{\phi} x_1) x_1 x_2 \left(1 - \frac{T}{\tau^{\phi}}\right) \end{aligned} \tag{3.3}$$

where 1 and 2 represent the first and the second component, respectively, ϕ represents the phase, and A, B, and τ are the subregular solution model parameters.

Table 3.2: Comparison of the Thermodynamic Functions of Solution Models

Thermodynamic function	Solution model			
	Ideal	Regular [41]	Subregular [42]	Subregular(T) [43]
ΔH^{id}	0	0	0	0
H^{xs}	0	$\surd$	$\surd$	$\surd$
ΔS^{id}	$\surd$	$\surd$	$\surd$	$\surd$
S^{xs}	0	0	0	$\surd$
$\Delta G^{id} = \Delta H^{id} - T\Delta S^{id}$	ΔS^{id}	ΔS^{id}	ΔS^{id}	ΔS^{id}
$G^{xs} = H^{xs} - TS^{xs}$	0	H^{xs}	H^{xs}	$H^{xs} - TS^{xs}$
$\Delta H^{m} = \Delta H^{id} + H^{xs}$	0	H^{xs}	H^{xs}	H^{xs}
$\Delta S^{m} = \Delta S^{id} + S^{xs}$	ΔS^{id}	ΔS^{id}	ΔS^{id}	$\Delta S^{id} + S^{xs}$
$\Delta G^{m} = \Delta H^{m} - T\Delta S^{m}$	$-T\Delta S^{id}$	$H^{xs} - T\Delta S^{id}$	$H^{xs} - T\Delta S^{id}$	$H^{xs} - T(\Delta S^{id} + S^{xs})$

3.4 Application of a Thermodynamic Solution Model to the Ag-Cu System

A metastable phase diagram for the Ag-Cu system has been recently computed by Murray [36] using a temperature dependent thermodynamic solution model. Even though this model can produce the phase diagram with good proximity, it is shown in this study that the model is not self-consistent and does not satisfy the necessary condition for equilibrium required in a heterogeneous system.

3.4.1 Metastable Phase Diagram Calculated by Murray

Murray calculated the Ag-Cu metastable phase diagram by using a solution model that is linearly dependent on temperature, which is referred to as the subregular solution model, to describe the excess Gibbs free energy for both the solid and liquid phases. The results obtained match the experimental data well except for some variation of the eutectic compositions from the widely accepted values. The expression used by Murray to define the excess free energy does not satisfy the necessary condition for equilibrium given by Equation (B.3) as:

$$G^{xs} = x_1\mu_1^{xs} + x_2\mu_2^{xs} \tag{3.4}$$

which is the most important requirement for the calculation of phase diagrams. In that sense, it cannot be referred to as a consistent subregular solution model, proved to satisfy the necessary condition, as shown in Equations (B.6) to (B.7) in Appendix B.

In Murray's treatment, the liquid phase is taken as the reference state for both components. The constant parameters of the subregular solution model that Murray defines as the free energy interaction coefficients are determined by fitting the equations to the equilibrium phase boundaries and the thermochemical data. Calculations are done by optimizing the "least squares" solution of the parameters to fit these parameters to the data. The optimization program requires initial guess values of the Gibbs free energies and allows different combinations of parameters to be simultaneously varied. The free energy equation used by Murray for each phase is given as:

$$\begin{aligned} F_i = {} & F_{Ai}^0 x_A + F_{Bi}^0 x_B + RT(x_A \ln x_A + x_B \ln x_B) \\ & + (f_i + \sigma_i T)x_A x_B + (f_i' + \sigma_i' T)x_A x_B(x_A - x_B) \end{aligned} \tag{3.5}$$

where A and B represent the first and second component, respectively, and i represents the phase. Murray refers to F^0 as the lattice stability parameter of the pure material and refers to f_i, σ_i (J/mol) and f_i', σ_i' (J/mol K) as the Gibbs free energy interaction coefficients [1] for

---

[1] General information about using interaction coefficients in the formulation of the excess free energy is provided in Section A.1 of Appendix A. It is explained by Lupis [44] that the temperature dependent subregular solution model can be expressed in terms of the free energy interaction parameters.

each phase. Thus, the excess free energy that Murray uses is given by:

$$F^{xs} = (f + \sigma T)x_A x_B + (f' + \sigma' T)x_A x_B(x_A - x_B) \tag{3.6}$$

Rewriting Equation (3.6) by replacing the subscripts A and B used to define the components by 1 and 2, respectively, to match the nomenclature of this text gives:

$$F^{xs} = (f + \sigma T)x_1 x_2 + (f' + \sigma' T)x_1 x_2(x_1 - x_2) \tag{3.7}$$

Using Equations (B.1) and (B.2), which should apply to any phase, the partial molar free energies in Murray's formulation becomes:

$$\overline{F}_1^{xs} = \mu_1^{xs} = (f + \sigma T)x_2 + (f' + \sigma' T)[x_2(x_1 + x_1 x_2 - x_2)] \tag{3.8}$$

$$\overline{F}_2^{xs} = \mu_2^{xs} = (f + \sigma T)x_1 + (f' + \sigma' T)[x_1(x_1 - x_1 x_2 - x_2)] \tag{3.9}$$

The equilibrium condition for the Gibbs free energy can be written in terms of F as Murray represents the Gibbs free energy by F. Then, F^{xs} can be written as:

$$F^{xs} = x_1\overline{F}_1^{xs} + x_2\overline{F}_2^{xs} \tag{3.10}$$

Substituting the molar free energy equations for each component given in Equations (3.8) and (3.9) in the equilibrium condition will give:

$$\begin{aligned} F^{xs} &= x_1\left\{(f + \sigma T)x_2 + (f' + \sigma' T)[x_2(x_1 + x_1 x_2 - x_2)]\right\} \\ &\quad + x_2\left\{(f + \sigma T)x_1 + (f' + \sigma' T)[x_1(x_1 - x_1 x_2 - x_2)]\right\} \\ &= 2x_1 x_2(f + \sigma T) + x_1 x_2(f' + \sigma' T)(x_1 + x_1 x_2 - x_2 + x_1 - x_1 x_2 - x_2) \\ &= 2x_1 x_2(f + \sigma T) + 2x_1 x_2(f' + \sigma' T)(x_1 - x_2) \end{aligned} \tag{3.11}$$

which is twice the original equation used by Murray. As Equation (3.11) and Equation (3.7) are not the same, the necessary equilibrium condition is not satisfied.

It is possible to rearrange Murray's definition for excess free energy into the temperature dependent subregular solution model structure given by Equation (3.3). Remembering the excess free energy expression for the temperature dependent subregular solution given by Equation (B.3) as $G^{xs} = (A+Bx_2)x_1x_2(1-T/\tau)$ and reorganizing Murray's formulation give:

$$F^{xs} = x_1x_2\left[(f+\sigma T)+(f'+\sigma' T)-2(f'+\sigma' T)x_2\right] \tag{3.12}$$

Letting $\sigma = -\frac{f}{\tau}$ and $\sigma' = -\frac{f'}{\tau}$ will give:

$$F^{xs} = x_1x_2\left[f\left(1-\frac{T}{\tau}\right)+f'\left(1-\frac{T}{\tau}\right)-2f'\left(1-\frac{T}{\tau}\right)x_2\right] \tag{3.13}$$

and rearranging Equation (3.13) will give:

$$F^{xs} = (\underbrace{f+f'}_{A} - \underbrace{2f'}_{B}x_2)x_1x_2\left(1-\frac{T}{\tau}\right) \tag{3.14}$$

where combining the interaction coefficients will give the subregular solution model parameters as:

$$f+f' = A \quad \text{and} \quad -2f' = B \tag{3.15}$$

In order for the above equations to hold and Murray's equation to satisfy the equilibrium condition in the form of the temperature dependent subregular solution model, the values of the interaction coefficients obtained by Murray should give a single value for τ in each phase. This is due to the presence of a single free energy curve in both the solid phase and the liquid phase. Consequently, the conditions that should hold for Equation (3.12) to resemble the temperature dependent subregular solution can be given as:

$$\tau_\alpha = -\frac{f_\alpha}{\sigma_\alpha} \overset{?}{=} \tau_\alpha = -\frac{f'_\alpha}{\sigma'_\alpha} \tag{3.16}$$

$$\tau_L = -\frac{f_L}{\sigma_L} \overset{?}{=} \tau_L = -\frac{f'_L}{\sigma'_L} \tag{3.17}$$

The conditions in Equations (3.16) and (3.17) can be checked by applying the values calculated by Murray on these equations. The results of Murray's calculations are presented in Table 3.3 as they appear in the original article [36].

Table 3.3: Interaction Parameters Calculated by Murray

Liquid Phase		Solid Phase	
$F^0_{Ag} =$	0	$F^0_{Ag} =$	$-11945 + 9.67\,T$
$F^0_{Cu} =$	0	$F^0_{Cu} =$	$-13054 + 9.62\,T$
$f_L =$	$15171 - 2.537\,T$	$f_{fcc} =$	$34532 - 9.178\,T$
$f'_L =$	$-2425 + 0.946\,T$	$f'_{fcc} =$	$-5996 + 1.725\,T$

It must be noted, as also indicated in Reference [39], that in the expressions for f and f' only the first terms represent f and f', and the second terms before the temperature T represent σ and σ'. Applying the interaction coefficients shown in Table 3.3 to Equations (3.16) and (3.17) will give:

$$\tau_\alpha = -\frac{34532}{-9.178} = 3762.475 \neq \tau_\alpha = -\frac{-5996}{1.725} = 3475.942 \tag{3.18}$$

$$\tau_L = -\frac{15171}{-2.537} = 5979.897 \neq \tau_L = -\frac{-2425}{0.946} = 2563.425 \tag{3.19}$$

It can be seen in the above calculation that the terms that need to be equal are not equal, and τ_α and τ_L each have been assigned two different values, which is not possible for a system with a single free energy curve in each of the solid and liquid phases.

Consequently, Murray's model should not be used to calculate the phase diagram as it does not satisfy the necessary equilibrium condition, although Murray's model replicates the equilibrium phase boundaries of the Ag-Cu system very well and predicts the metastable extensions of all phase boundaries similar to those calculated with the model presented in this work.

3.4.2 Computation of the Ag-Cu Metastable Phase Diagram

The Ag-Cu metastable phase diagram is computed using the temperature dependent subregular solution model to define the excess free energy, which satisfies the necessary criterion for equilibrium as well as the necessary and sufficient conditions for stability given in Equations (3.1) and (3.2). Two main phases are assumed to exist in the Ag-Cu system: The fcc solid phase, represented by α, and the liquid phase, L. Therefore, there are two Gibbs free energy curves represented by G^α and G^L.

Calculation of Thermodynamic Parameters

In the temperature dependent subregular solution model, the excess Gibbs free energy, G^{xs}, is assumed to be composed of an excess enthalpy, H^{xs}, and an excess entropy term, S^{xs}, as shown in Table 3.2. The derivation of G^{xs} is described in Appendix A and given by using the temperature dependent subregular solution model as:

$$G^{xs,\phi} = \left(A^{\phi} + B^{\phi} x_2\right) x_1 x_2 \left(1 - \frac{T}{\tau^{\phi}}\right) \tag{3.20}$$

where A, B and τ are the solution model parameters of a phase represented by ϕ and x is the concentration (in mole fractions) of components represented by 1 and 2.

Using the excess free energy given by Equation (3.20), the phase boundary equations for the solid and the liquid can be obtained as described in Section B.2 in Appendix B. The phase boundary equations written in terms of the mole fractions of the second component, x_2, are given by:

$$\begin{aligned} \ln \frac{1 - x_2^{\alpha}}{1 - x_2^{L}} + \frac{1}{RT} \Bigg\{ & \left[A^{\alpha} + B^{\alpha}(2x_2^{\alpha} - 1)\right] \left(1 - \frac{T}{\tau^{\alpha}}\right) x_2^{\alpha 2} \\ & - \left[A^{L} + B^{L}(2x_2^{L} - 1)\right] \left(1 - \frac{T}{\tau^{L}}\right) {x_2^{L}}^2 \Bigg\} - \frac{\Delta\mu_1^{0,\alpha\rightarrow L}}{RT} = 0 \end{aligned} \tag{3.21}$$

$$\begin{aligned} \ln \frac{x_2^{\alpha}}{x_2^{L}} + \frac{1}{RT} \Bigg\{ & \left(A^{\alpha} + 2B^{\alpha} x_2^{\alpha}\right) \left(1 - \frac{T}{\tau^{\alpha}}\right) \left(1 - x_2^{\alpha}\right)^2 \\ & - \left(A^{L} + 2B^{L} x_2^{L}\right) \left(1 - \frac{T}{\tau^{L}}\right) \left(1 - x_2^{L}\right)^2 \Bigg\} - \frac{\Delta\mu_2^{0,\alpha\rightarrow L}}{RT} = 0 \end{aligned} \tag{3.22}$$

Since the system is eutectic, there are six phase boundaries to be calculated: Two sets of solidus and liquidus, one set on the Ag-rich side and the other on the Cu-rich side, and two solvi, one on each side of the phase diagram. Equations (3.21) and (3.22) are solved for the unknown coefficients A^{ϕ}, B^{ϕ} and τ^{ϕ} of each phase using the available experimental data. Once the coefficients are determined, the same equations are solved for the molar fractions, x_i^{ϕ}, of the same equations along a temperature range to give the phase diagram.

In this study, Component 1 represents the solvent Ag and Component 2 represents the solute Cu. All the calculations are based on the mole fraction of component 2. The two equilibrium phase boundary equations given in Equations (3.21) and (3.22) are written three times: First for the boundaries between the solid and the liquid ($\alpha \rightarrow L$) on the Ag-rich side, then for the boundaries between the liquid and the solid ($L \rightarrow \alpha$) on the Cu-rich side, and for the boundaries between the Ag-rich solid and the Cu-rich solid ($\alpha \rightarrow \alpha$), which are of the same fcc structure. All six equations are solved simultaneously at the eutectic temperature.

The subregular solution model, when applied to the whole system of equations with three sections, has six unknown constants to be solved for: $A^\alpha, B^\alpha, \tau^\alpha, A^L, B^L, \tau^L$. The variables are the temperature and composition of each phase on each section of the phase diagram, symbolically shown as T, x_2^ϕ. The values of these variables are obtained from published experimental data for the equilibrium phase diagram [38, 39]. It is important to note that there are different values for x_2^α and x_2^L on each of the three sections of the phase diagram. Consequently, there are six mole fraction variables and together with the input constant parameter temperature, the total number of variables in this system of equations is seven. The variables and constant parameters of the phase diagram equations can be represented as:

$$f(T, x_2^{\alpha 1}, x_2^{L1}, x_2^{\alpha 2}, x_2^{L2}, x_2^{S1}, x_2^{S2}, A^\alpha, B^\alpha, \tau^\alpha, A^L, B^L, \tau^L) = 0, \tag{3.23}$$

where the superscripts $L1, \alpha 1, L2, \alpha 2, S1, S2$ represent the liquidus and the solidus on the Ag(1)-rich side, the liquidus and the solidus on the Cu(2)-rich side and the solvus on the

Ag-rich and Cu-rich sides, respectively.

Numerical Solution of the Phase Boundary Equations

Given the compositions at the eutectic temperature, the set of six nonlinear equations are first solved simultaneously for the subregular solution model parameters using a Mathcad function employing the Conjugate Gradient method. The resultant parameters are substituted back in the phase diagram equations to solve for the molar fractions. An iterative program written in Matlab [45, 46] is used to solve these equations for the six roots (compositions in molar fractions) given the temperature and repeated over a range. The calculated compositions in mole fractions of Cu are shown in Figure 3.1 starting from 273 K.

3.5 Results and Discussion

As a result of the calculations, a variety of solutions for the subregular solution model parameters $A^\alpha, B^\alpha, \tau^\alpha, A^L, B^L, \tau^L$ giving phase diagrams, which match the experimental data almost perfectly, is obtained.

The calculated phase diagram in Figure 3.1 agrees well with the calculated phase boundaries with the experimental data of Heycock [38, 39] shows the suitability of the subregular solution model with this system. The solidi are shown to be retrograde below the eutectic temperature, which indicates that the straight phase boundary assumption in free dendritic growth models would not be valid for high supercoolings.

The solvi are found to form a miscibility gap above the eutectic temperature. The critical point on the solid phase miscibility gap is calculated to occur at a Cu mole fraction of 0.61 and 1366.45 K, which is a lower value than that calculated by Murray at 1382 K [36].

The total Gibbs free energy curves for the solid and liquid phases are studied at different temperatures taking the solid as the reference phase for both components. Figures 3.2 to 3.5 show the calculated free energy curves using the temperature dependent subregular solution model. It is observed that the free energy curve for the solid has a W-shape below the melting temperature of the higher melting Cu due to the fact that mixing is endothermic.

The free energy calculations using the subregular solution model for the Ag-Cu system, thus proved to be sound, are used in the calculation of the interfacial driving force presented in Chapter 5.

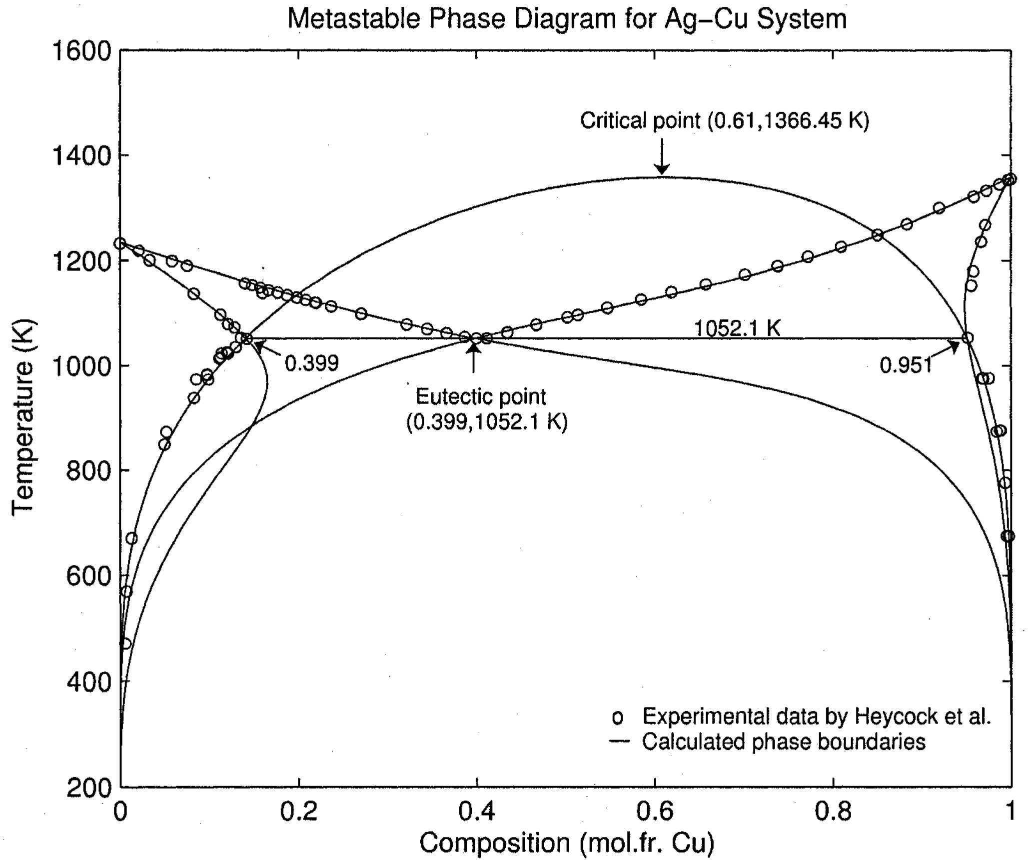

Figure 3.1: Calculated metastable phase diagram of Ag-Cu alloy system using a temperature dependent subregular solution model.

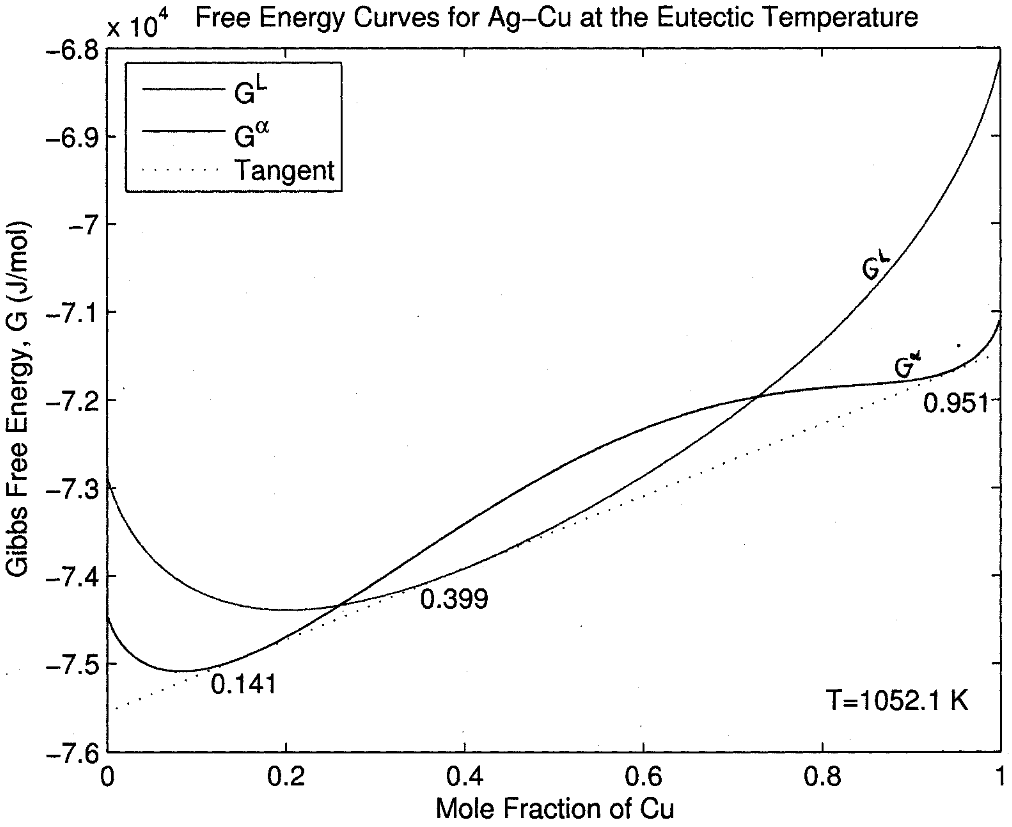

Figure 3.2: Calculated Gibbs free energies for the Ag-Cu system at the eutectic temperature 1052.1 K

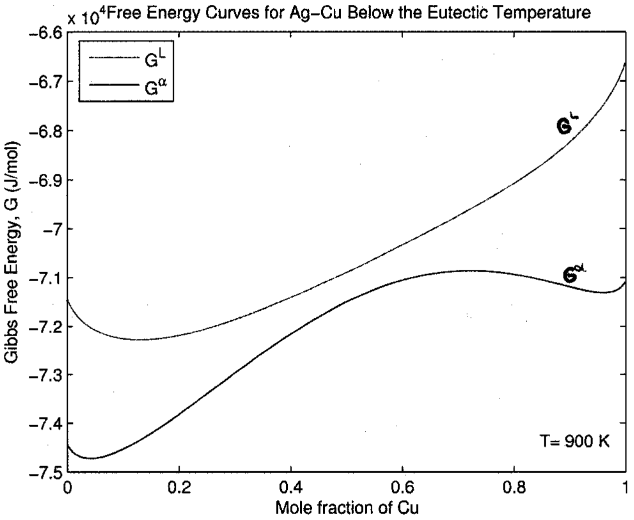

Figure 3.3: Calculated Gibbs free energies for the Ag-Cu system below the eutectic temperature at 900 K

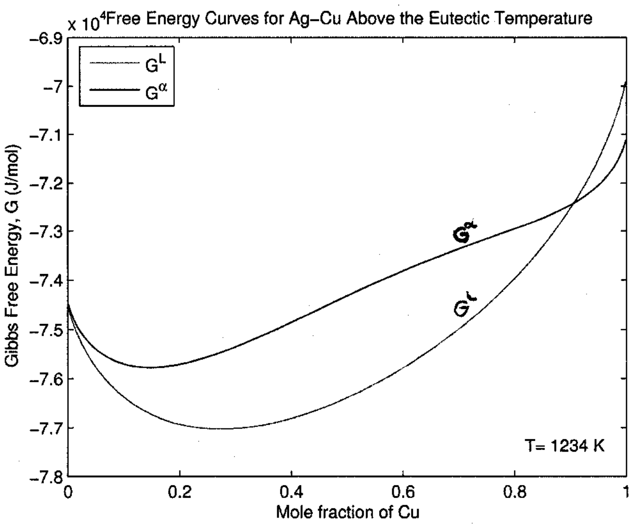

Figure 3.4: Calculated Gibbs free energies for the Ag-Cu system above the eutectic temperature at the melting temperature of Ag at 1234 K

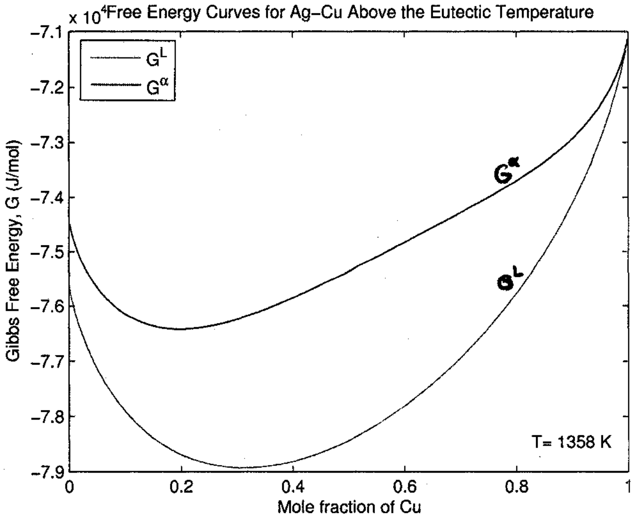

Figure 3.5: Calculated Gibbs free energies for the Ag-Cu system above the eutectic temperature at the melting temperature of Cu at 1358 K

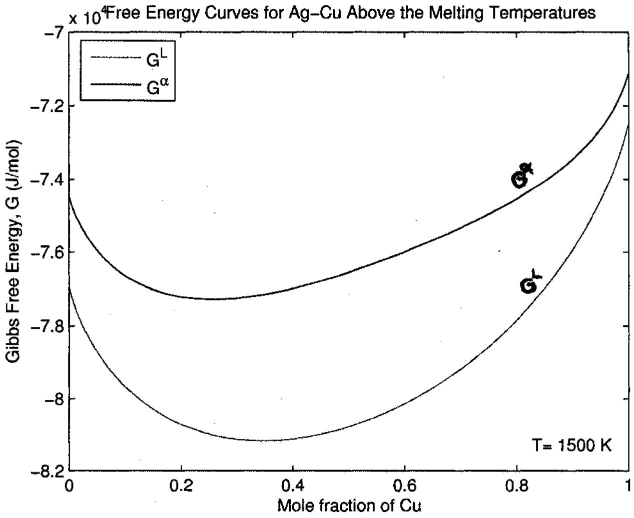

Figure 3.6: Calculated Gibbs free energies for the Ag-Cu system above the melting temperatures of Ag and Cu at 1500 K

Chapter 4

Comparative Computation with the Free Dendritic Growth Models

One of the objectives of this doctoral study is to apply the free dendritic growth models that are derived from the earlier LGK model [9] to a specific alloy to provide numerical comparisons of the models and their modifications. The specific free dendritic growth models assume an isothermal, isosolutal paraboloidal dendrite tip that migrates into a supercooled melt with a constant growth rate. The free dendritic growth models compared in this study are the LKT, TLK, and BCT models, the modified TLK model adopting a kinetic liquidus, and the DA model, which is an extended BCT model employing curved phase boundaries.

The free dendritic growth models, studied in this work in a chronological order, added new equations to the earlier LGK model in an attempt to make it applicable to high crystal growth rates. However, the addition of new equations introduced new restrictions that were inherited with the equations or caused inconsistencies in the models. An overview of the free dendritic growth models and their limitations is presented in Chapter 1. A critical review and description of the free dendritic growth models, based on the discussions provided by Ando [23], is presented in Chapter 2. For the application of the free dendritic growth models, a Ag-15 mass % Cu alloy is selected due to the availability of solidification and thermochemical data. Thermodynamic calculations related to this system, as required in the DA model, are presented in Chapter 3.

Applying these free dendritic growth models, all originating from the LGK model, to the same alloy allows to compare the models numerically and to illustrate how the models differ from each other. This chapter starts with the scheme and method employed for the numerical comparison of the free dendritic growth models and presents the computation results graphically with discussion showing the variation of the solidification parameters with increasing total supercooling.

4.1 Computation Scheme

Free dendritic growth models typically predict the dendrite tip radius, r, and the interface velocity, V, given an alloy composition, C_0, and a total melt supercooling, ΔT. The other important parameters that depend on these two variables, V and r, are the interface temperature, T^*, the liquid concentration at the interface, C_L^*, and the solute partition coefficient, k. The free dendritic growth models studied in this work treat these variables in different ways.

At the beginning of the computation, the two independent variables, V and r, are introduced as initial guess values to solve for the dependent variables and, at the end, they are obtained as the solutions to the system of two equations given by:

$$f_1 = V_{guess} - V_{calculated} \tag{4.1}$$

$$f_2 = r_{guess} - r_{calculated} \tag{4.2}$$

Given the alloy composition C_0, the liquidus temperature of the melt for a flat interface shown by $T_L(C_0, r = \infty)$ can easily be obtained from the phase diagram. The melt (bath) temperature is, then, given by:

$$T_\infty = T_L(C_0, r = \infty) - \Delta T \tag{4.3}$$

Next, the interface temperature T^* needs to be found using Equation (2.15). This requires the knowledge of the thermal Péclet number P_t and the dimensionless thermal supercooling Ω_t, which is equal to $I_v(P_t)$. By using the input guess values of V and r, the thermal Péclet number P_t is obtained from:

$$P_t = \frac{Vr}{2\alpha} \tag{4.4}$$

The dimensionless thermal supercooling is calculated using the Ivantsov function defined as

$$I_v(P_t) = -P_t e^{P_t} E_i(P_t) \tag{4.5}$$

where the exponential integral function $E_i(P_t)$ is calculated from the approximations given in Equations (C.2) and (C.3) in the appendix. The dimensionless thermal supercooling is multiplied by the unit supercooling Θ, which is constant and can be calculated from thermochemical data ($\Theta = \Delta H_f / c_p$), to get the thermal supercooling ΔT_t given as:

$$\Delta T_t = \frac{\Delta H_f}{c_p} I_v(P_t) \tag{4.6}$$

Adding the thermal supercooling to the bath temperature gives the interface temperature T^* shown as:

$$T^* = T_\infty + \Delta T_t \tag{4.7}$$

From the interface temperature, the equilibrium concentrations of the solid and the liquid at this temperature, C_S^{eq} and C_L^{eq}, can be found using phase diagram data. Whether assuming straight phase boundaries as in the LKT, TLK, and BCT models, or employing curved phase boundaries from a metastable phase diagram as in the DA model, the phase boundaries need to be adjusted for the curved solid-liquid interface by shifting them down by the amount given by the curvature supercooling given by:

$$\Delta T_r = \frac{2\Gamma}{r} \tag{4.8}$$

The models that assume straight phase boundaries determine the constant parameters k_0 and m_L from phase diagram data and get the equilibrium concentration of the liquid and the solid from

$$C_L^{eq} = -\frac{T_{m1} - \Delta T_r - T^*}{m_L} \tag{4.9}$$

and

$$C_S^{eq} = C_L^{eq} m_L \tag{4.10}$$

The DA model, on the other hand, employs a binary phase diagram that includes the curved metastable extensions of the liquidus and the solidus below the eutectic temperature. The corresponding equilibrium concentrations C_L^{eq} and C_S^{eq} at T^* are obtained from this metastable phase diagram after shifting both the liquidus and the solidus by ΔT_r. Then, the equilibrium partition coefficient is obtained from:

$$k_0 = \frac{C_S^{eq}}{C_L^{eq}} \tag{4.11}$$

A nonequilibrium partition coefficient, k, is employed in the TLK, BCT, modified TLK, and DA models. The LKT model does not use k as it does not introduce any interface kinetics. k is defined by Aziz [30] in Equation (2.43) as a function of the interface velocity, the equilibrium partition coefficient, and the solute trapping kinetic coefficient. The solute trapping kinetic coefficient β_0, is a function of the mass diffusion coefficient D, which is used as a constant in the LKT, TLK, and BCT models, but is replaced in the DA model with the Arrhenius law given by:

$$D = D_0 e^{\frac{E_d}{RT^*}} \tag{4.12}$$

where D_0 is the theoretical maximum diffusion coefficient at infinite temperature and E_d is the activation energy for diffusion, both given as constants. Next, the solute trapping kinetic coefficient β_0 is given by:

$$\beta_0 = \frac{a_0}{D} \tag{4.13}$$

where a_0 is the characteristic atomic diffusion distance. The nonequilibrium partition coefficient k can, finally, be found from:

$$k = \frac{k_0 + \beta_0 V}{1 + \beta_0 V} \tag{4.14}$$

The following step is to find the interface solute concentrations C_L^* and C_S^*. The concentration of the liquid at the interface is found by using the Ivantsov solution giving the dimensionless supersaturation Ω_c defined by Equation (2.20). Ω_c is equal to $I_v(P_c)$, which is a function of the solutal Péclet number P_c, given by:

$$P_c = \frac{Vr}{2D} \tag{4.15}$$

The dimensionless supersaturation is calculated using the Ivantsov function defined as

$$I_v(P_c) = -P_c e^{P_c} E_i(P_c) \tag{4.16}$$

where the exponential integral function $E_i(P_c)$ is calculated from the approximations given in Equations (C.2) and (C.3) in the appendix. LGK reorganize Equation (2.20) to get Equation (2.23) for C_L^* by using the equilibrium partition coefficient. This equation, also used by the LKT model, is given by:

$$C_L^* = \frac{C_0}{1 - (1 - k_0) I_v(P_c)} \tag{4.17}$$

The TLK, BCT, modified TLK, and DA models use this equation with the nonequilibrium partition coefficient as:

$$C_L^* = \frac{C_0}{1 - (1 - k) I_v(P_c)} \tag{4.18}$$

The solute concentration of the solid at the interface, C_S^*, is calculated by using the partition coefficient and the solute concentration of the liquid at the interface as:

$$C_S^* = k_0 C_L^* \tag{4.19}$$

in the LKT model, which does not account for solute trapping, and as:

$$C_S^* = k C_L^* \tag{4.20}$$

in the TLK, BCT, modified TLK, and DA models, which use the Aziz equation to account for solute trapping at the interface.

The LKT and TLK models, then yield the solutal supercooling ΔT_c from Equation (2.19) or:

$$\Delta T_c = m_L (C_0 - C_L^*) \tag{4.21}$$

which is defined for straight liquidus and solidus. The modified TLK model uses the same equation for ΔT_c, but with the nonequilibrium liquidus slope m_L' instead of the equilibrium slope m_L. m_L' is defined by BCT as:

$$m_L' = m_L \frac{1 - k\left(1 - \ln \frac{k}{k_0}\right)}{1 - k_0} \tag{4.22}$$

and the ΔT_c in the TLK model is given as:

$$\Delta T_c = m_L' (C_0 - C_L^*) \tag{4.23}$$

The total supercooling equation is then used to check if $f_1 = V_{guess} - V_{calculated}$ is close to zero. The LKT and TLK models use the total supercooling equation with three components to get f_1 as:

$$f_1 = V_{guess} - \frac{\alpha P_t}{\Gamma}(\Delta T - \Delta T_t - \Delta T_c) \tag{4.24}$$

while the modified TLK model uses a linear kinetic supercooling component given by V/μ in addition to the three components of the total supercooling, so f_1 is given as:

$$f_1 = V_{guess} - \frac{\alpha P_t}{\Gamma}\left(\Delta T - \Delta T_t - \Delta T_c - \frac{V_{guess}}{\mu}\right) \tag{4.25}$$

The f_1 functions in the BCT and DA models take a different form from Equations (4.24) and (4.25). In these models, Turnbull's linear collision-limited growth model, given by Equation (2.52), is used to relate the interface velocity to the Baker-Cahn equation for the interfacial driving force ΔG^*, which after rearranging Equation (2.50), is given by:

$$\Delta G^* = RT^*\left(C_L^* - C_S^* + C_L^* k \ln\frac{k}{k_0} - C_L^{eq} + C_L^{eq}\right) \tag{4.26}$$

Thus, f_1 is given by:

$$f_1 = V_{guess} - \left(-\frac{V_0 \Delta G^*}{RT^*}\right) \tag{4.27}$$

The second equation that needs to be satisfied in all the models is given by $f_2 = r_{guess} - r_{calculated}$. This equation depends on the Trivedi-Kurz marginal stability criterion [16] represented by Equation (2.36) and is used similarly in all the models discussed here except for some differences in the models that include the Aziz equation and adopt the kinetic liquidus slope defined by Equation (4.22). The LKT model does not use the Aziz equation, so f_2 is written as:

$$f_2 = r_{guess} - \frac{\frac{\Gamma}{\sigma}}{\frac{\Delta H_f}{c_p} P_t \xi_t + 2 m_L C_L^* (k_0 - 1) P_c \xi_c} \tag{4.28}$$

In the TLK, BCT, and DA models, the equilibrium partition coefficient, k_0, in the denominator of the second term on the right hand side of Equation (4.28) is replaced with the nonequilibrium partition coefficient, k, as shown below:

$$f_2 = r_{guess} - \frac{\frac{\Gamma}{\sigma}}{\frac{\Delta H_f}{c_p} P_t \xi_t + 2 m_L C_L^* (k - 1) P_c \xi_c} \tag{4.29}$$

In the modified TLK model [20, 21, 22], the liquidus slope m_L is replaced with the kinetic slope m'_L as shown below:

$$f_2 = r_{guess} - \frac{\frac{\Gamma}{\sigma}}{\frac{\Delta H_f}{c_p} P_t \xi_t + 2 m'_L C_L^* (k - 1) P_c \xi_c} \tag{4.30}$$

DA [5] has shown that if straight phase boundaries are assumed, the Trivedi-Kurz stability criterion needs to be used with the equilibrium liquidus slope m_L, otherwise, the slope of a curved liquidus should be determined by taking the derivative of the curve at the given interfacial liquid concentration, say C_L^*, i.e., $\left(\frac{dT_l}{dC_l}\right)_{C_l = C_L^*}$ as done in the DA model.

In all of the free dendritic growth models analyzed in this study, a system of two equations, $f_1(V, r)$ and $f_2(V, r)$, are solved for the two variables V and r, from which the other important solidification parameters are obtained. The next section describes how the models are computed using the formulation shown above.

4.2 Numerical Computation Method

The free dendritic growth models investigated in this study are composed of a multi-coupled, multi-variable system of nonlinear algebraic equations. In this study, these equations are solved using a bisection method with a minimal error iterative algorithm. The system is square with two equations and two unknown variables with varying parameters dependent on the unknowns. The unknown physical system variables are the interface velocity V and the tip radius r. The other varying solidification parameters are dependent on V and r, and all the system parameters interact with each other. The mathematical system can simply be shown as:

$$f_1(V, r) = 0 \tag{4.31}$$

$$f_2(V, r) = 0 \tag{4.32}$$

As the equations are nonlinear and multi-coupled, a numerical solution using a multi-grid iterative method is applied. There are various important factors involved in choosing an appropriate iteration method to approximate the roots of a function, such as the initial values, the rate of convergence, and the complexity of the calculation. In this study, the bisection method is selected because this method is powerful when a range can be set for the initial guess values and when a multi-grid iterative solution is required. Besides, the system in this case is highly coupled and highly complex due to the interaction between the parameters that depend on the unknown variables and that need to be called from external functions. The bisection method is a relatively easy method to apply when the system of equations is complex [47].

The computation starts by assigning initial guess values for the unknown variables, V and r. The initial guess values are bounded with the assigned maximum and minimum values. Assuming that the problem is continuous within the given boundaries, bisection is iterated on two grids, one grid for V and the other for r. The first iteration is used to find the best root for V by changing this variable and keeping r constant until the equation for f_1 is satisfied as shown in Equation (4.31). Then, the solution to f_1 from the first iteration is introduced to f_2 to check r. If Equation (4.32) is satisfied, the solution is found, if not, a new value is assigned for r and the computation runs until the best V and r that satisfy f_1 and f_2 with a minimal error are found. This process is presented in a simple flowchart presented in Figure 4.1.

During each iteration, the step-length is, first, calculated based on the maximum and minimum vales of the unknown variables or on the result from the previous calculation, which is set as one of these boundaries. The iterations are stopped when the error is small enough, i.e., less than ϵ.

For each free dendritic growth model, computation is performed over a range of total supercoolings, ΔT, starting from 1 K to 200 K. For certain values of the constant parameter ΔT, especially in the region described as the transition region, it is possible to observe

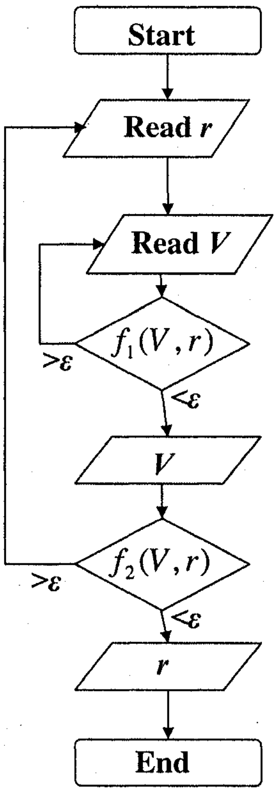

Figure 4.1: Simple flowchart of the computer program for the free dendritic growth models.

a multiple set of roots caused by a jump bifurcation due to the nonlinearity of the mathematical system [48, 49]. Figure 4.2 shows such a region from the total supercooling versus interface velocity graph of the BCT solution for an Ag-15 mass % Cu alloy.

In this case, as the constant parameter ΔT is increased by very small increments, the roots of the function arrive at a vertical tangent. Numerical solution shows that the roots jump to another point, say from P1 to P2 as shown in Figure 4.2, where they can continue moving rightward as ΔT is increased further. This means there is a transient period during which the roots jump from one point to another. Once the roots settle down at the new

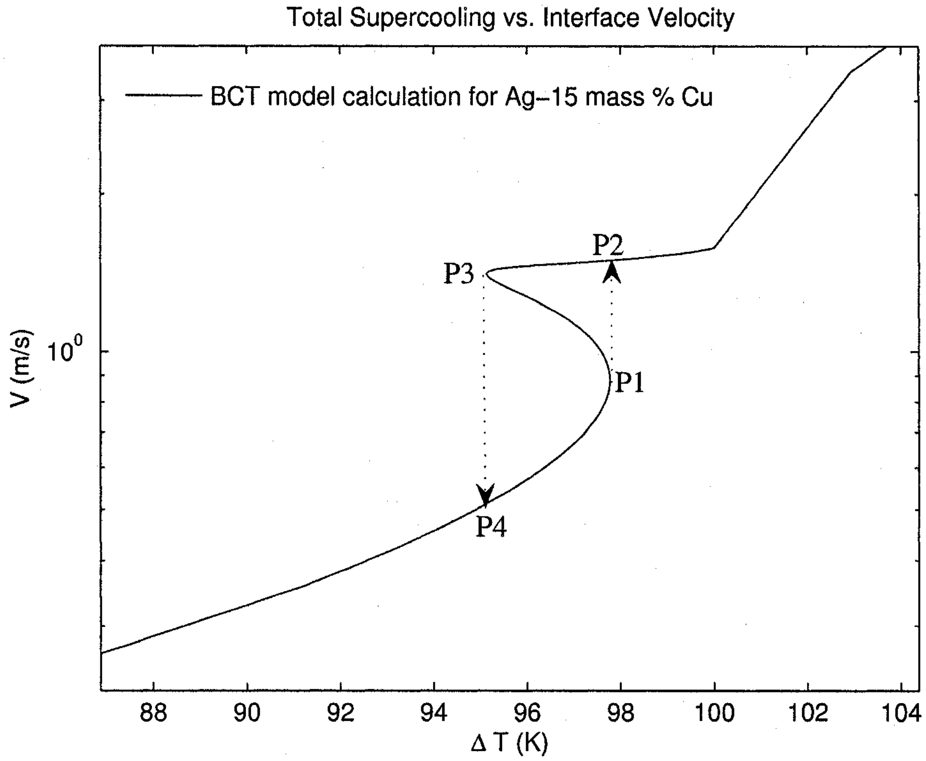

Figure 4.2: Multiple root region showing a jump bifurcation.

point, ΔT can be further increased and the roots continue to move to the right.

Then, running the program backwards by decreasing the ΔT from 200 K to 1 K, when ΔT reaches P2, it does not jump back to P1 but continues to move toward left to another point of vertical tangency at P3. At this point, the roots again make a jump to another point, P4, back on the track obtained in the forward solution, and continue to move leftwards to the starting point. Consequently, continuous variation of the system parameter, ΔT, leads to a discontinuous change in output, namely the jumps in the roots from P1 to P2 and from P3 to P4. There are at least three roots for the values of ΔT between the vertical lines formed by P1-P2 and P3-P4. With such a treatment of the ΔT as described above, the middle branches of the curve that gives the intermediate roots are not accessible [50].

It is possible to start the system for a ΔT in this multiple roots (three or more) region, however, if the initial guess values are not close enough to the roots and if the range between the maximum and minimum values is set too wide, the solution is attracted to a point on the lower branch or on the upper branch, or the computation enters a loop because it can never get close enough to any of the roots due to the setting of the initial values. It is possible to find the real roots only by assigning initial values very close to the actual roots and keeping the step-lengths small.

Consequently, during the computations, it is important to describe a neighborhood of the solution so that the multi-grid iteration is well defined and that the iterates $V(k)$ and $r(k)$ converge to the solution V and r.

4.3 Comparison and Analysis of Computation Results

The LKT, TLK, BCT, modified TLK, and DA models, all originating from the LGK model, are applied to the same alloy with the objective of comparing these free dendritic growth models numerically and illustrating how they differ.

All the models are applied to a Ag-15 mass % Cu alloy. The Ag-Cu system is selected due to the availability of solidification and thermodynamic data. The alloy composition of 15 mass % Cu is selected so that the calculation results for the BCT model can be verified with those calculated and presented by BCT [4] for the same alloy.

For each model, given the alloy composition C_0, the computation is performed over a range of total melt supercoolings, ΔT, between 1 K and 200 K, by using the bisection method in two grids to solve for the interface velocity V and the tip radius r with minimal error for each ΔT chosen. The other important solidification parameters, such as the interface temperature T^*, the interface concentration of the liquid C_L^*, the solute partition coefficient k, and the interface concentration of the solid C_S^*, are calculated for each ΔT from the calculated values of V and r.

4.3.1 General Behavior of Solidification Parameters with Total Melt Supercooling

Figures 4.3 - 4.7 compares the results of calculations of the free dendritic growth in an Ag-15 mass % Cu alloy performed with the LKT, TLK, BCT, modified TLK, and DA models.

Figure 4.3 shows the interface velocity versus the total supercooling. The interface velocity increases nearly parabollicaly with increasing total supercooling, except at about 70 to 100 K supercoolings, occurrence of a transition region is noted for all the models except for the LKT model. Such a transition behavior is observed for all the solidification parameters. The LKT model, which does not account for the kinetics of the interface, does not present such a transition, instead the interface velocity increases almost parabollicaly until 190 K.

Figure 4.4 shows the tip radius versus the total supercooling. The dendrite tip gets

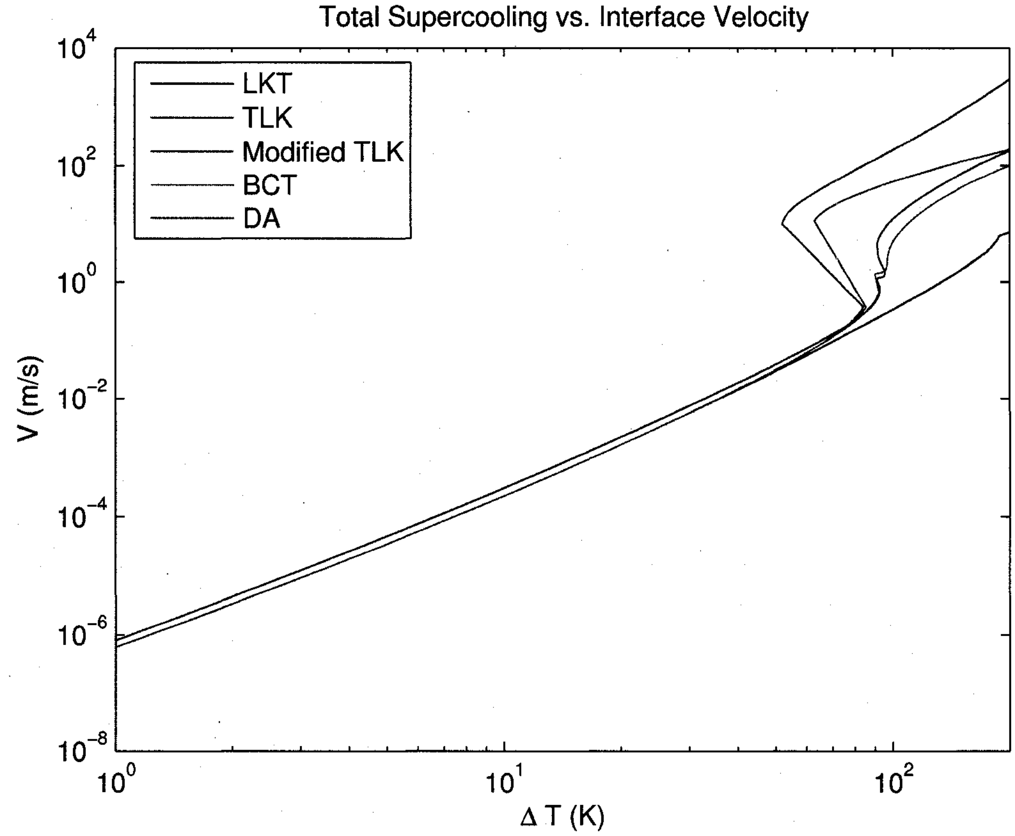

Figure 4.3: Results of free dendritic growth calculations showing the variation of the interface velocity with melt supercoling for Ag-15 mass % Cu.

sharper with increasing melt supercooling, and increasing interface velocity up to the transition region, where the tip rapidly becomes blunter. Then, as the total supercooling is increased, the tip radius decreases again, although the tip does not get as sharp as the stage right before the transition. The LKT model predicts a rapid increase in tip radius to infinity at around 190 K.

Figure 4.5 shows the interface temperature versus the total supercooling relation. The interface temperature decreases with total supercooling until the transition region, where

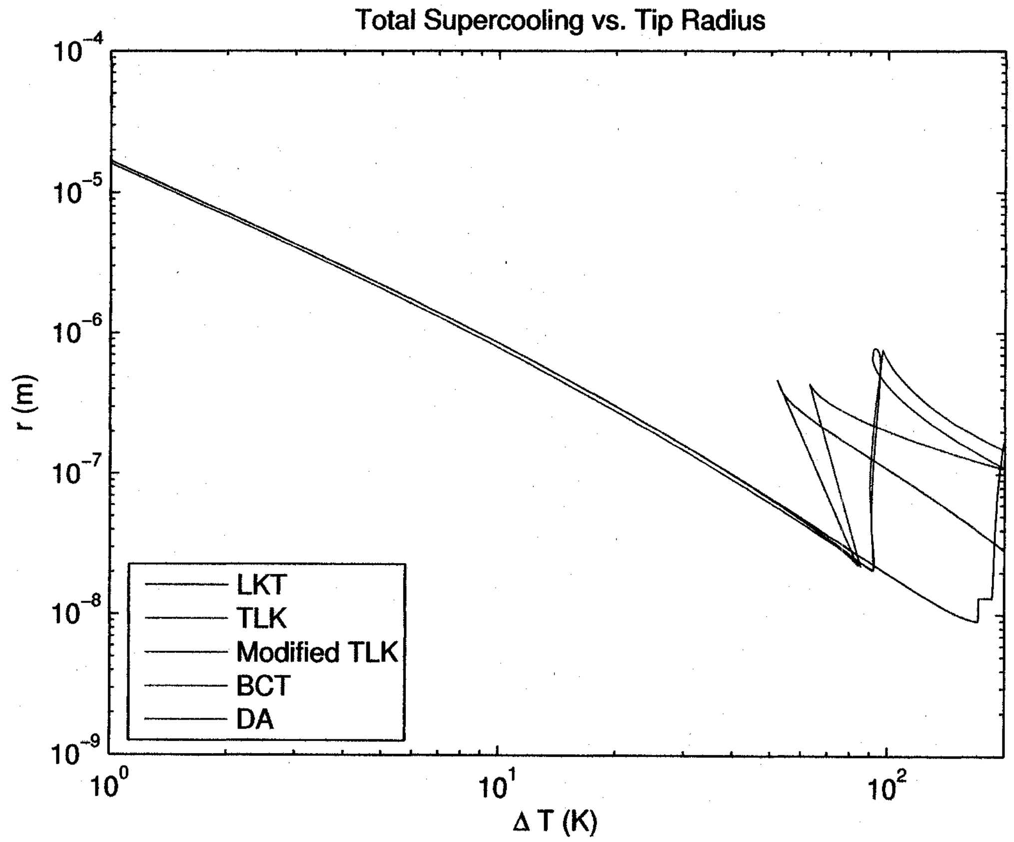

Figure 4.4: Results of free dendritic growth calculations showing the variation of the tip radius with melt supercooling for Ag-15 mass % Cu.

the interface temperature increases rapidly, and then continues to decrease as the total supercooling is increased. The LKT model, which determines the interface temperature simply from heat and mass transport equations without incorporating any interface kinetics or thermodynamic driving force, shows the interface temperature to decrease monotonically with increasing total supercoolings, i.e., decreasing melt temperatures, and to remain almost constant at total melt supercoolings larger than about 190 K.

Figure 4.6 shows the dependence of the interface liquid and solid concentrations on the

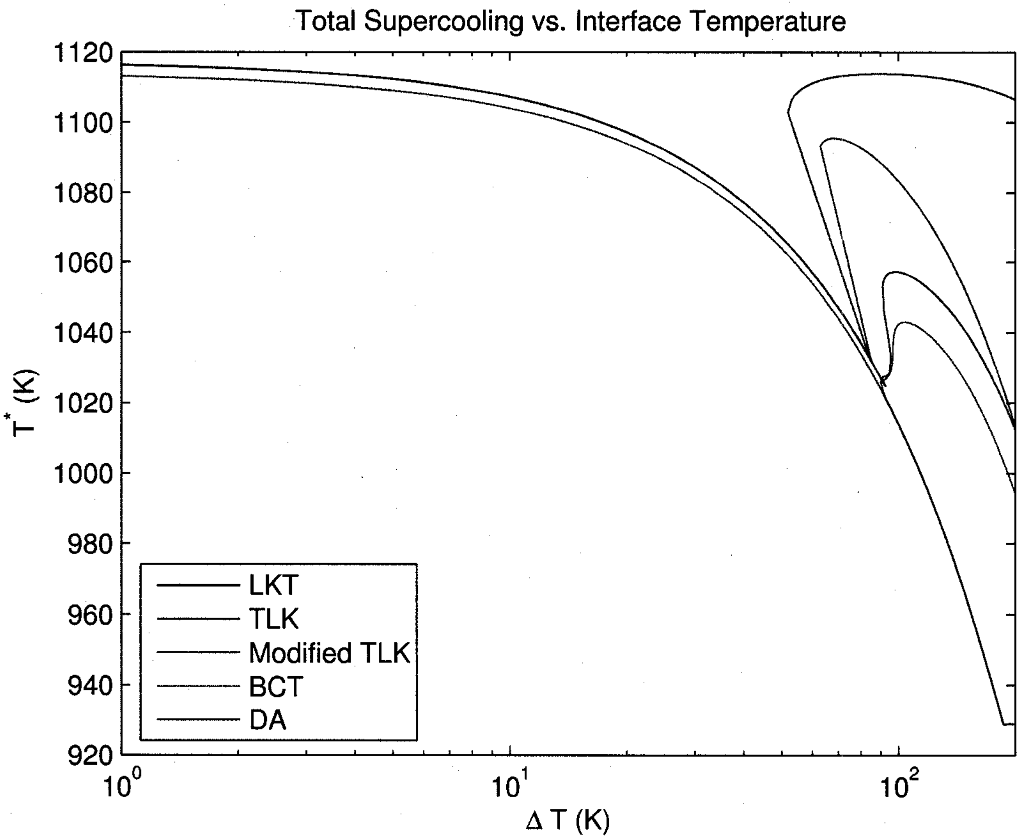

Figure 4.5: Results of free dendritic growth calculations showing the variation of the interface temperature with melt supercoling for Ag-15 mass % Cu.

total supercooling. For all models, the calculations are performed using molar fractions, where the alloy concentration of 15 mass % Cu corresponds to 0.23 mole fraction of Cu. The concentration of the copper in solid is around 0.09 in mole fraction at low melt supercoolings, the value that corresponds to k_0C_0, and rises rapidly to 0.23 mole fraction Cu in the transition region, then remains constant. Thereafter the interface concentration of the liquid is equal to that of the melt for low melt supercoolings, rises to higher concentrations around 0.43 for the DA model and 0.36 for the TLK, BCT, and modified TLK models in

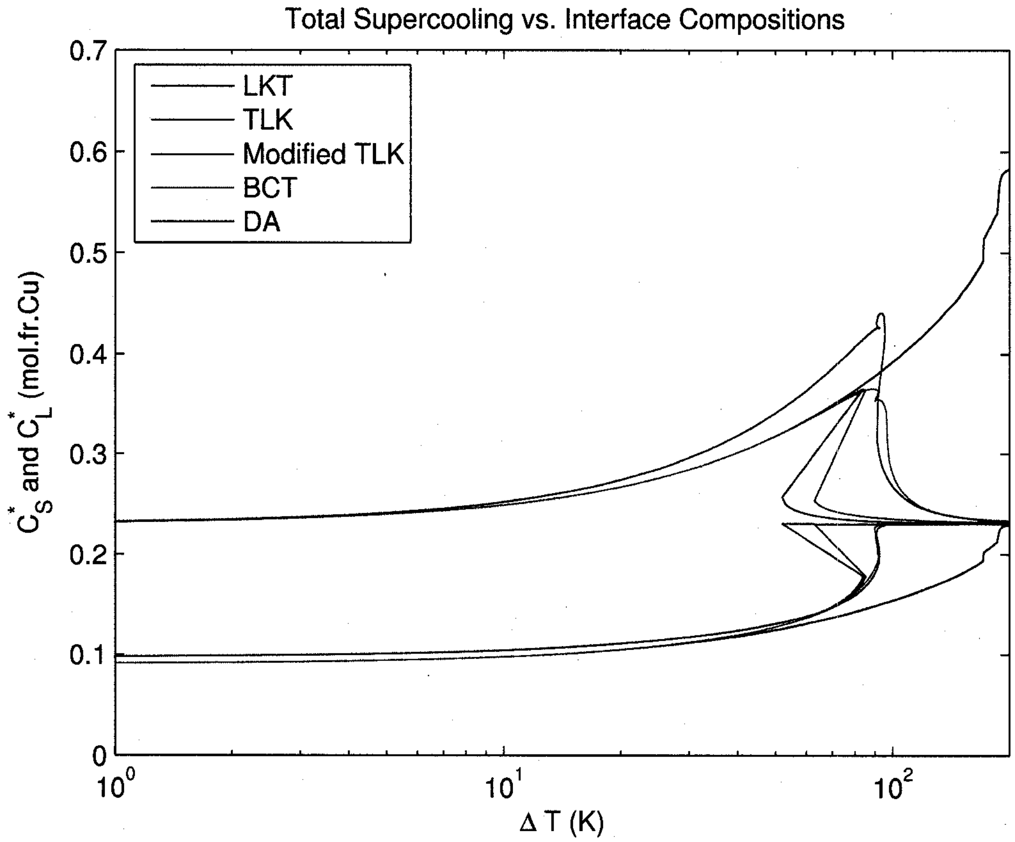

Figure 4.6: Results of free dendritic growth calculations showing the variation of the interface concentrations of the liquid and the solid with melt supercoling for Ag-15 mass % Cu.

the transition region, then drops rapidly to 0.23, the copper concentration of the alloy.

The LKT model predicts a monotonic increase in copper interface concentration of the liquid as this model does not employ a solute trapping model. As a result, the latter model shows a higher increase in liquid concentration up to 0.58 at around 190 K, above which the concentration remains constant.

Thus, all the models, except LKT show that solute partitioning decreases drastically at supercoolings above the transition region.

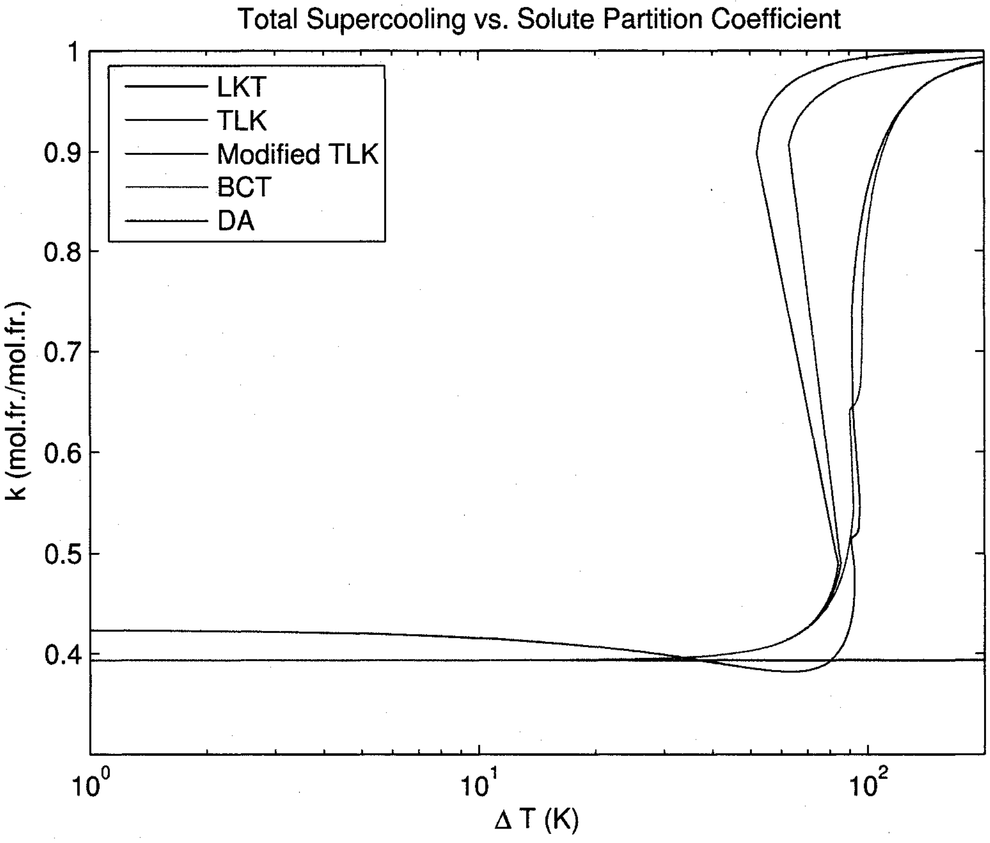

Figure 4.7: Results of free dendritic growth calculations showing the variation of the solute partition coefficient with melt supercooling for Ag-15 mass % Cu.

Figure 4.7 shows the dependence of the solute partition coefficient on the total supercooling. In the models that account for the solute trapping at the interface, the interface partition coefficient jumps sharply toward unity in the transition region, indicating partitionless solidification may take place at the dendrite tip at high supercoolings. The LKT model does not predict such a jump in the solute partition coefficient. In fact, it predicts a constant solute partition coefficient due to the omission of interface kinetics at the assumption of linear liquidus and solidus.

Figure 4.7 also shows that, due to the use of the curved phase boundaries for the equilibrium concentration values of the liquid and the solid, the partition coefficient calculated with the DA model decreases somewhat with increasing ΔT above the transition region.

4.3.2 Transition Region

Figures 4.3 to 4.7 show that the free dendritic growth models work similarly for low supercooling values as the solutions are consistent for all the models in this region. However, the free dendritic growth parameters calculated using the TLK, BCT, modified TLK, and DA models take different values in the transition region of total supercoolings. This transition region, or the solutal-to-thermal transition region, represents the transition from the solute diffusion-limited growth at low supercoolings to the thermal diffusion-limited growth at high supercoolings.

The solutal-to-thermal transition starts at about 50 K for the TLK model and at about 60 K for the modified TLK model, and extend to about 85 K below the starting temperature. The transition region for the BCT and DA models is observed between 90 K and 100 K. The transition region for the TLK and modified TLK models is wider than that for the BCT and DA models. This is due to the fact that the BCT and DA models correctly account for the kinetics and the thermodynamic driving force at the interface further constraining the system, whereas, the TLK model does not account for the latter two. Similarly, the modified TLK model only replaces the equilibrium slope with a kinetic slope defined by BCT and adds a kinetic supercooling component, but it does not use the collision-limited linear growth equation to actually incorporate the thermodynamic driving force as explained in Chapter 2.

The calculation results obtained using the LKT model for supercoolings of 1 to 200 K do not exhibit any obvious solutal-to-thermal transition as this model does not account for any interface kinetics.

4.3.3 Effects of Solute Trapping

At high supercoolings, the dynamics at the dendrite tip are such that there is not enough time for solute diffusion to take place between the two phases at the interface. Consequently, the solute remains trapped in the solid as the solidification front advances into the liquid. This means that the interface concentrations of the solid and the liquid cannot be adjusted to the local equilibrium values and as a result they attain nonequilibrium values determined by the kinetics.

Figure 4.7 shows that the solute partition coefficient calculated with the models that incorporate the Aziz solute trapping equation increases very sharply toward unity in the solutal-to-thermal transition region. The value of k becomes unity, when the melt freezes so fast that all of the solute is trapped in the growing solid without leaving time for solute redistribution, and consequently $C_S^* = C_L^*$. This is called partitionless or massive solidification.

Figure 4.4 shows that at low supercoolings, where the solute diffusion is the dominant rate-controlling step, the dendrite tip is blunt. As the total supercooling increases requiring higher growth rates, the tip gets sharper to allow for more effective diffusion of the rejected solute in the liquid, which becomes more difficult due to the relatively small value of mass diffusion coefficient compared with the large thermal diffusion coefficient. As the total supercooling is increased, thermal diffusion control dominates over mass diffusion control and ultimately partitionless solidification sets in. In the transition region, as solute trapping increases and, hence, the need for solute rejection decreases, where the thermal diffusion field is much larger than that for mass diffusion, the sharp tip is replaced with a blunt tip to adjust for the thermal control regime. The latter transition is not predicted by the LKT model, which does not employ the Aziz equation that relates the solute partition coefficient to the interface velocity.

4.3.4 Effects of Curved Phase Boundaries versus Straight Phase Boundaries

Using the straight phase boundaries assumption introduces a limitation to the free dendritic growth models as the linear approximation is often only appropriate for low supercoolings and curved metastable extensions do exist at higher supercoolings for most binary systems.

Figure 4.8 shows the curved liquidus and solidus for the Ag-Cu system calculated with

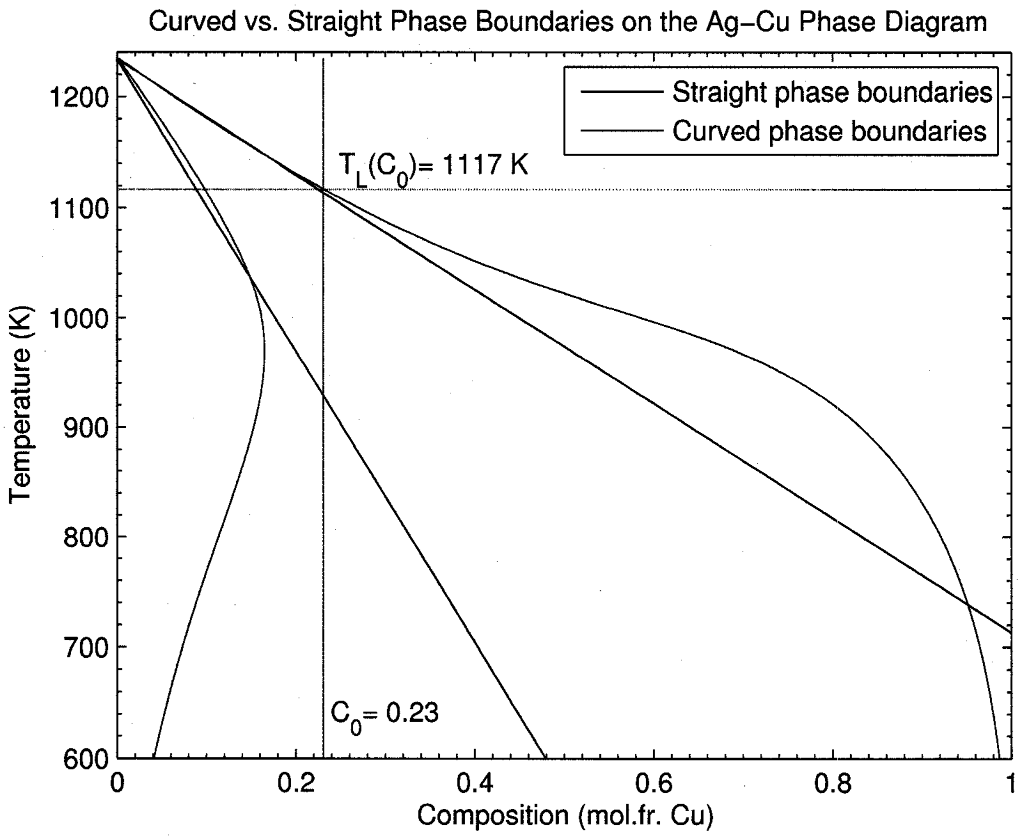

Figure 4.8: Ag-rich part of the Ag-Cu metastable phase diagram showing curved and straight liquidus and solidus.

the temperature dependent subregular solution model developed in this study (see Chapter 3) and the straight liquidus and solidus used by BCT [4]. This figure shows that the straight liquidus and solidus coincide with the curved liquidus and solidus between the melting temperature of pure Ag and the liquidus temperature of the alloy at a Cu mole fraction of 0.23, the concentration of Cu in the alloy they studied. However, below that temperature the assumed straight liquidus deviates from the actual (curved) liquidus and the deviation becomes significant as the supercooling increases.

The LKT, TLK, and the BCT models all assume straight phase boundaries, whereas the DA model extends the BCT model by adopting curved phase boundaries from a metastable phase diagram calculated using a thermodynamic solution. Figure 4.9 shows that in the region before the transition region, the interface liquid concentrations calculated with the BCT model deviate significantly from those of the curved liquidus, but remain close to those of the straight liquidus assumed by BCT as a result of the deviation of the straight phase boundaries from the actual curved phase boundaries. The results of the DA model follow closely the curved liquidus and solidus.

As the curved phase boundaries affect the interface concentrations of the liquid and solid at low supercoolings and in the transition region, they also affect the solute partition coefficient given by C_S^*/C_L^*. Figure 4.7 clearly shows that the partition coefficient given by the DA model decreases slowly with increasing total supercooling above the transition region, whereas in the other models except for the LKT model, it remains constant until the transition is reached.

In all the latter models, the interfacial concentrations deviate from the liquidus and the solidus with the achievement of high enough growth rates at high supercoolings to ultimately yield partitionless formation of the solid with the same composition as that of the liquid. The deviation of the interfacial concentrations from the phase boundaries occurs largely over the temperature range that corresponds to the region for solutal-to-thermal transition.

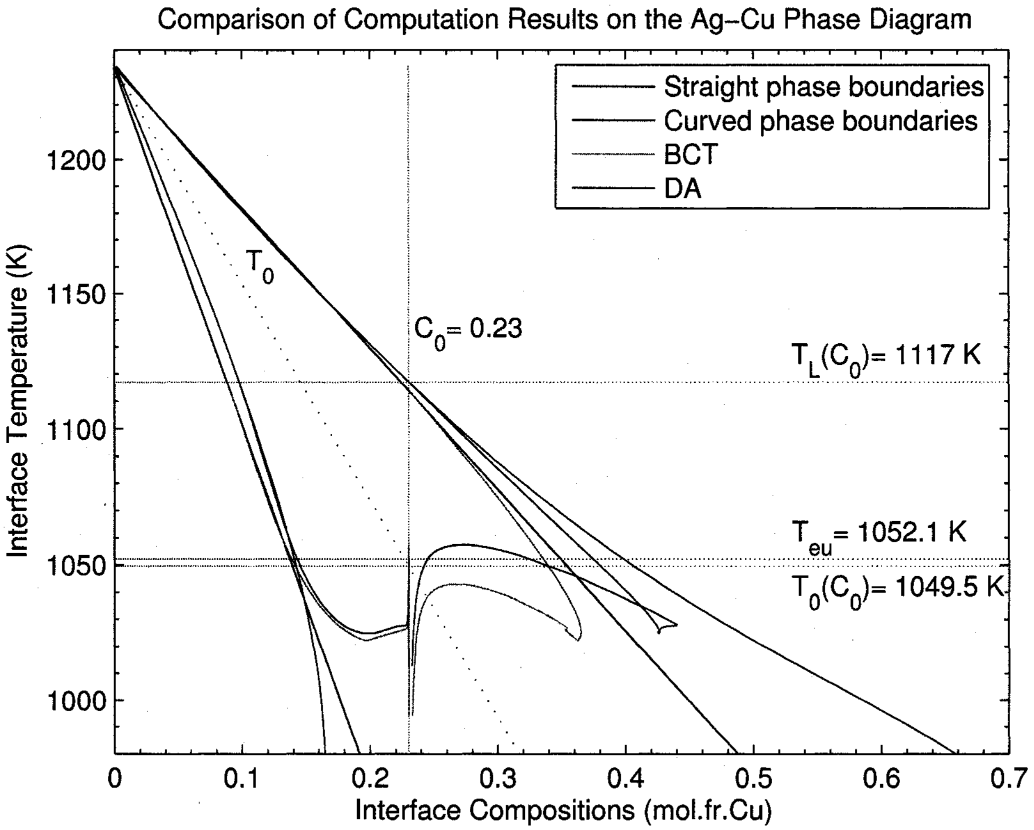

Figure 4.9: Comparison of the BCT and DA model solutions with respect to the curved and straight liquidus and solidus on the Ag-rich part of the Ag-Cu metastable phase diagram.

The transition regions of the BCT and DA models both start at a supercooling around 90 K. This is roughly 1027 K and is below the T_0 temperature. For the Ag-0.23 mole fraction Cu alloy, T_0 is calculated as 1050 K using the approximate equation given by BCT [4]. The transition is expected to start near the T_0 temperature. Full transition to thermal control, i.e., massive solidification, requires that $T^* < T_0$ by an amount V/μ according to the BCT model [4, 36]. The TLK and modified TLK models predict much earlier occurence of the transition region starting above the T_0 temperature. The latter prediction, however, is not correct as these models do not account for the interfacial driving force which needs to be significant to allow the interfacial concentrations to deviate significantly from the local equilibrium values.

4.3.5 Effects of Linear Kinetics and Thermodynamic Driving Force at the Interface

It is shown in Figure 4.9 that at low supercoolings, the interface concentrations are close to the local thermodynamic equilibrium concentrations defined by the liquidus and solidus. Therefore, it is appropriate to assume local equilibrium conditions for such cases, where the interface migration is governed by the mass transport in the liquid, i.e., no interfacial driving force is required. On the other hand, for higher values of supercooling, where the dendrite tip attains a high growth rate, there is not sufficient time for atom rearrangement to maintain local equilibrium concentrations at the interface. Therefore, the interface concentrations deviate from the equilibrium values defined by the solidus and liquidus. In such cases, the interface temperature and the nonequilibrium interfacial concentrations should be determined by the kinetics at the solid-liquid interface, which also depend on the amount of the thermodynamic driving force as indicated in the linear collision-limited kinetic model by Turnbull [19].

The BCT and DA models correctly integrate the interface kinetics and the thermodynamic driving force in the free dendritic growth models. This treatment allows to find a more correct value for the interface temperature by assigning a thermodynamically driven growth velocity and more appropriate values for the interface concentrations that are limited by the thermodynamic force, thus narrowing the transition region.

The following chapter presents a new model that is obtained by further incorporating a thermodynamic solution model in the DA model in order to calculate the interfacial driving force ΔG^* rather than using the Baker-Cahn equation, which is based on Henrian conditions.

Chapter 5

A Modification of the DA Model by Incorporation of a Thermodynamic Solution Model

5.1 Background for Development of the Model

In rapid solidification processes, such as spray forming, the melt is cooled well below the melting temperature often causing the formation of dendrites in the melt. Predicting the microstructure of such crystals requires a free dendritic growth model that applies to high supercoolings and crystal growth rates for alloys, whether dilute or concentrated. However, current free dendritic growth models are restricted to low supercoolings and growth rates, or dilute solutions, or all. Therefore, one of the objectives of this thesis is to show that some of these restrictions can be removed by modifiying the free dendritic growth models.

An early free dendritic growth model, the LGK model [9, 15] for a paraboloidal tip, applies only to small Péclet number conditions as it assumes local equilibrium at the solid-liquid interface at the dendrite tip. The other free dendritic growth models discussed in this thesis are developed with an intention to modify the LGK model to high supercoolings and growth rates, i.e., large Péclet number conditions.

LKT [2] modified the LGK model by applying the Trivedi-Kurz [16] marginal stability criteria, which is suitable for high interface velocities, instead of the marginal stability criteria given by Trivedi [14], and Kurz and Fisher [13]. The LKT model is regarded as still assuming local equilibrium interface conditions as the interface kinetics are omitted in the total supercooling.

The subsequent TLK model [3] included the effect of interface kinetics through a growth rate dependent partition coefficient, but neglected the kinetic effects on the total supercooling as done in the LKT model. The omission of the kinetic supercooling, however, necessitates the use of the equilibrium interfacial composition for the liquid as the interface temperature and velocity that determine the liquid composition do not reflect any kinetic effects.

BCT [4] modified these models by correctly addressing the inclusion of nonequilibrium interface kinetics. The BCT model introduces an interfacial driving force for dendritic growth, correctly relates it to the interface velocity and includes a kinetic supercooling component in the total supercooling. The BCT model assumes straight phase boundaries as done in the previous models, which may not be appropriate for high supercoolings.

The DA model [5] modifies the BCT model successfully by incorporating curved phase boundaries in formulating the interfacial driving force in accordance with the procedure of the BCT model. The DA model also addresses the kinetic component correctly in defining the total supercooling. In addition, it shows Trivedi-Kurz stability criteria to apply to the dendritic growth in a system with curved phase boundaries, even at a high supercooling, where the kinetic component is significantly large.

Table 5.1 provides a summary of the features of the free dendritic growth models discussed in this thesis and shows the modifications made in the later models. These free dendritic growth models are applicable only to the case of very dilute alloys due to the modifications added to extend the LGK model. The interfacial driving force for dendritic growth, which is addressed correctly in the BCT and DA models, is given by the Baker and Cahn [17] expression for the change in free energy per mole of liquid which is restricted to Henrian solutions.

Table 5.1: Free Dendritic Growth Models for a Paraboloidal Tip

Model	*Stability Criterion*	*Equilibrium Condition*	*Solute Distribution*	*Driving Force*	*Kinetics*
LGK 1984	Trivedi, Kurz-Fisher (Small P)	Local eqlb., Liquidus slope Straight solidus-liquidus	Eqlb. solute partitioning	No solidification thermodynamics	None
LKT 1987	Trivedi-Kurz (All P)	Local eqlb., Liquidus slope Straight solidus-liquidus	Eqlb. solute partitioning	No solidification thermodynamics	None
TLK 1987	Trivedi-Kurz (All P)	Local eqlb., Liquidus slope Straight solidus-liquidus	Growth rate dependent solute partitioning (Aziz eqn.)	No solidification thermodynamics	None
BCT 1988	Trivedi-Kurz (All P)	Noneqlb. conditions Kinetic slope Straight solidus-liquidus	Growth rate dependent solute partitioning (Aziz eqn.)	Baker-Cahn expression simplified for straight phase boundaries	Linear kinetic law, ΔT_k
Modified TLK	Trivedi-Kurz (All P)	Noneqlb. conditions Kinetic slope applied incorrectly	Growth rate dependent solute partitioning (Aziz eqn.)	No solidification thermodynamics	ΔT_k for pure metal
DA 1998	Modified Trivedi-Kurz (All P)	Noneqlb. conditions Slope of curved liquidus Curved solidus-liquidus	Growth rate dependent solute partitioning (Aziz eqn.)	Simplified Baker-Cahn expression corrected for curvature	Linear kinetic law, ΔT_k
New Model	Modified Trivedi-Kurz (All P)	Noneqlb. conditions Slope of curved liquidus Curved solidus-liquidus	Growth rate dependent solute partitioning (Aziz eqn.)	Thermodynamic solution model	Linear kinetic law, ΔT_k

Therefore, in this thesis, the DA model is extended by incorporating a thermodynamic solution model for the calculation of the driving force at the dendrite tip, thereby, eliminating the Henrian restriction of the Baker-Cahn equation.

5.2 Modification Scheme

The new free dendritic growth model is similar to the free dendritic growth models presented in Table 5.1, where a set of two equations are solved for the interface velocity and the tip radius, from which the other solidification parameters such as the interface temperature and concentrations are calculated.

The new model depends on the same computation scheme that is used for the DA model as described in Section 4.1, except for the calculation of the interfacial driving force. The DA model employs the Baker-Cahn expression that represents the change in molar free energy across the interface given by Equation (2.49). This expression is further simplified and rearranged by BCT for the assumptions of straight phase boundaries and dilute solution, and then proved by DA to apply to curved phase boundaries, and is given by:

$$\Delta G^* = RT^* \left(C_L^* - C_S^* + C_L^* k \ln \frac{k}{k_0} - C_L^{eq} + C_L^{eq} \right) \tag{5.1}$$

In the DA model, this equation is easily used to find ΔG^* with the calculated values of $T^*, C_L^{eq}, C_S^{eq}, k_0, C_S^*, C_L^*,$ and k, where the equilibrium concentrations are obtained using polynomial functions to represent the curved liquidus and solidus in the calculated phase diagram as well as the curvature supercooling ΔT_r that shifts the liquidus for the curved solid-liquid interface.

The new model employs a thermodynamic solution model to calculate the molar free energies of the solid and liquid phases represented by G^{α} and G^{L} as described in Chapter 3. ΔG^{*} is defined as the difference between the molar free energy of the solid and the liquid at the interface, and is given by:

$$\Delta G^{*} = G^{\alpha *} - G^{L*} \tag{5.2}$$

where $G^{\alpha *}$ and G^{L*} represent the molar free energy of the solid and the liquid at the interface.

As the dendrite tip is curved at the interface, its free energy is increased due to capillary effects by ΔG_r. Consequently, the molar free energy of the solid for the curved interface is given by:

$$G^{\alpha *} = G^{\alpha} + \Delta G_r^{\alpha} \tag{5.3}$$

where G^{α} is the molar free energy of the solid for a flat solidification front. Any curvature effects in the liquid are neglected assuming the liquid is infinitely large compared to the solid [7, 6]. Thus, G^{L*} is assumed equal to G^{L}. Consequently, ΔG^{*} is given by:

$$\Delta G^{*} = G^{\alpha} + \Delta G_r^{\alpha} - G^{L} \tag{5.4}$$

The values of G^{α} and G^{L} are obtained by calling external functions that yield the free energy curves for the solid and the liquid. These functions are dependent on the constant parameters of the temperature dependent subregular solution model, $A^{L}, B^{L}, \tau^{L}, A^{\alpha}, B^{\alpha}, \tau^{\alpha}$, calculated for the Ag-Cu system as described in Chapter 3. ΔG^* is then calculated with the free energy functions as explained in Section 5.3 using the interface temperature T^*, the interface concentrations C_L^* and C_S^* of the liquid and the solid, and the radius of curvature r.

ΔG^*, thus calculated using a thermodynamic solution model and data as well as the calculated solidification parameters from the dendritic growth model, is substituted in the collision-limited linear kinetic equation given by Turnbull [19] in Equation (2.52), as also done in the BCT and DA models, to find the interface velocity V. The calculated velocity is then compared with the initial-guess velocity to find $f_1(V,r)$, given by:

$$f_1(V,r) = V + V_0 \frac{\Delta G^*}{RT^*} \tag{5.5}$$

The computation is iterated with new guess values of V until $f_1(V,r)$ is smaller than the preset minimal error ϵ. Figure 5.1 shows the computation scheme with the modification for the interfacial driving force. The final values of the interface velocity and the tip radius are found by the two-grid iteration of these variables until both $f_1(V,r)$ and $f_1(V,r)$ are satisfied within the minimal error limit.

5.3 Calculation of the Interfacial Driving Force

The change in free energy across the solid-liquid interface is calculated using the general thermodynamic equilibrium rule for a closed heterogeneous system as explained elsewhere

[7, 17], which is also referred to as the tangent-to-tangent rule, given by:

$$\Delta G^* = (1 - C)(\mu_1^\alpha - \mu_1^L) + C(\mu_2^\alpha - \mu_2^L) \tag{5.6}$$

where μ is the chemical potential of the species shown by 1 and 2 in the solid α or liquid L phase, and C is the mole fraction of the component that transforms from one phase to the other. In the treatment of the interfacial driving force for free dendritic growth, this becomes a tangent-to-curve rule given by:

$$\Delta G^* = (1 - C_S^*)(\mu_1^{\alpha'} - \mu_1^L) + C_S^*(\mu_2^{\alpha'} - \mu_2^L) \tag{5.7}$$

as the solute concentration of the transformed component is the same as the solid phase at the interface, i.e., $C = C_S^*$. $\mu_1^{\alpha'}$ and $\mu_2^{\alpha'}$ are the increased chemical potentials of component 1 and 2 in the solid phase for the curved interface at the dendrite tip. This equation can be represented graphically on the free energy curves as shown in Figure 5.2. Using Figure 5.2, the interfacial driving force is calculated at C_S^* and is found by the difference between the shifted molar free energy of the solid and the tangent to molar free energy curve of the liquid drawn at C_L^*.

$$\Delta G^* = G^\alpha(C_S^*) + \Delta G_r^\alpha - g^L(C_S^*) \tag{5.8}$$

where G^α is the molar free energy of the solid, ΔG_r^α is the increase in molar free energy of the solid phase due to curvature, g^L represents the equation of the line tangent to the free energy curve of the liquid at C_L^*, and $g^L(C_S^*)$ is the value of this tangent line at C_S^*.

$G^{\alpha}(C_S^*)$ can be calculated using the interface temperature and concentration of the solid, T^* and C_S^*, from the free dendritic growth computation together with the constant parameters of the thermodynamic solution model, $A^L, B^L, \tau^L, A^{\alpha}, B^{\alpha}, \tau^{\alpha}$.

ΔG_r^{α} is given by:

$$\Delta G_r^{\alpha} = \frac{2}{r}\Gamma \Delta S_{f1} \tag{5.9}$$

where Γ is the interface energy per unit area and ΔS_{f1} is the molar entropy of fusion of pure component 1 (solvent). $g^L(C_S^*)$ is found by first writing the equation of the tangent line g^L. Taking the derivative of the molar free energy curve for the liquid phase, G^L, at the interface concentration of the liquid C_L^*, i.e., $\left(\frac{dG_L}{dC_2}\right)_{C_L^*}$, gives the slope of the tangent line that passes through C_S^*. The equation of the tangent is written using the 'point-slope' form of a line given by:

$$g^L(C_S^*) - G^L(C_L^*) = \left(\frac{dG_L}{dC_2}\right)_{C_L^*}(C_S^* - C_L^*) \tag{5.10}$$

Calculating the equation for the molar free energy curve of the liquid and its derivative at C_L^* and substituting these values in Equation (5.10) gives the value of the tangent line at C_S^*, i.e., $g^L(C_S^*)$.

Finally, using the calculated values of $G^{\alpha}(C_S^*)$, ΔG_r^{α}, and $g^L(C_S^*)$ in Equation (5.8) yields ΔG^*. Figure 5.3 presents a graphical representation for the calculation of the interfacial driving force.

5.4 Computation Results and Comparison With Those From the BCT and DA Models

The computation results for the new model along with the results for the LKT, TLK, modified TLK, BCT and DA models are presented in Figures 5.4 - 5.8 for total supercooling versus important solidification parameters such as interface velocity, tip radius, partition coefficient, interface concentrations of the solid and the liquid, and the interface temperature.

The new model differs from the DA and BCT models with the incorporation of a thermodynamic model to calculate the interfacial driving force instead of the Baker-Cahn equation and it employs curved phase boundaries like the DA model instead of the straight phase boundaries used in the BCT model. The effects of the interfacial free energy calculation on the solidification parameters for the three models are graphically presented in Figures 5.9 - 5.15.

The computation results for the new model are similar to those of the BCT and DA models, and closer to the DA model due to the use of the curved phase boundaries especially recognizable from the behavior of the partition coefficient with the total supercooling presented in Figure 5.5 and with the interfacial driving force presented in Figure 5.15, where the DA model and the new model are shown to depart slightly only in the transition region.

Overall, the figures that show the interface concentration, interface temperature, and total supercooling relation with the interfacial free energy address the deviation of the new model from the DA model more clearly. Figures 5.11 and 5.10 show that the new model and the DA model results coincide for low total supercoolings proving the validity of the Baker-Cahn relation in this region; however, the results diverge in the transition region and at higher supercoolings. Figures 5.12, 5.13, 5.14, and 5.15 show the effect of the interfacial driving force on the interface concentrations and the partition coefficient, which present a deviation especially in the solutal-to-thermal transition area.

Consequently, the validity of the Baker-Cahn equation is proved for low supercoolings, however a another model, such as the thermodynamic solution model used in this work, should be used to define the molar free energies of the solid and the liquid phase for application at high supercoolings.

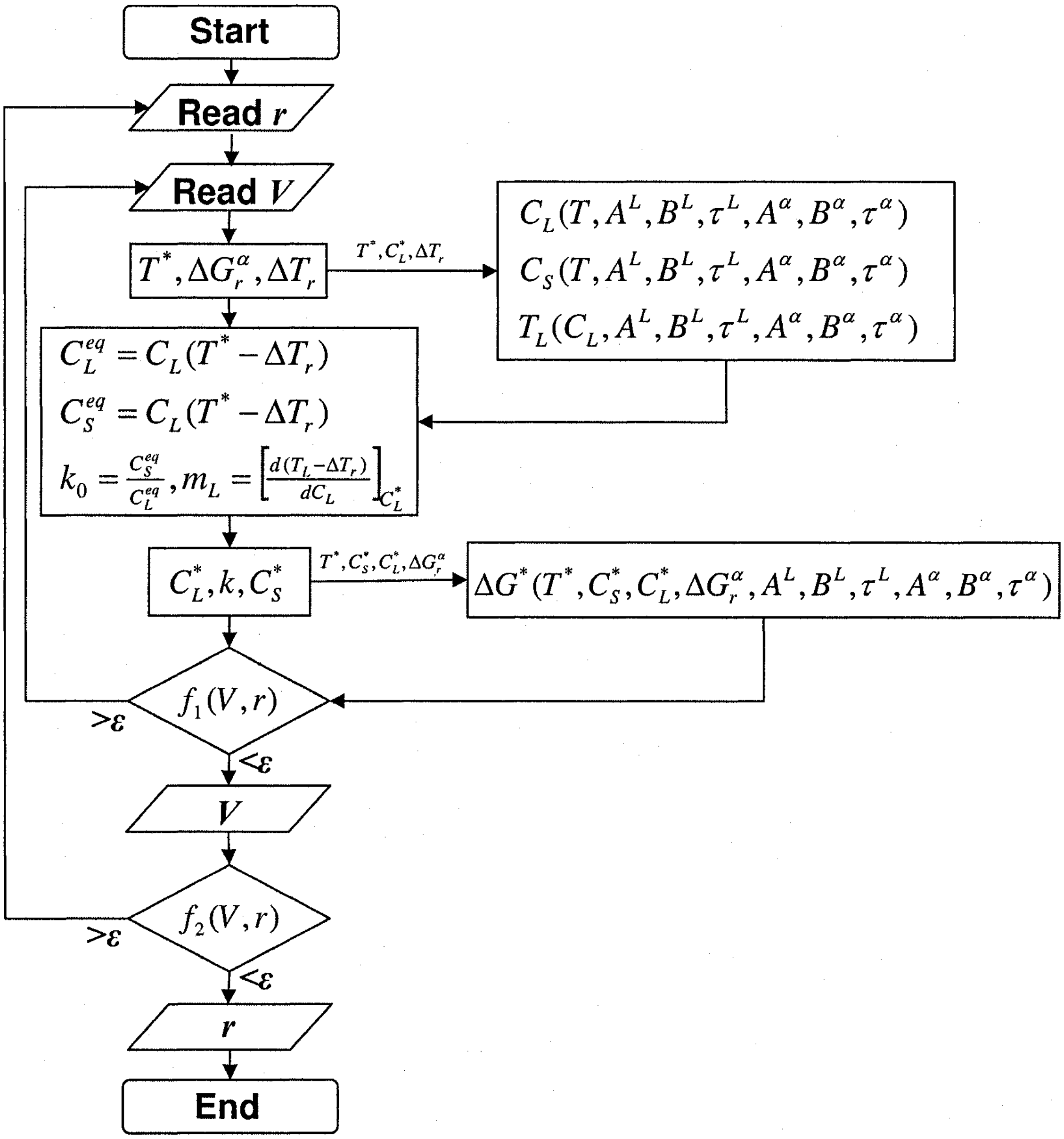

Figure 5.1: Flowchart showing the computation of the new model with the modification for the interfacial driving force calculation.

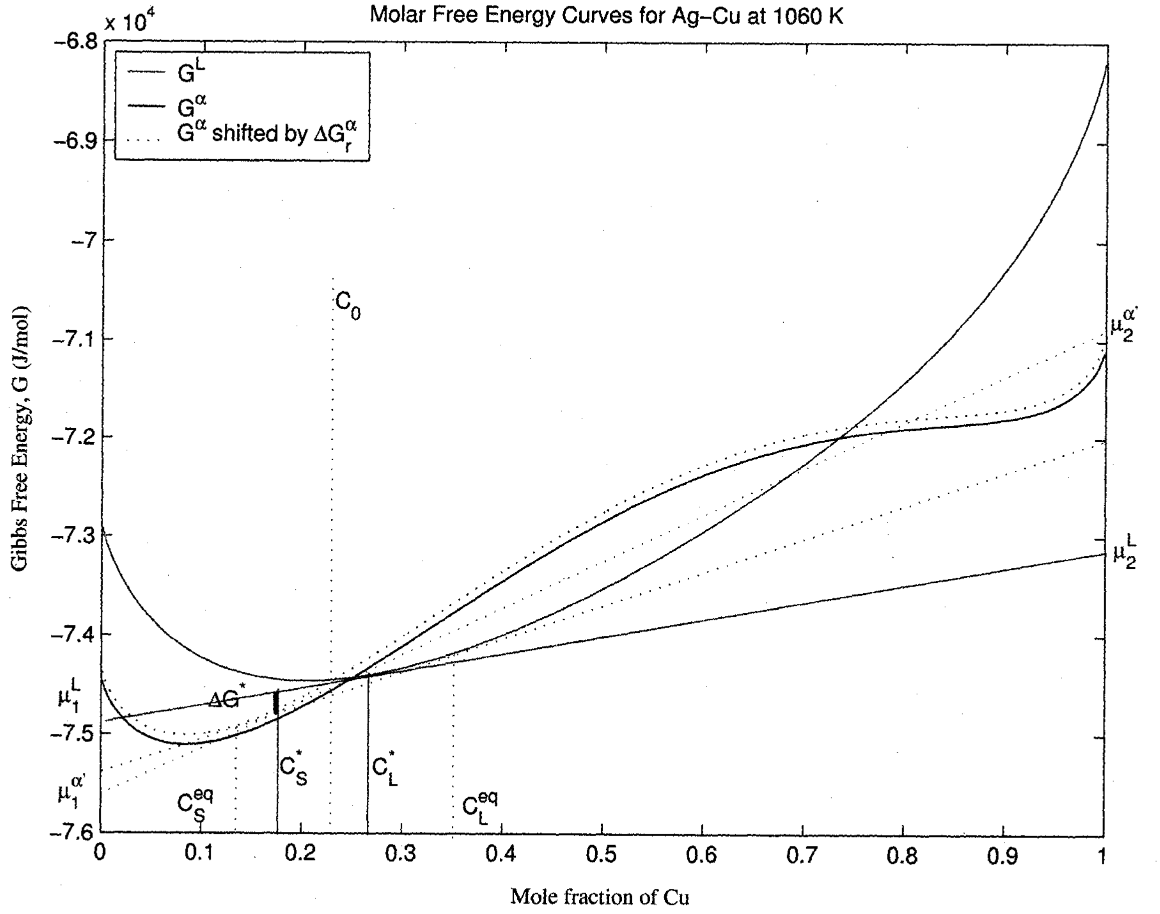

Figure 5.2: Molar Free energy curves for the liquid and solid phases at T^* showing the interfacial driving force ΔG^*.

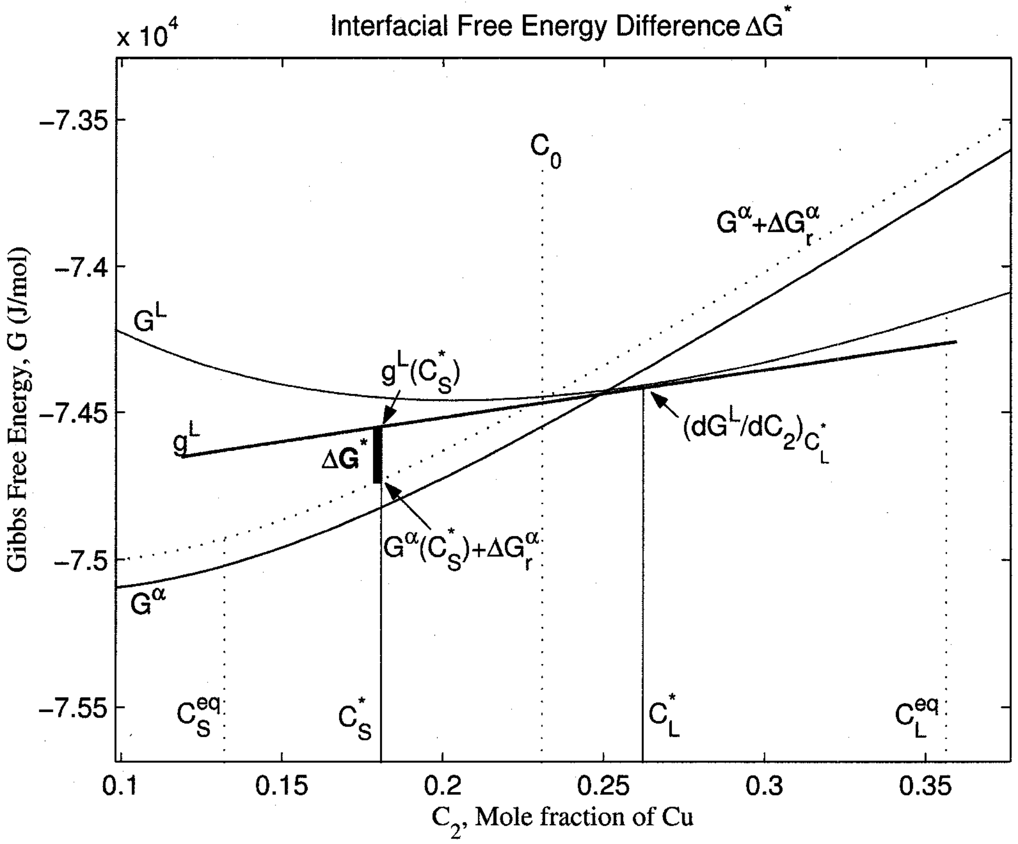

Figure 5.3: Part of the free energy curves given in Figure 5.2 showing the calculation of the interfacial driving force ΔG^*.

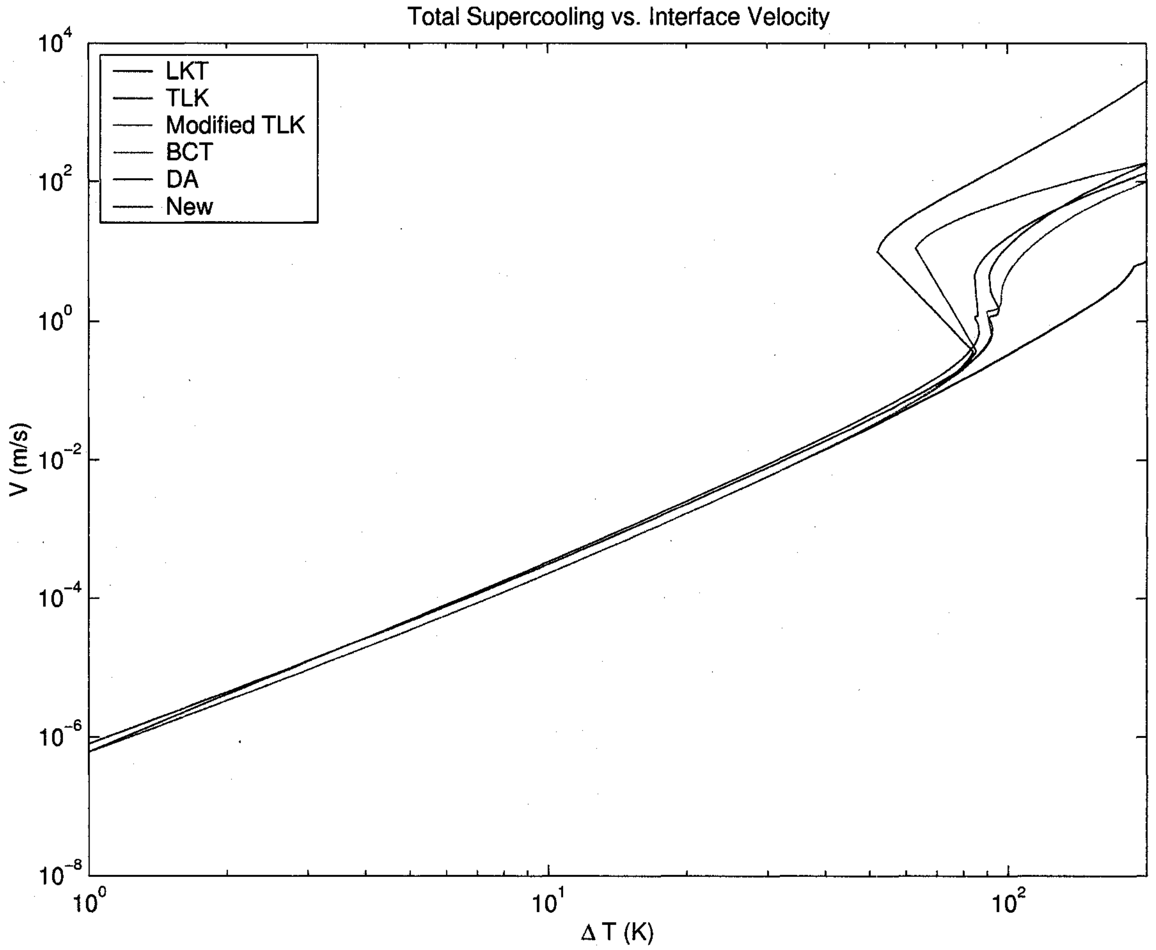

Figure 5.4: Results of free dendritic growth calculations showing the variation of interface velocity with total supercooling for Ag-15 mass % Cu.

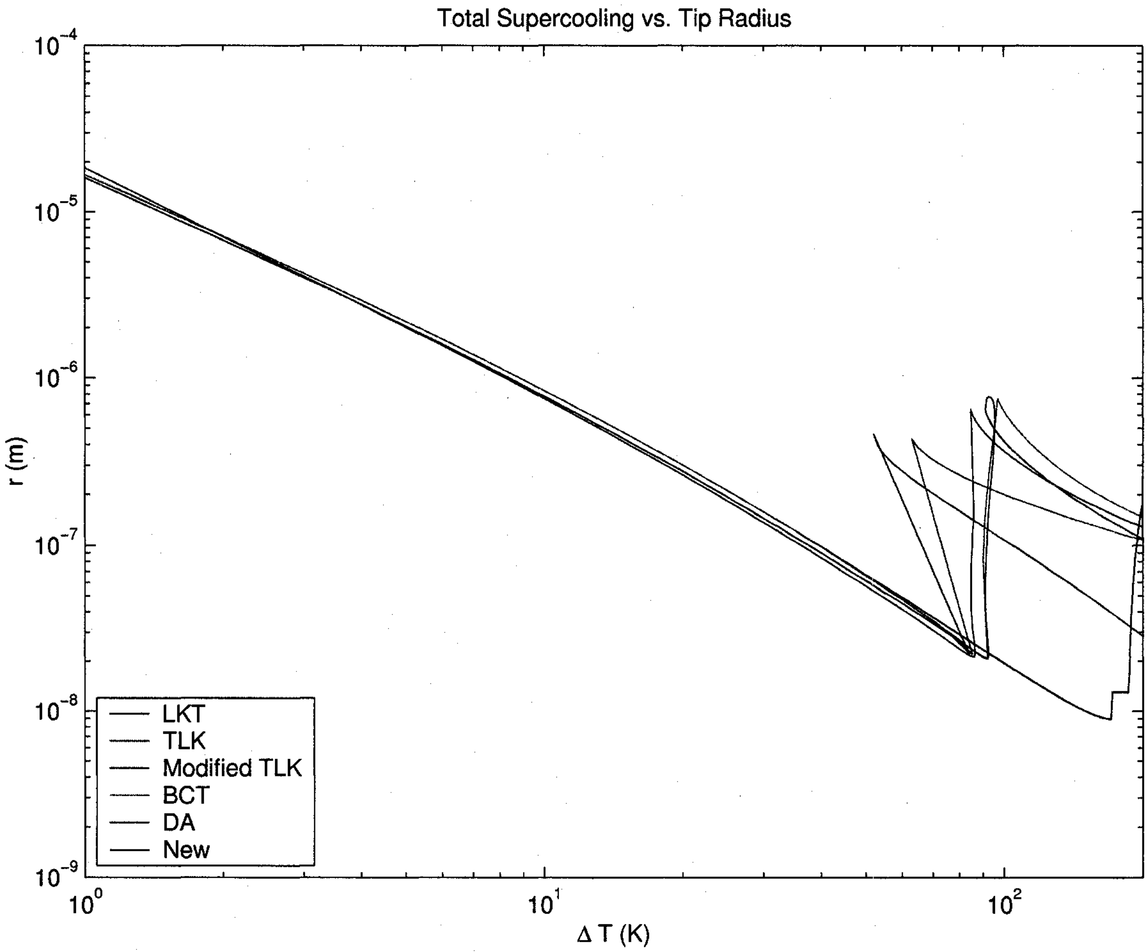

Figure 5.5: Results of free dendritic growth calculations showing the variation of tip radius with total supercooling for Ag-15 mass % Cu.

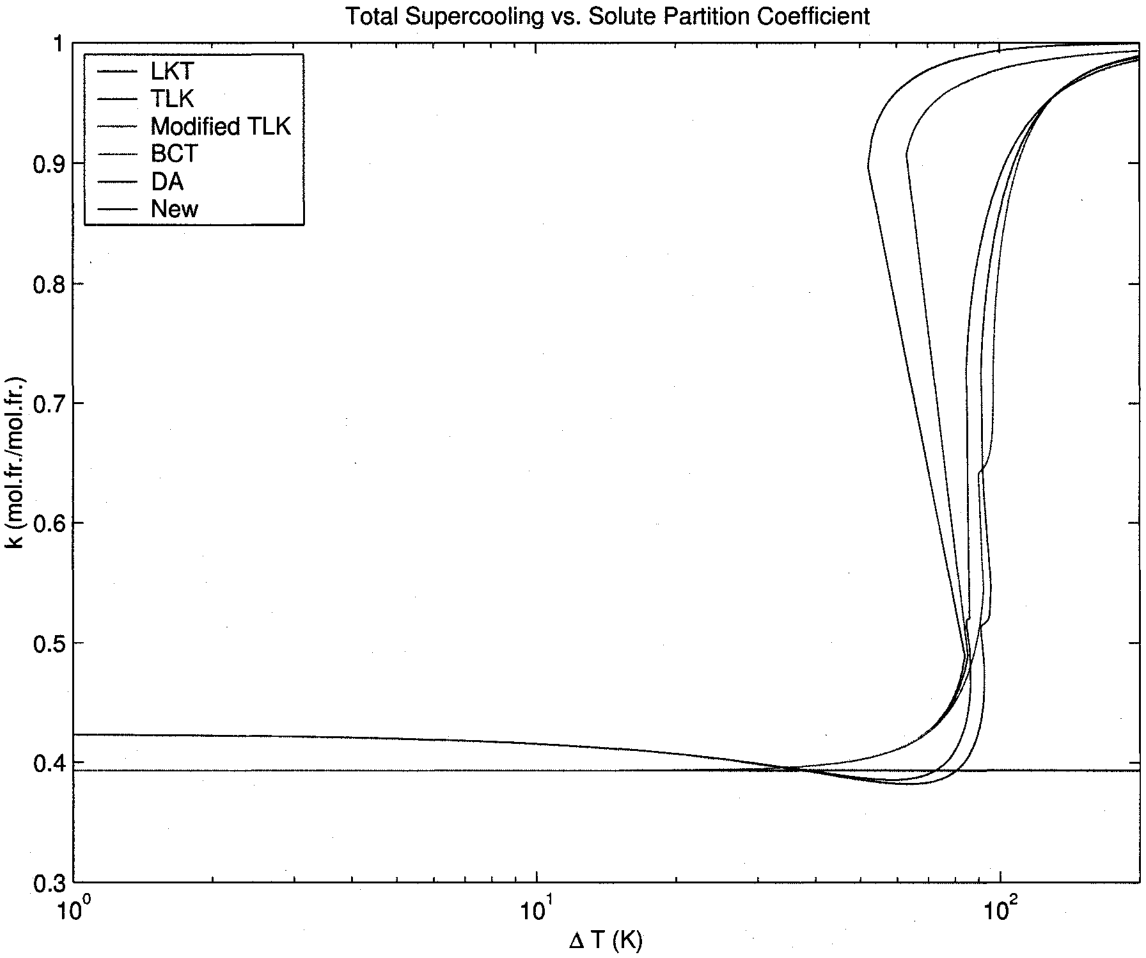

Figure 5.6: Results of free dendritic growth calculations showing the variation of partition coefficient with total supercooling for Ag-15 mass % Cu.

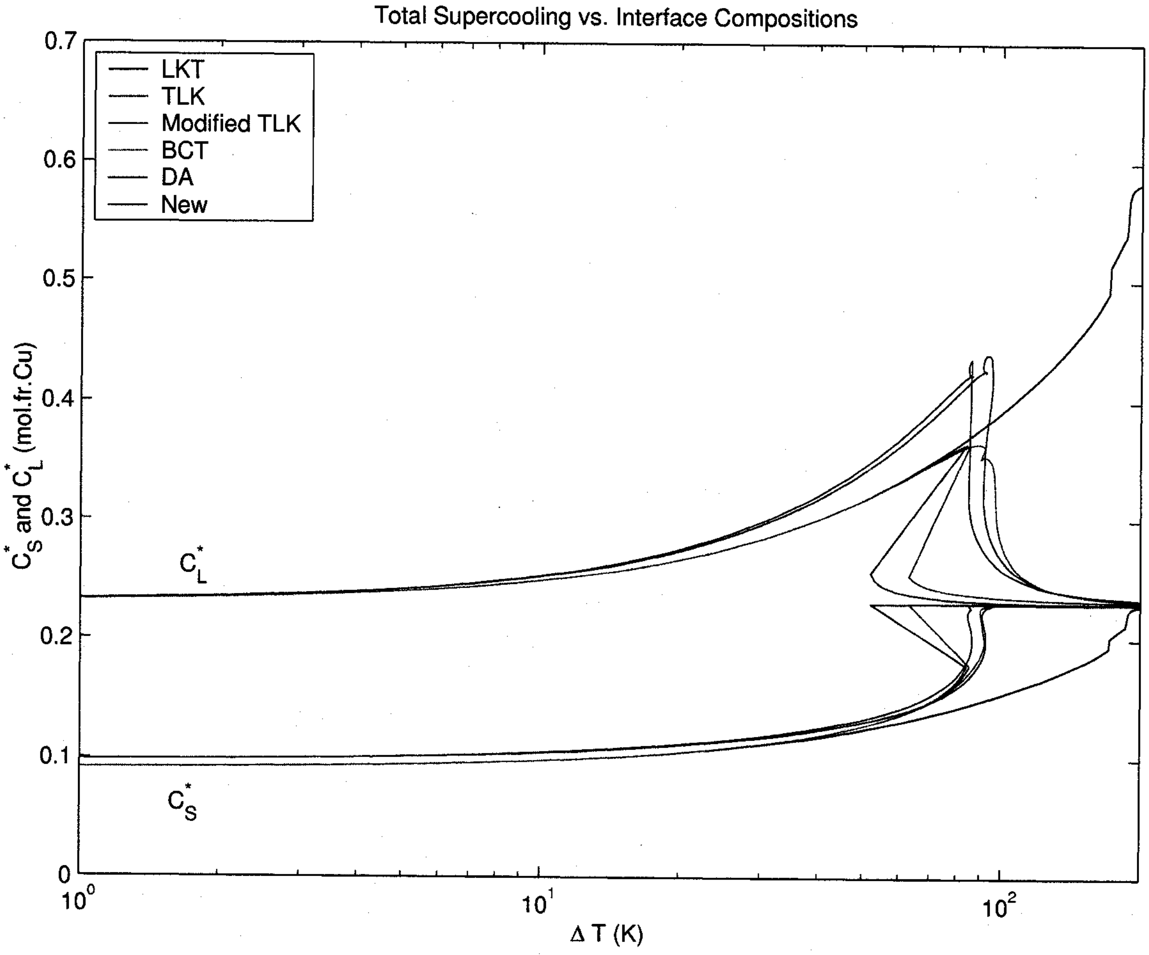

Figure 5.7: Results of free dendritic growth calculations showing the variation of interface solid and liquid concentrations with total supercooling for Ag-15 mass % Cu.

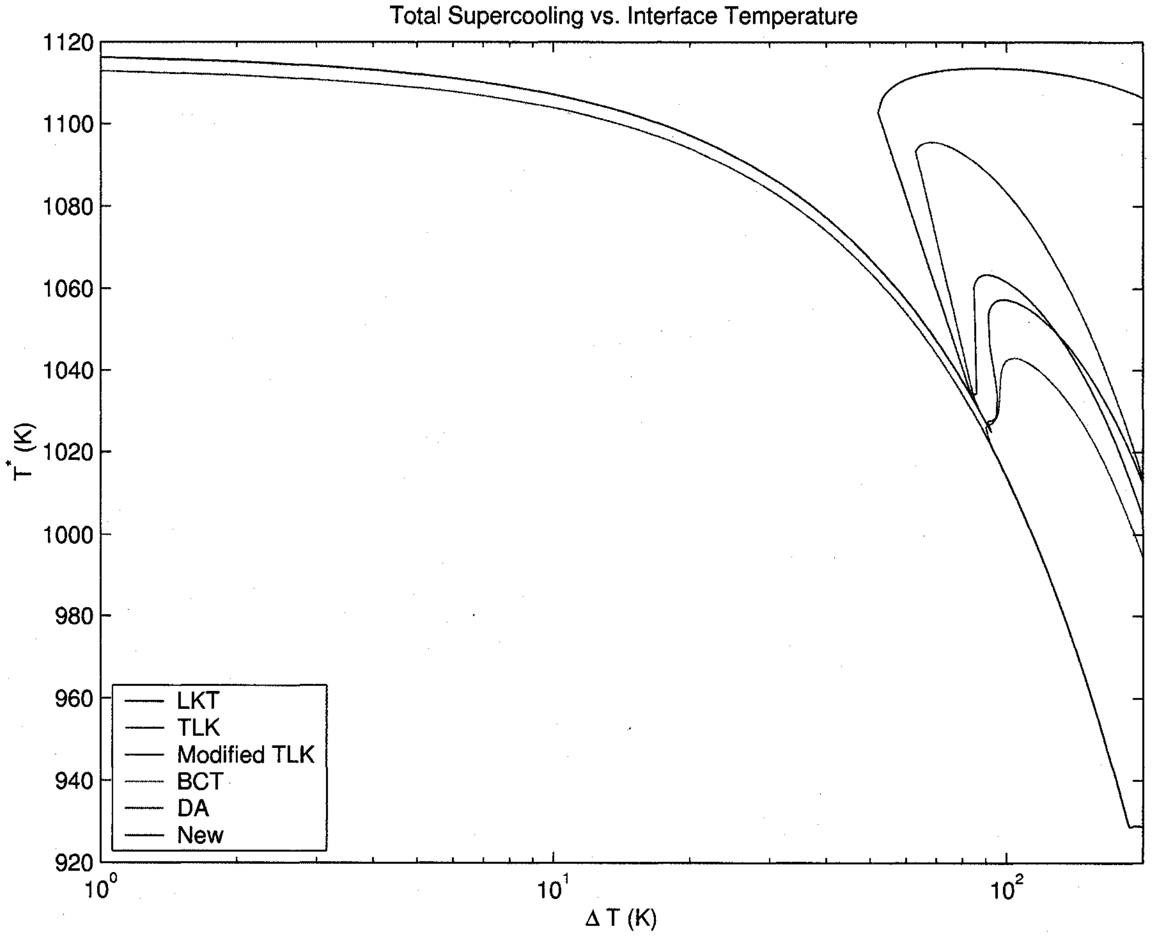

Figure 5.8: Results of free dendritic growth calculations showing the variation of interface temperature with total supercooling for Ag-15 mass % Cu.

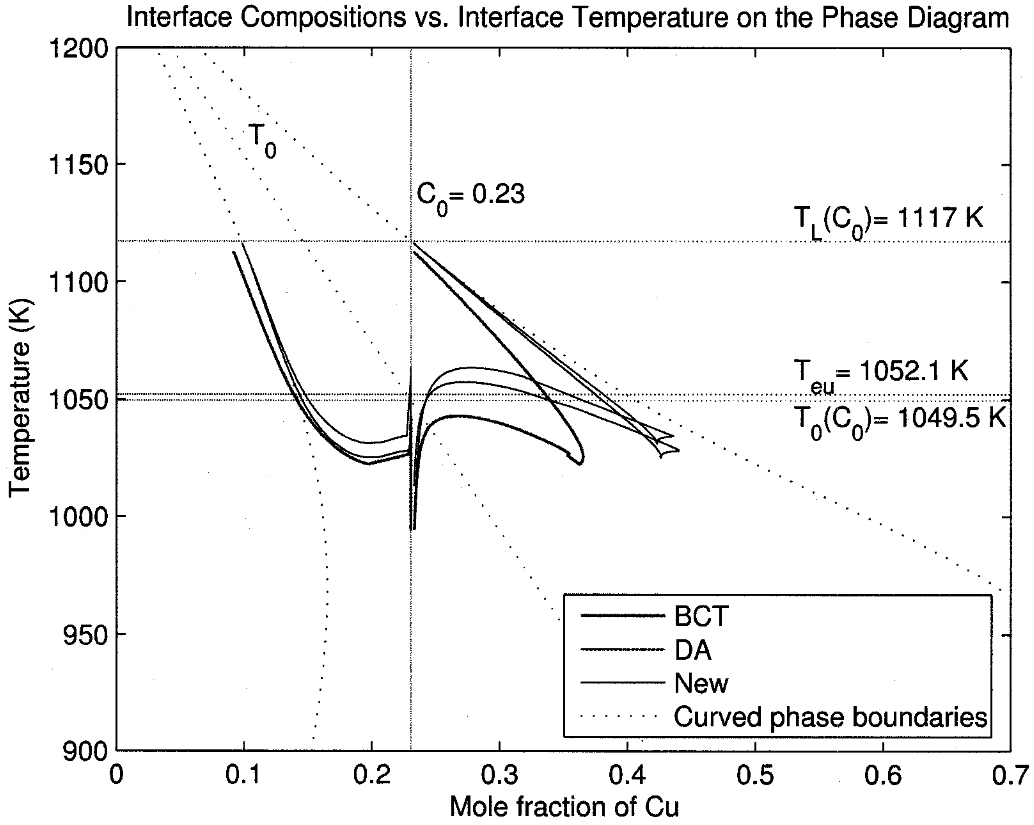

Figure 5.9: Comparison of the new model with the BCT and DA models on the Ag-Cu phase diagram.

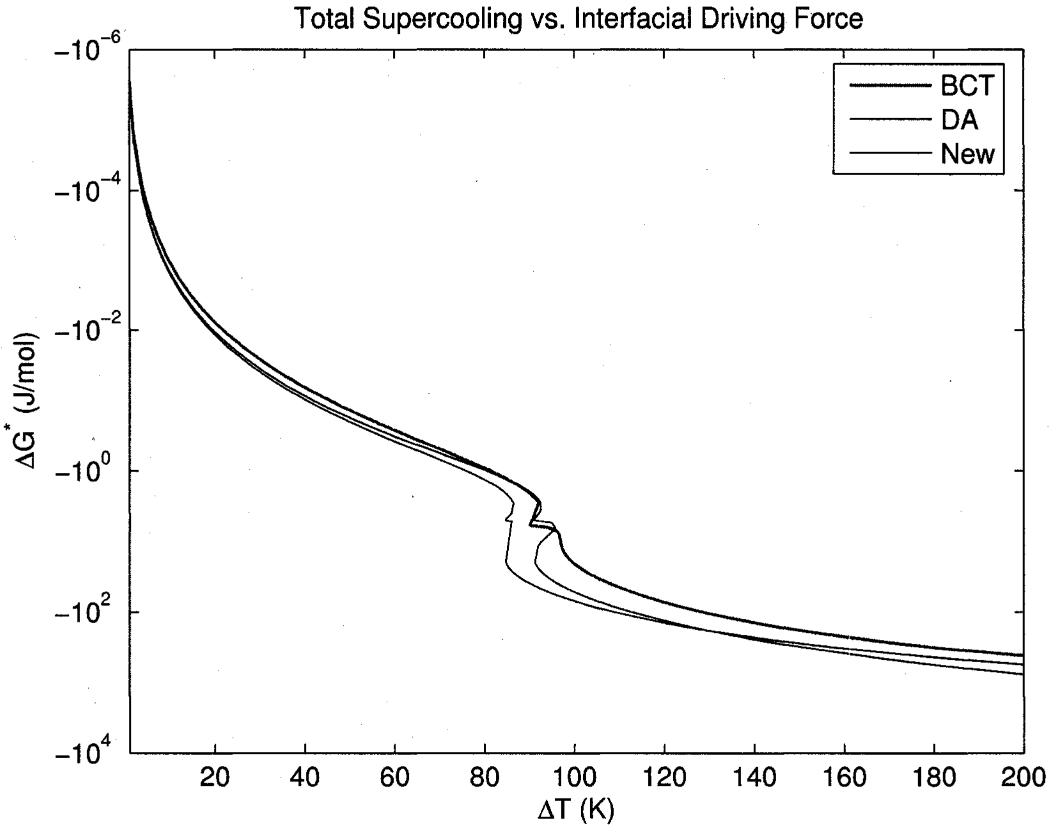

Figure 5.10: Comparison of the new model with the BCT and DA models with respect to the variation of interfacial driving force with total supercooling for Ag-15 mass % Cu.

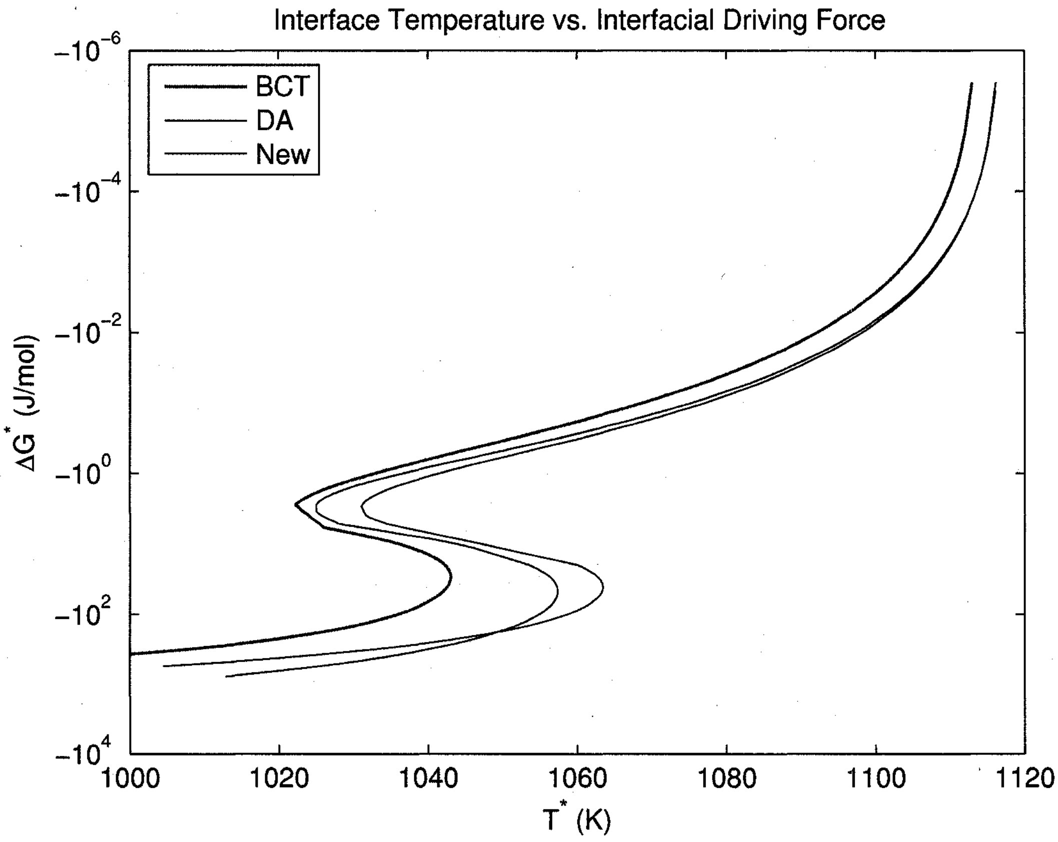

Figure 5.11: Comparison of the new model with the BCT and DA models with respect to the variation of interfacial driving force with interface temperature for Ag-15 mass % Cu.

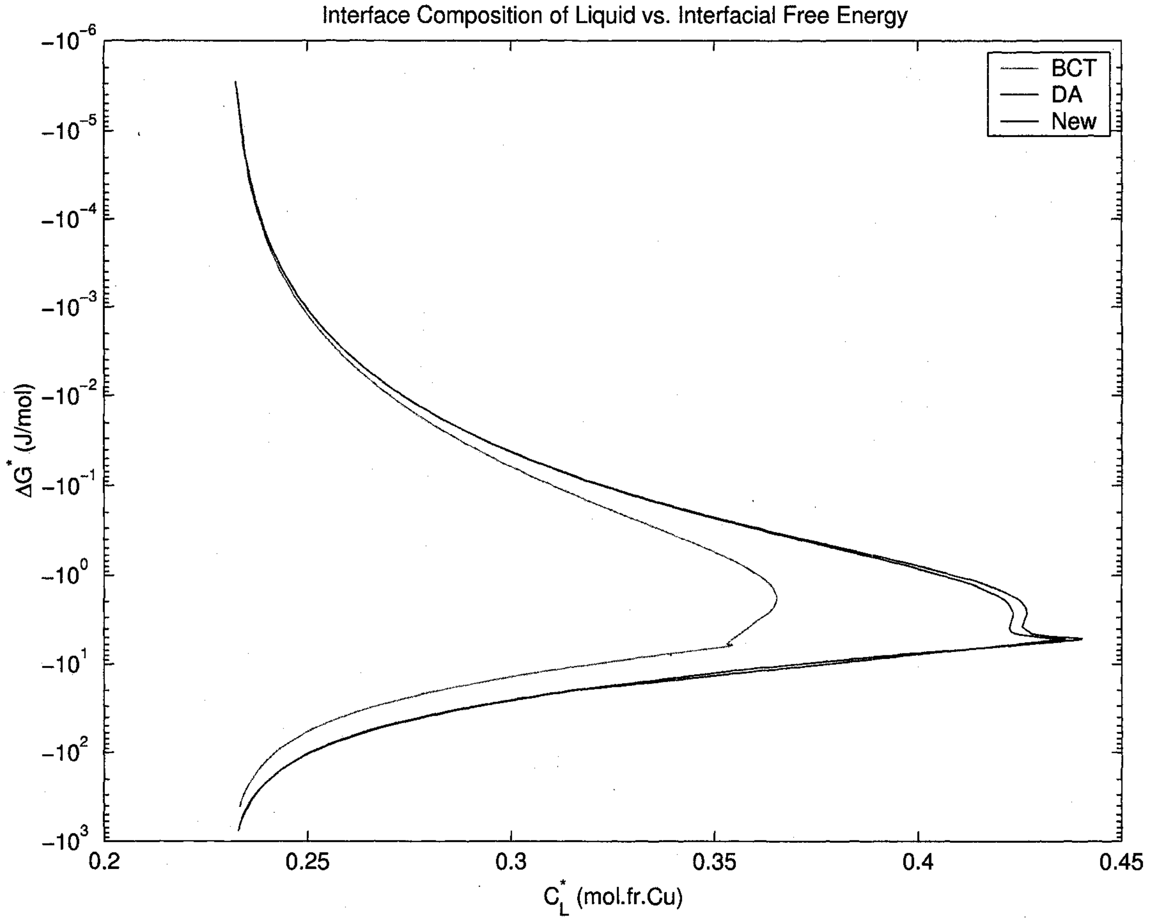

Figure 5.12: Comparison of the new model with the BCT and DA models with respect to the variation of interface concentration of the liquid with interfacial driving force for Ag-15 mass % Cu.

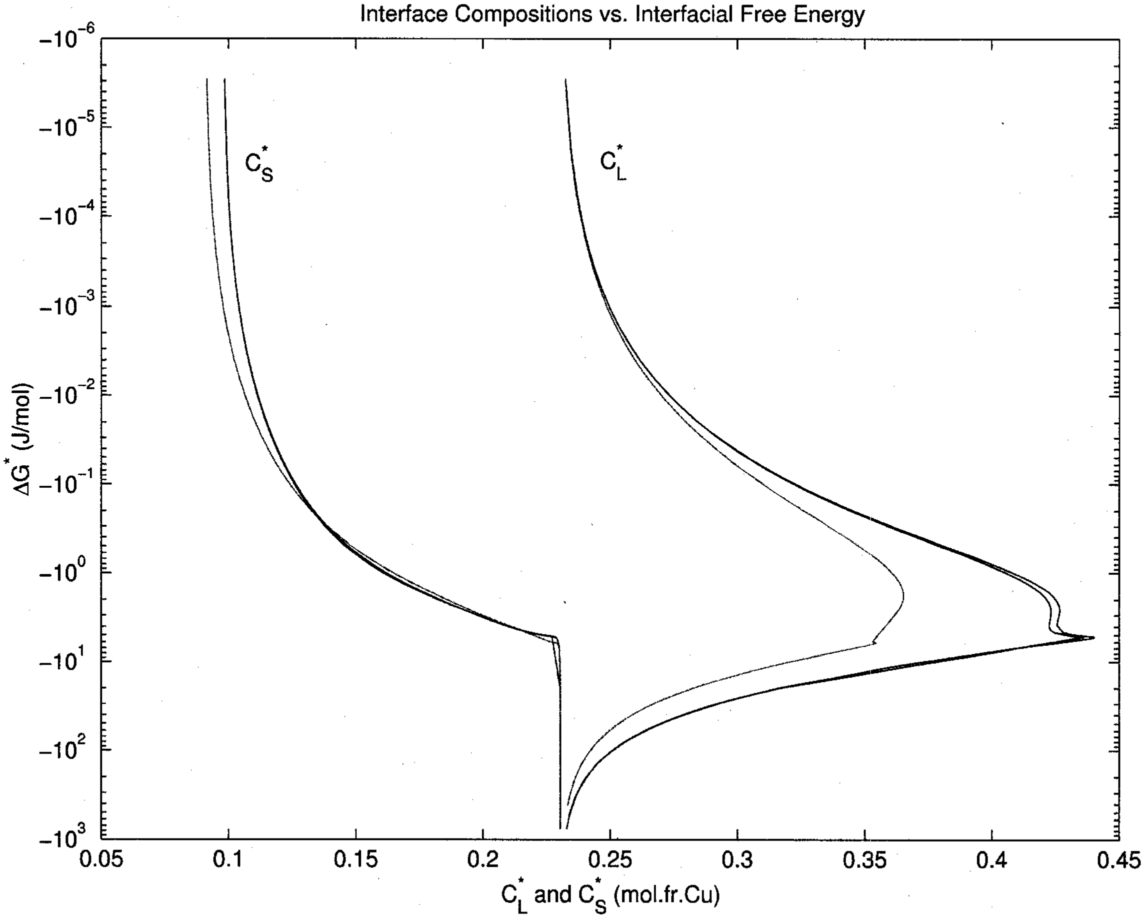

Figure 5.13: Comparison of the new model with the BCT and DA models with respect to the variation of interfacial driving force with interface concentrations of the liquid and the solid for Ag-15 mass % Cu.

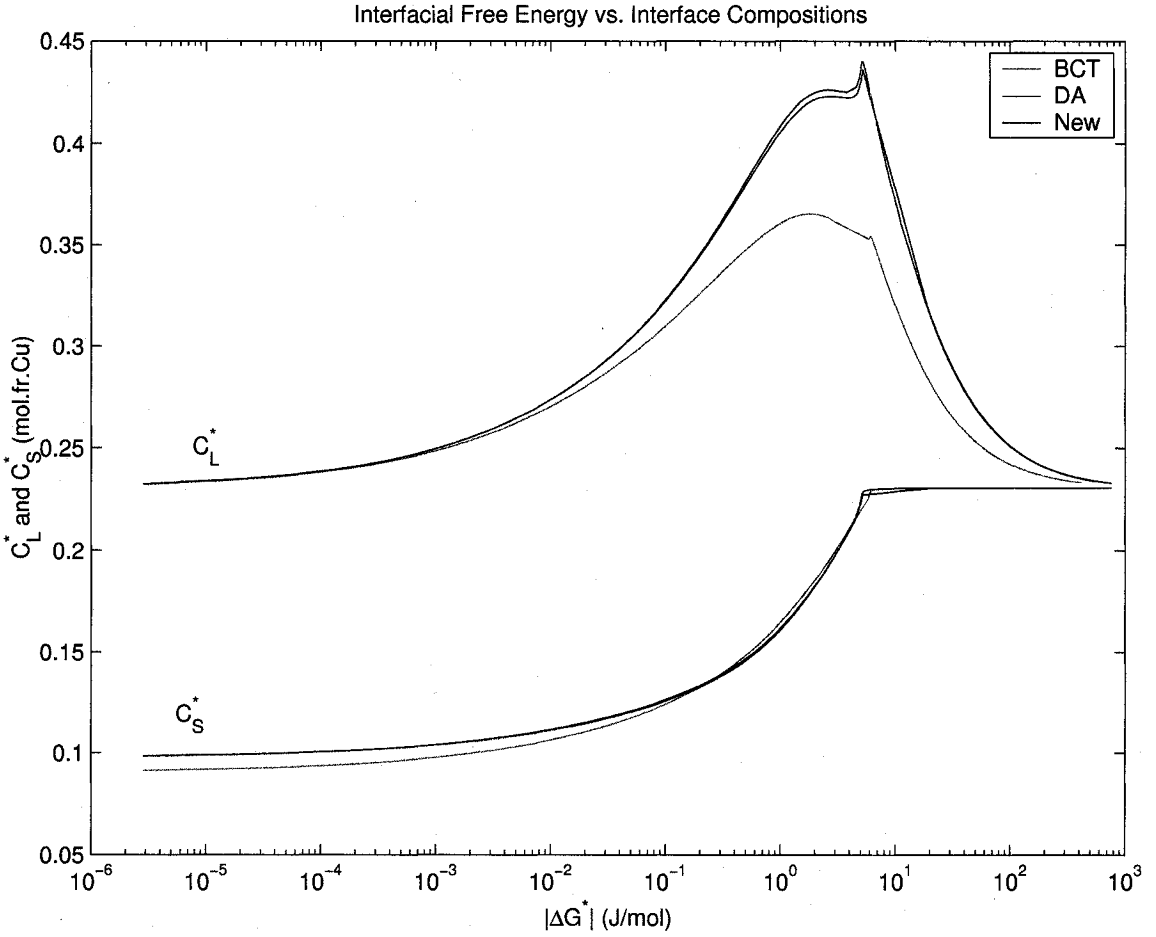

Figure 5.14: Comparison of the BCT and DA models with the new model with respect to the variation of interface concentration of the liquid and the solid with the absolute value of interfacial driving force for Ag-15 mass % Cu.

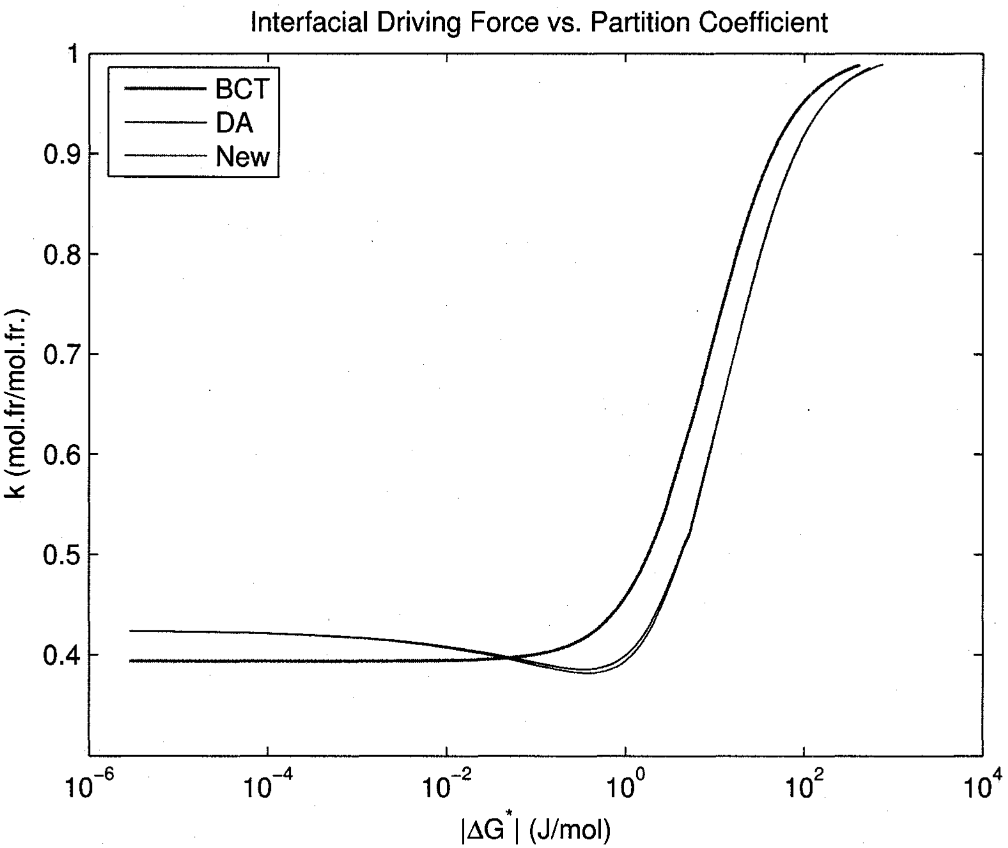

Figure 5.15: Comparison of the BCT and DA models with the new model with respect to the variation of partition coefficient with the absolute value of interfacial driving force for Ag-15 mass % Cu.

Chapter 6

A Review of Models for Solute Trapping

The rate at which atoms cross the interface during melting or freezing is usually large compared to the net rate of melting or freezing under equilibrium conditions [51]. However, a high supercooling of the solidification front during rapid solidification may cause the net rate of solid growth to exceed the interdiffusion rate of solute atoms across the interface. Under such conditions, partitioning of the solute may be restricted, promoting solute trapping, which may have impact on the mechanical properties of the material.

Jackson [52], who describes solidification in terms of kinetics, defines the solute partition coefficient for the equilibrium and the nonequilibrium cases as the microscopic k-value denoted by k_0 and the macroscopic or effective k-value denoted by k, respectively. However, Jackson assumes that in the nonequilibrium case, the chemical potentials of both the solute and the solvent decrease upon solidification, which must be balanced with the atomic mobilities in the interface in order to give the interface composition of the growing phase. Pfann [53] addresses the nonequilibrium partitioning of the solute with reference to semiconductors in his zone melting studies. Chernov [54] addresses the entrapment of the surface active solute atoms that normally diffuse toward the surface but become passive as the steps of solid layers move quickly and bury the solute, which results in an increase in chemical potential of the solute atoms in the solid as opposed to Jackson. Baker and Cahn [18] experimentally show for large growth rates that while the ratio of the solute concentration in the growing solid and that in the liquid at the interface departs from the equilibrium value given by $k_0 = C_S^{eq}/C_L^{eq}$, the solute undergoes an increase in its chemical potential upon solidification as also noted by Chernov. Baker and Cahn [17] use reversible thermodynamics to show the allowable ranges for the concentrations of the solid and the liquid at the interface temperature and to explain the thermodynamic basis for solute trapping in terms of the interfacial driving force.

The solute trapping phenomena is driven and controlled by the thermodynamic driving forces at the interface as well as the kinetics. A widely accepted solute trapping model dependent on the growth rate has been developed for dilute solutions [30, 55] and tested [56, 57, 58] by Aziz. Similar to Jackson's model, this model is formulated for one-dimensional crystal growth by using the chemical reaction rate expressions to write the mass flux of the solute atoms at the interface shown in Figure 6.1.

For steady state continuous growth with constant interface velocity, Aziz assumes that the activation energy for the diffusion in the solid is much larger than that for a solute jump across the interface given by E_d in Figure 6.2. In the stepwise growth regime shown in

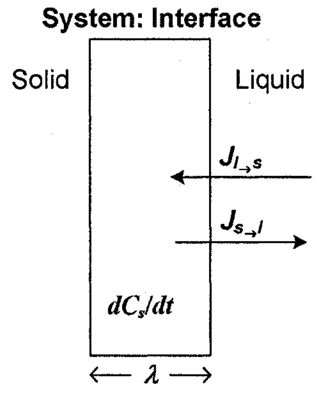

Figure 6.1: Schematic diagram of the mass balance at the solid-liquid interface.

Figure 6.2, the interface is locally planar and the movement of monolayer steps on the planar interface causes intermittent advancement of the interface that occurs at a time interval $\tau = \lambda/V$, where λ is the monolayer thickness and V is the growth rate in the direction normal to the overall interface. The diffusion of solute atoms in and out of the interface is assumed to take place in a time interval given by $0 \leq t \leq \tau$.

In the case of continuous solidification, the steady state mass balance for the system shown in Figure 6.1 at the solid-liquid interface is given by:

$$\frac{dJ}{dz} - \frac{d(VC)}{dz} = 0 \tag{6.1}$$

where J is the mass flux of the solute atoms at the interface. In a time interval t, the mass flux of the solute atoms from the solid monolayer into the liquid is given by:

$$J(t)_{s\to l} = k_f C_s(t) = \left(f_s \nu_s \lambda \gamma_s e^{\frac{-E_d}{RT^*}}\right) C_s(t) \tag{6.2}$$

where f_s is the fraction of sites in the solid monolayer where an atomic jump can occur, ν_s is the attempt frequency which is on the order of an atomic vibrational frequency, γ_s

is the activity coefficient of the solute in the solid, and $C_s(t)$ is the instantaneous solute concentration in the solid at the interface. The mass flux of the solute atoms from the liquid into the solid monolayer is given by:

$$J(t)_{l\to s} = k_b C_l(t) = \left(f_l \nu_l \lambda \gamma_l e^{\frac{-E_d - \Delta\mu_2^0}{RT^*}} \right) C_l(t) \tag{6.3}$$

where f_l is the fraction of sites in the liquid monolayer where such an atomic jump can occur, ν_l is the attempt frequency in the liquid, γ_l is the activity coefficient of the solute in the liquid, $\Delta\mu_2^0$ is the standard molar free energy change of the solute, and $C_l(t)$ is the instantaneous solute concentration in the liquid at the interface.

Integrating Equation (6.1) for the steady state growth gives:

$$(-J_{s\to l} + J_{l\to s}) = V(C_L^* - C_S^*) \tag{6.4}$$

Substituting the reaction rate expressions given in Equations (6.2) and (6.3) for $J_{s\to l}$ and $J_{l\to s}$ in Equation (6.4) at $t = \tau$ gives:

$$f_s \nu_s \lambda \gamma_s C_s e^{\frac{-E_d}{RT^*}} - f_l \nu_l \lambda \gamma_l C_L^* e^{\frac{-E_d}{RT^*}} e^{\frac{-\Delta\mu_2^0}{RT^*}} = V(C_L^* - C_S^*) \tag{6.5}$$

Introducing

$$D = \lambda^2 f_l \nu_l \gamma_s e^{\frac{-E_d}{RT^*}} \tag{6.6}$$

$$\beta = \frac{V\lambda}{D} \tag{6.7}$$

and writing the equilibrium partition coefficient for dilute solutions [59] as:

$$k_0(T^*) = \frac{\gamma_l}{\gamma_s} e^{\frac{-\Delta\mu_2^0}{RT^*}} \tag{6.8}$$

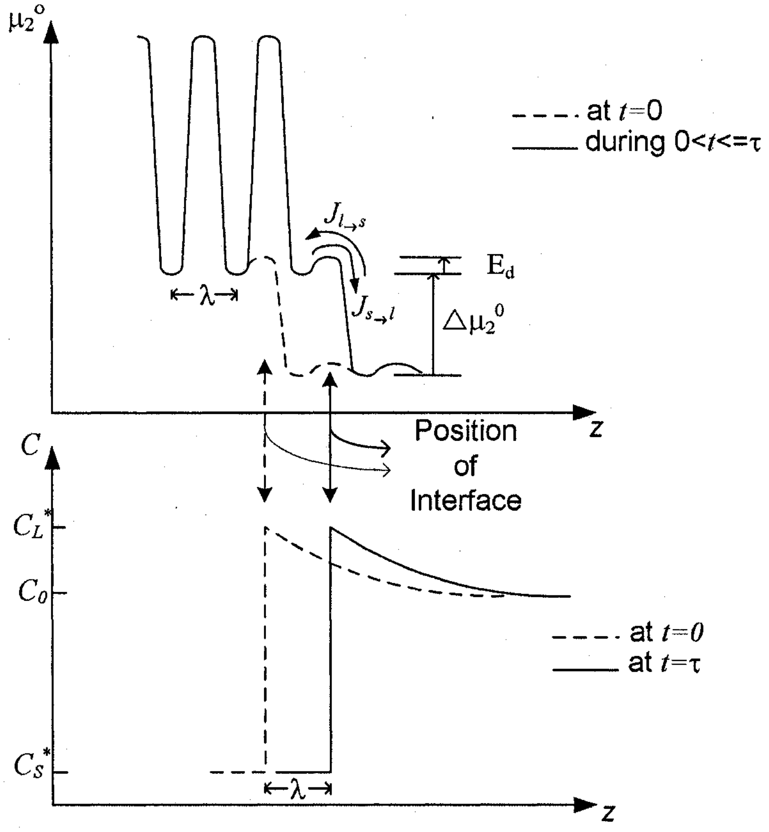

Figure 6.2: Schematic diagram of solid-liquid interface energy on the configurational coordinates for stepwise growth (Reproduced from Aziz).

and then rearranging Equation 6.5 gives:

$$-\frac{D}{\lambda}k_0(T^*)C_L^* + \frac{D}{\lambda}\frac{f_s\nu_s}{f_l\nu_l}C_s = V(C_L^* - C_S^*) \tag{6.9}$$

Rearranging Equation (6.9) gives:

$$\frac{f_s\nu_s}{f_l\nu_l}C_s - k_0(T^*)C_L^* = \frac{V\lambda}{D}(C_L^* - C_S^*) \tag{6.10}$$

Detailed balance at equilibrium requires that $\frac{f_s\nu_s}{f_l\nu_l}$ be unity, and Equation (6.10) is simplified to:

$$C_s - k_0(T^*)C_L^* = \frac{V\lambda}{D}(C_L^* - C_S^*) \tag{6.11}$$

By assuming negligible diffusion of the solute in the solid, i.e., $dC_s/dz = 0$, C_s is set equal to the solute concentration of the solid at the interface, C_S^*. Then, rearranging Equation (6.11), C_S^* is given by:

$$C_S^* = k_0(T^*)C_L^* + \frac{V\lambda}{D}C_L^* - \frac{V\lambda}{D}C_S^* \tag{6.12}$$

Regrouping the terms in Equation (6.12) gives:

$$C_S^* + \frac{V\lambda}{D}C_S^* = C_L^*\left[k_0(T^*) + \frac{V\lambda}{D}\right] \tag{6.13}$$

Finally, the nonequilibrium partition coefficient k is given by:

$$\frac{C_S^*}{C_L^*} = \frac{k_0(T^*) + \frac{V\lambda}{D}}{1 + \frac{V\lambda}{D}} = k \tag{6.14}$$

Equation (6.14) is restricted to dilute solutions due to the use of Equation (6.8) and is the same as the equation for the partition coefficient obtained by Brice [60] with the assumption of continuous growth of a rough sharp interface by using the difference of reaction rates across the interface [59, 61].

Aziz and Kaplan [59] present a version of the Aziz solute trapping model for continuous growth before simplifying it for dilute solutions as:

$$k = \frac{C_S^*}{C_L^*} = \frac{\frac{V}{V_D} + \kappa}{\frac{V}{V_D} + 1 - (1-\kappa)C_L^*} \tag{6.15}$$

where V_D is the diffusive speed given by:

$$V_D \equiv f_l \nu_l \lambda e^{\frac{-E_d}{RT^*}} \tag{6.16}$$

and κ is the partitioning parameter as a measure of the driving force for solute redistribution given by:

$$\kappa(C_L^*, C_S^*, T^*) \equiv e^{\frac{-\Delta\mu_2^0}{RT^*}} \tag{6.17}$$

Abbaschian and Kurz [62] claim that Equation (6.15) developed by Aziz can only apply to extremely sharp interfaces. This is due to the fact that the latter model assumes the total energy required for the jump of a solute atom from the liquid to the solid is given by $\Delta\mu_2^0 + E_d$ and the same for the reverse direction is given by E_d, which would be too abrupt for atomically rough or diffuse interfaces. The interfacial driving force for different types of solid-liquid interfaces as well as different molecular kinetic mechanisms for crystal growth are discussed by Cahn [63] and Cahn et al. [64].

Abbaschian and Kurz use the continuous growth mechanism to develop a solute trapping model that applies to a diffuse interface with a width δ' over which the chemical potentials of the chemical species change continuously (the chemical potential of the solvent atoms decrease to compensate for the increase in the chemical potential of the solute atoms, and the overall chemical potential of the system decreases). Applying the chemical reaction rate theory to calculate the diffusive flux of the solute atoms across the interface and defining an effective interfacial diffusion coefficient D_i gives:

$$J_2 = J_{2,l\to i} - J_{2,i\to s} = -\frac{D_i\bar{C}}{RT^*}\frac{\mu_2^s(C_S^*) - \mu_2^l(C_L^*)}{\delta'} \tag{6.18}$$

where J_2 is the flux of the solute atoms across the interface and $\bar{C}$ is the average composition within the interface. D_i describes the overall diffusion of the solute atoms in and out of the interface region without requiring detailed knowledge of the interface. As C_S^* and C_L^* represent the solute concentrations outside the interface, Equation (6.18) is rewritten as:

$$J_2 = -\frac{D_i(C_S^* + C_L^*)}{2RT^*}\frac{\Delta\mu_2^0}{\delta'} \tag{6.19}$$

For steady state solution, J_2 is given by:

$$J_2 = V\left(\frac{\rho_l}{\rho_s}C_L^* - C_S^*\right) \tag{6.20}$$

where ρ_l/ρ_s is incorporated to account for the density change upon solidification and assumed to be equal to 1. Combining Equations (6.19) and (6.20) and rearranging gives the final equation as a function of the interfacial driving force as:

$$\frac{V\delta'}{D_i} = -\frac{1+k}{2(1-k)}\frac{\Delta\mu_2^0}{RT^*} \tag{6.21}$$

The solute trapping models given by Equations (6.15) and (6.21) developed for continuous growth are free of dilute solution restrictions. The nonequilibrium partition coefficients are given as functions of the standard molar free energy change of the solute $\Delta\mu_2^0$, which is different from the interfacial driving force ΔG^*, and the growth rate V as well as some diffusive properties of the interface such as the diffusion coefficient and the interface thickness. These models can easily be incorporated in the newly developed dendritic growth model that incorporates a thermodynamic solution model to calculate the free energy curves at any interface temperature, thus removing the dilute solution limitations of the widely used Aziz equation.

Chapter 7

Conclusions

In this thesis, the current free dendritic growth models and their modifications that are designed for high supercoolings are applied to a Ag-15 mass % Cu alloy and compared numerically for the inclusion of the Aziz solute trapping model, the treatment of the thermodynamic driving force together with the Turnbull collision-limited linear kinetic model, and the employment of the curved phase boundaries. Some of the restrictions are removed from the DA model by extending this model through incorporation of a thermodynamic solution model for the interfacial driving force to replace the Baker-Cahn expression which has Henrian law restrictions. A metastable Ag-Cu phase diagram is calculated using a temperature dependent subregular solution model to calculate the interfacial driving force for dendritic growth.

The calculation results for the free dendritic growth models show that the free dendritic growth models can be classified into three groups: The first group consists of the LKT model that does not include any interface kinetics; the second group consists of the TLK and modified TLK models that include the Aziz equation for solute trapping but that do not account for the thermodynamic driving force; and the third group consists of the BCT and DA models that correctly relate the thermodynamic driving force to the interface kinetics.

The analysis of the free dendritic growth models indicate that it is important to employ their formula in a correct arrangement and consistent with the theories used, i.e., replacing the equilibrium liquidus slope with the kinetic liquidus slope in all of the involved equations does not correctly address the deviations from the local equilibrium conditions at the solid-liquid interface encountered at high supercoolings. The model referred to as the modified TLK model in this study is shown to be clearly different than the BCT model, and is proved to resemble the TLK model more as suggested by Ando [23].

It is demonstrated that the correct use of the nonlinear liquidus and solidus in the DA model (together with the Baker-Cahn equation and the Trivedi-Kurz stability criteria) improves the BCT model. Depending on the alloy selected, it may be necessary to employ curved phase boundaries as the deviations of the equilibrium concentrations from those defined by straight phase boundaries may be large at high supercoolings. The comparison of the calculation results of the DA model with those of the BCT model show that the nonequilibrium partition coefficient given by the Aziz equation and the interfacial driving force given by the Baker-Cahn equation, which are dependent on the equilibrium concentrations of the liquid and the solid, are affected by such a deviation.

It is shown that, specifically for the Ag-15 mass % Cu alloy, the free dendritic growth models which correctly relate the interfacial driving force to the linear kinetic theory (third group) yield a narrower multi-root region and, thus, can better predict the supercooling at which the solutal-to-thermal transition begins. Those models that do not account for the interfacial driving force (second group) yield a wider range of supercoolings over which the solutal-to-thermal transition can take place. Determining the interface temperature and velocity from the thermal and mass balances at the interface and accounting for only the curvature effects as in the LKT model does not give correct solutions to the free dendritic growth problem especially at high supercoolings. Integrating the interfacial driving force and the interface kinetics correctly with the solute trapping, the thermal and mass balances at the interface, and the curvature effects of the interface yields better prediction of the solidification parameters.

Comparison of the numerical results of the newly developed free dendritic growth model, which employs a thermodynamic solution model for the interfacial driving force, with those of the DA model, which employs the Baker-Cahn equation, proves that the incorporation of the thermodynamic model to calculate the interfacial driving force, ΔG^*, further improves the DA model. Numerical comparison of the computation results of the two models, however, indicates that the Baker-Cahn equation gives a fairly good approximation of ΔG^* for the Ag-15 % Cu alloy within the conditions applied to the computation.

It is explained that the free dendritic growth models designed for high supercoolings need to employ nonlinear phase boundaries with metastable extensions as the deviation from equilibrium concentrations at higher supercoolings usually becomes important as observed for the Ag-Cu system. Murrays thermodynamic solution model for the Ag-Cu system is not self-consistent as it does not satisfy the equilibrium conditions for phase diagrams. The use of the temperature dependent subregular solution model with the Ag-Cu system gives accurate phase diagram and free energy curves.

It is possible to employ the interfacial driving force, ΔG^*, calculated with a thermodynamic solution model as demonstrated in this work, together with a solute trapping model suitable for high interfacial driving forces to further eliminate the dilute solution limitation of the Aziz solute trapping equation.

Chapter 8

Future Research Direction

The incorporation of a thermodynamic solution model to calculate the interfacial driving force in the newly developed free dendritic growth model presented in this study introduces the flexibility to extend this model to completely eliminate the remaining dilute solution limitation that arise from the use of the Aziz solute trapping equation.

Solute trapping models, as discussed in Chapter 6, typically depend on the free energy difference between the solid and the liquid phases at the interface since solute trapping occurs as a result of the high interface velocity caused by the larger thermodynamic driving forces at the interface. However, these models have been simplified in order to be used with the current free dendritic models that do not incorporate a model to calculate the free energy difference at the interface.

The Aziz equation, before the implementation of the dilute solution simplifications, is given by Aziz and Kaplan [59] as:

$$k \equiv \frac{V + \frac{D}{a} e^{\frac{-\Delta\mu_2^0}{RT^*}}}{V + \frac{D}{a} - \frac{D}{a}\left(1 - e^{\frac{-\Delta\mu_2^0}{RT^*}}\right) C_L^*} \tag{8.1}$$

where the nonequilibrium partition coefficient, k, is given as a function of the standard molar free energy change of the solute $\Delta\mu_2^0$, the interface temperature T^*, and the interface concentration of the melt C_L^*, in addition to the interface velocity V. It is possible to incorporate this solute trapping model in the newly developed free dendritic growth model to replace the Aziz equation which is limited to dilute solutions.

Another solute trapping model that can be used to replace the Aziz equation is developed by Abbaschian and Kurz [62] for a diffuse interface. This model, before the simplifications done using the dilute solution assumptions, is represented by:

$$k = \frac{V - \frac{D}{2\delta}\frac{-\Delta\mu_2^0}{RT^*}}{V + \frac{D}{2\delta}\frac{-\Delta\mu_2^0}{RT^*}} \tag{8.2}$$

The incorporation of this solute trapping model in the free dendritic growth model developed in this thesis would be similar to the former one as the nonequilibrium partition coefficient is dependent on the free energy difference for the solute in the two phases.

The free energy difference for the solute represented by $\Delta\mu_2^0$ in both models is different from the interfacial driving force for free dendritic growth represented by ΔG^*. The computation scheme used for the new free dendritic growth model, presented in Figure 5.1, can be modified to couple these solute trapping models (whether used with $\Delta\mu_2^0$ or ΔG^*) with the thermodynamic solution model for free energy calculations.

Appendices

Appendix A

Formulation of the Excess Free Energy

For a binary system, the criteria for equilibrium between any two phases, for example the solid phase α and the liquid phase L, is given by [65, 44, 66] :

$$\mu_1^\alpha = \mu_1^L \tag{A.1}$$

$$\mu_2^\alpha = \mu_2^L \tag{A.2}$$

where subscripts 1 and 2 represent the components, the solvent and the solute, respectively. Writing these equations for each component using the activities gives:

$$\mu_1^{0,\alpha} + RT\ln a_1^\alpha = \mu_1^{0,L} + RT\ln a_1^L \tag{A.3}$$

$$\mu_2^{0,\alpha} + RT\ln a_2^\alpha = \mu_2^{0,L} + RT\ln a_2^L \tag{A.4}$$

Reorganizing Equations (A.3) and (A.4) gives:

$$\ln\frac{a_1^\alpha}{a_1^L} - \frac{\Delta\mu_1^{0,\alpha\to L}}{RT} = 0 \tag{A.5}$$

$$\ln\frac{a_2^\alpha}{a_2^L} - \frac{\Delta\mu_2^{0,\alpha\to L}}{RT} = 0 \tag{A.6}$$

The activity, a, is equal to the mole fraction of the component for ideal solutions. For nonideal solutions, the activity is the product of the mole fraction and the activity coefficient of the component, $a_i = x_i\gamma_i$. The activity coefficient of each component γ_i in a phase under constant pressure is dependent on the composition and the temperature of the phase. Rewriting Equations (A.5) and (A.6) with $a_i = x_i\gamma_i$ gives:

$$\ln\frac{x_1^\alpha}{x_1^L} + \ln\frac{\gamma_1^\alpha}{\gamma_1^L} - \frac{\Delta\mu_1^{0,\alpha\to L}}{RT} = 0 \tag{A.7}$$

$$\ln\frac{x_2^\alpha}{x_2^L} + \ln\frac{\gamma_2^\alpha}{\gamma_2^L} - \frac{\Delta\mu_2^{0,\alpha\to L}}{RT} = 0 \tag{A.8}$$

These equations can be solved for equilibrium phase boundaries between the two phases, i.e., the equilibrium mole fractions of the components in the two phases, at a given temperature if the logarithms of the activity coefficients can be expressed as polynomials of the mole fraction of component 2, x_2. These equations involve logarithms of mole fraction and its powers qualifying them as nonlinear algebraic equations that need to be solved numerically. Except for some special simple cases, such as a system with a very narrow region of solid solution on one side of the phase diagram, an analytic solution of this system of equations is not possible and a numerical solution must be sought [44].

The total Gibbs free energy of a system can be represented as :

$$G = \sum x_i \mu_i \tag{A.9}$$

$$= \sum x_i(\mu_i^0 + RT \ln a_i) \tag{A.10}$$

$$G = \underbrace{\sum x_i(\mu_i^0 + RT \ln x_i)}_{G^{id}} + \underbrace{\sum RT x_i \ln \gamma_i}_{G^{xs}} \tag{A.11}$$

The first part of this equation corresponds to the ideal mixing component, G^{id}, of the total Gibbs free energy, while the second part gives the excess free energy, G^{xs}, representing the non-ideality of the mixing. Expressing this equation in terms of the chemical potentials gives:

$$G = \sum x_i(\underbrace{\mu_i^0 + RT \ln x_i}_{\mu_i^{id}}) + \sum x_i \mu_i^{xs} \tag{A.12}$$

$$G = \underbrace{\sum x_i(\mu_i^0 + RT \ln x_i)}_{G^{id}} + \underbrace{\sum x_i \mu_i^{xs}}_{G^{xs}} \tag{A.13}$$

where $\mu_i^{xs} = RT \ln \gamma_i$. Consequently, the excess term for the Gibbs free energy can be written as:

$$G^{xs} = \sum x_i \mu_i^{xs} = \sum x_i RT \ln \gamma_i \tag{A.14}$$

For a binary system of components 1 and 2, G^{xs} is given by:

$$G^{xs} = x_1 \mu_1^{xs} + x_2 \mu_2^{xs} \tag{A.15}$$

where

$$\mu_1^{xs} = RT \ln \gamma_1 \quad \text{and} \quad \mu_2^{xs} = RT \ln \gamma_2 \tag{A.16}$$

Using Equations (A.15) and (A.16), the logarithmic terms of the activity coefficients in Equations (A.7) and (A.8) can be replaced with the excess chemical potentials μ_1^{xs} and μ_2^{xs}, i.e., the excess partial molar Gibbs free energies, $\overline{G}_i^{xs}$, using the following relation:

$$\ln\gamma_i = \frac{\mu_i^{xs}}{RT} \quad \text{or} \quad \ln\gamma_i = \frac{\overline{G}_i^{xs}}{RT} \tag{A.17}$$

where

$$\overline{G}_i^{xs} = \frac{G_i^{xs}}{x_i RT} = \mu_i^{xs} \tag{A.18}$$

The logarithmic function shown above can be expressed in terms of free energy interaction coefficients [36, 44] or polynomial coefficients [65, 44, 66] that represent the excess free energy.

A.1 Using Free Energy Interaction Coefficients

The use of free energy interaction coefficients is limited to dilute solutions [44]. They are obtained by the Taylor series expansion of the logarithm of the activity coefficient of the solute, $\ln\gamma_2$, at infinitely dilute solution $x_2 \longrightarrow 0$ and given by:

$$\ln\gamma_2 = \sum_{k=0}^{\infty} J_k^{(2)} x_2^k \tag{A.19}$$

where $J_k^{(2)}$ is the interaction coefficient of order k given by:

$$J_k^{(2)} = \frac{1}{k!}\left(\frac{\partial^k \ln\gamma_2}{\partial x_2^k}\right)_{x_2\longrightarrow 0} \tag{A.20}$$

By substituting the zeroth, first and second order free energy interaction coefficients designated by $\ln\gamma_2^{\infty}$, $\epsilon_2^{(2)}$, and $\rho_2^{(2)}$ [44] in Equation (A.19), $\ln\gamma_2$ is given by:

$$\ln\gamma_2 = \ln\gamma_2^{\infty} + \epsilon_2^{(2)} x_2 + \rho_2^{(2)} x_2^2 + \text{ higher order terms} \tag{A.21}$$

$\ln\gamma_2^{\infty}$, as defined by Lupis [44], is the value of $\ln\gamma_2$ at infinite solution and $\epsilon_2^{(2)}$ is a measure of how an increase in the concentration of component 2 affects the activity coefficient of component 2, γ_2. Both $J_k^{(1)}$ and $J_k^{(2)}$ are required to solve for the equilibrium phase boundaries in a binary system, which will give the partial molar ($\overline{G}_1^{xs}$, $\overline{G}_2^{xs}$) and integral molar ($\overline{G}^{xs}$) excess Gibbs free energies given by:

$$\overline{G}_1^{xs} = RT\ln\gamma_1 = RT\sum_{k=0}^{\infty} J_k^{(1)} x_2^k \tag{A.22}$$

$$\overline{G}_2^{xs} = RT\ln\gamma_1 = RT\sum_{k=0}^{\infty} J_k^{(2)} x_2^k \tag{A.23}$$

$$\overline{G}^{xs} = RT(x_1\ln\gamma_1 + x_2\ln\gamma_2) = RT\sum_{k=0}^{\infty} \Phi_k x_2^k \tag{A.24}$$

The general coefficients $J_k^{(1)}$ and $\Phi_k x_2^k$ in Equations (A.22) and (A.24) are not called the interaction coefficients since only the coefficients of the Taylor series expansion of a partial molar property of the solute with respect to its mole fraction are given this name. However, the coefficients for the solvent can be expressed in terms of the interaction coefficients using the Gibbs-Duhem relation to give:

$$\ln\gamma_1 = -\frac{1}{2}\,\epsilon_2^{(2)} x_2^2 + \text{higher order terms} \tag{A.25}$$

Finally, combining Equations (A.21) and (A.25), the integral molar excess Gibbs free energy can be expressed as a function of the interaction parameters given by:

$$\overline{G}^{xs} = RT(x_2 \ln \gamma_2^{\infty} + \frac{1}{2}\epsilon_2^{(2)} x_2^2 + \cdots) \tag{A.26}$$

A.2 Using Polynomial Coefficients

Polynomials with certain coefficients can be used to represent the excess molar free energy across the composition range in a nonideal system. The complexity of such polynomials is dependent on the system used and the solutions that form. While the use of a single coefficient may give satisfactory results for a regular solution, more complicated polynomials may be required for real solutions. The expression for the excess Gibbs free energy for regular solutions is given by:

$$G^{xs} = \Omega\, x_1 x_2 \tag{A.27}$$

where

$$\Omega = Z\left[E_{12} - \frac{1}{2}(E_{11} + E_{22})\right] \tag{A.28}$$

where Ω is a constant defined by the difference between the energy of the bonds between dissimilar atoms 1 and 2 represented by E_{12}, and the arithmetic mean of the energy of the bonds between like atoms represented by E_{11} and E_{22}, multiplied by the number of nearest neighbors to an atom in that lattice represented by Z .

For a mixture, the change in atom bonding energy of the system due to mixing, ΔE^m, is defined as the difference between the energy of the solution and the energy of the unmixed components, and is given by:

$$\Delta E^m = P_{12}\left[E_{12} - \frac{1}{2}(E_{11} + E_{22})\right] \tag{A.29}$$

ΔE^m is also defined by:

$$\Delta H^m = \Delta E^m - P\Delta V^m \tag{A.30}$$

where ΔH^m is the enthalpy of mixing. ΔE^m is equal to ΔH^m for the condition that there is no change in the volume of the system. P_{12} is the number of bonds between the atoms of component 1 and 2. It is obtained by multiplying the number of pairs of lattice sites a mole of crystal contains by the probability of a dissimilar atom pair (1-2) to fill each site, i.e., $P_{12} = (Z/2)(2\,x_1x_2)$. Substituting the expression for P_{12} in Equation (A.29), gives the enthalpy of mixing as:

$$\Delta H^m = Z\,x_1x_2\left[E_{12} - \frac{1}{2}(E_{11} + E_{22})\right] \tag{A.31}$$

In thermodynamics, the general equation for the change in Gibbs free energy due to mixing, ΔG^m, for a solution (see Table 3.2), is given by:

$$\Delta G^m = \Delta H^m - T\Delta S^m \tag{A.32}$$

For an ideal solution, there is no change in the enthalpy of the system due to mixing. Thus, the change in Gibbs free energy is only dependent on the change of the entropy of the system and is given by:

$$\Delta G^{m,id} = -T\Delta S^{m,id} \tag{A.33}$$

For a regular solution [41], the enthalpy of the system changes and the entropy of the system remains the same, $\Delta S^{m} = \Delta S^{m,id}$, which also means that there is no excess entropy formed, i.e., $S^{xs} = 0$. Hence, after mixing, the change in Gibbs free energy for a regular solution is different from that for an ideal system due to changes in the enthalpy by an amount of G^{xs}. Therefore, for a regular solution, the excess free energy is equal to the enthalpy of mixing, which is equal to the excess enthalpy and is given by:

$$G^{xs} = \Delta H^{m} = H^{xs} \tag{A.34}$$

Substituting ΔH^{m} given in Equation (A.31) in Equation (A.34) gives G^{xs} as:

$$G^{xs} = Z\, x_1 x_2 \left[E_{12} - \frac{1}{2}(E_{11} + E_{22}) \right] \tag{A.35}$$

Rewriting Equation (A.35) using $\Omega = Z\left[E_{12} - \frac{1}{2}(E_{11} + E_{22})\right]$ gives:

$$G^{xs} = \Omega\, x_1 x_2 \tag{A.36}$$

For systems with real solutions, if the regular solution model with Ω being the only constant coefficient is not capable of representing the properties, a polynomial representation for Ω can be implemented to give:

$$\Omega = a + b x_2 + c x_2^2 + \cdots \tag{A.37}$$

where a, b and c are constant parameters [44]. Employing the first and second parts of the polynomial in Ω given by

$$\Omega = a + b\, x_2 \tag{A.38}$$

is called the subregular solution model [42, 65, 44, 66]. Depending on how well the alloy system data is represented, the third coefficient with the second order term, $c\,x_2^2$, and higher order terms can be included in the expression for Ω. Such a subregular solution model is not dependent on temperature. This model may be made more sensitive with the addition of an excess entropy term by making Ω dependent on temperature. The coefficients of the subregular solution model, a and b, can be written as a function of temperature T and another constant parameter τ as:

$$a = A\left(1 - \frac{T}{\tau}\right) \quad \text{and} \quad b = B\left(1 - \frac{T}{\tau}\right) \tag{A.39}$$

where A and B are the new constant parameters. After the introduction of the temperature dependency, Ω and G^{xs} are given by:

$$\Omega = (A + Bx_2)\left(1 - \frac{T}{\tau}\right) \tag{A.40}$$

and

$$G^{xs} = (A + Bx_2)\,x_1 x_2\left(1 - \frac{T}{\tau}\right) \tag{A.41}$$

In Equation (A.41), G^{xs} is no longer equivalent to the change in the enthalpy of mixing, ΔH^m, i.e., $G^{xs} \neq H^{xs}$, but also involves the excess entropy term S^{xs} and is given by:

$$G^{xs} = H^{xs} - TS^{xs} \tag{A.42}$$

By definition, the excess entropy S^{xs} is given by:

$$S^{xs} = -\frac{\partial G^{xs}}{\partial T} \tag{A.43}$$

By combining Equation (A.41) with Equation (A.43), S^{xs} is given by:

$$S^{xs} = \frac{(A + Bx_2)x_1x_2}{\tau} \tag{A.44}$$

Lupis and Elliott [44, 43] name the temperature dependent subregular solution model as the quasi-regular solution model due to the involvement of the excess entropy and gives the physical interpretation of the parameter τ as the ratio of the excess enthalpy to the excess entropy of the system given by $\tau = H^{xs}/S^{xs}$. It is possible to express the subregular and the temperature dependent subregular solution models in terms of the free energy interaction parameters mentioned in Section A.1 as explained clearly by Lupis [44].

The thermodynamic functions for the ideal, regular, subregular and temperature dependent subregular solution models are summarized in Table 3.2.

Appendix B

Phase Boundary Equations

The first thing to check before implementing any solution model on the phase boundary equations is whether the solution model that defines the excess free energy or the excess chemical potential satisfies the condition for equilibrium.

B.1 Verification of the Temperature Dependent Subregular Solution Model

It is known from the phase diagram that for a binary system the following relations should hold in any of the phases:

$$\mu_1^{xs} = \overline{G}_1^{xs} = G^{xs} + x_2 \frac{dG^{xs}}{dx_1} \qquad \text{for component 1} \tag{B.1}$$

$$\mu_2^{xs} = \overline{G}_2^{xs} = G^{xs} + x_1 \frac{dG^{xs}}{dx_2} \qquad \text{for component 2} \tag{B.2}$$

Multiplying the chemical potentials (molar free energies) for each component by their respective molar fractions yields the total excess free energy for the system given by:

$$G^{xs} = x_1\mu_1^{xs} + x_2\mu_2^{xs} \tag{B.3}$$

For the temperature dependent subregular solution model this necessary condition is satisfied. This can be shown by applying the subregular solution model given in Equation (A.41) as

$$G^{xs} = (A + Bx_2)x_1x_2\left(1 - \frac{T}{\tau}\right)$$

on a binary system to find the chemical potentials of each component using Equations (B.1) and (B.2). This gives:

$$\mu_1^{xs} = [A + B(2x_2 - 1)]\left(1 - \frac{T}{\tau}\right)x_2^2 \tag{B.4}$$

for component 1, and

$$\mu_2^{xs} = (A + 2Bx_2)\left(1 - \frac{T}{\tau}\right)x_1^2 \tag{B.5}$$

for component 2. Substituting the expressions for μ_1^{xs} and μ_2^{xs} into Equation (B.3) to get the excess free energy of the system gives:

$$\begin{aligned} G^{xs} &= x_1\left[A + B(2x_2 - 1)\right]\left(1 - \frac{T}{\tau}\right)x_2^2 + x_2(A + 2Bx_2)\left(1 - \frac{T}{\tau}\right)x_1^2 \qquad \text{(B.6)} \\ &= \left[x_1(Ax_2^2 - Bx_2^2 + 2Bx_2^3) + x_2(Ax_1^2 + 2Bx_1^2x_2)\right]\left(1 - \frac{T}{\tau}\right) \\ &= x_1x_2(Ax_1x_2^2 - Bx_1x_2^2 + 2Bx_1x_2^3 + Ax_1^2x_2 + 2Bx_1^2x_2^2)\left(1 - \frac{T}{\tau}\right) \\ &= x_1x_2(Ax_2 - Bx_2 + 2Bx_2^2 + Ax_1 + 2Bx_1x_2)\left(1 - \frac{T}{\tau}\right) \end{aligned}$$

Using the molar fraction relations $x_1 = 1 - x_2$ and $x_2 = 1 - x_1$ in Equation (B.6) gives:

$$G^{xs} = x_1x_2(A - Ax_1 - Bx_2 + 2Bx_2^2 + Ax_1 + 2Bx_2 - 2Bx_2^2)\left(1 - \frac{T}{\tau}\right)$$

and, further simplifying gives:

$$G^{xs} = x_1x_2(A + Bx_2)\left(1 - \frac{T}{\tau}\right) \tag{B.7}$$

Equation (B.7) is the same as Equation (A.41), which shows that the temperature dependent subregular solution model with the coefficients A, B and τ satisfies the necessary equilibrium condition.

B.2 Derivation of the Phase Boundary Equations Using the Temperature Dependent Subregular Solution Model

Recalling the phase boundary equations given in Equations (A.7) and (A.8) as:

$$\ln\frac{x_1^\alpha}{x_1^L} + \ln\frac{\gamma_1^\alpha}{\gamma_1^L} - \frac{\Delta\mu_1^{0,\alpha\to L}}{RT} = 0$$

$$\ln\frac{x_2^\alpha}{x_2^L} + \ln\frac{\gamma_2^\alpha}{\gamma_2^L} - \frac{\Delta\mu_2^{0,\alpha\to L}}{RT} = 0$$

and remembering $\ln\gamma_i^\phi = \mu_i^{xs,\phi}/RT$, the phase boundary equations can be rearranged for each component in the two adjacent phases to give:

$$\ln\frac{\gamma_i^\alpha}{\gamma_i^L} = \frac{1}{RT}(\mu_i^{xs,\alpha} - \mu_i^{xs,L}) \tag{B.8}$$

Rewriting the chemical potential expressions obtained in Equations (B.4) and (B.5) for the solid, α, and the liquid, L, phases gives:

$$\mu_1^{xs,\alpha} = [A^\alpha + B^\alpha(2x_2 - 1)]\left(1 - \frac{T}{\tau^\alpha}\right)x_2^2 \tag{B.9}$$

$$\mu_1^{xs,L} = [A^L + B^L(2x_2 - 1)]\left(1 - \frac{T}{\tau^L}\right)x_2^2 \tag{B.10}$$

for component 1 and

$$\mu_2^{xs,\alpha} = (A^\alpha + 2B^\alpha x_2)\left(1 - \frac{T}{\tau^\alpha}\right)x_1^2 \tag{B.11}$$

$$\mu_2^{xs,L} = (A^L + 2B^L x_2)\left(1 - \frac{T}{\tau^L}\right)x_1^2 \tag{B.12}$$

for component 2. Substituting the chemical potentials obtained in Equations (B.9) to (B.12) in Equation (B.8) for each component gives:

$$\ln\frac{\gamma_1^\alpha}{\gamma_1^L} = \frac{1}{RT}\left\{[A^\alpha + B^\alpha(2x_2 - 1)]\left(1 - \frac{T}{\tau^\alpha}\right)x_2^2 - [A^L + B^L(2x_2 - 1)]\left(1 - \frac{T}{\tau^L}\right)x_2^2\right\} \tag{B.13}$$

$$\ln\frac{\gamma_2^\alpha}{\gamma_2^L} = \frac{1}{RT}\left\{(A^\alpha + 2B^\alpha x_2)\left(1 - \frac{T}{\tau^\alpha}\right)x_1^2 - (A^L + 2B^L x_2)\left(1 - \frac{T}{\tau^L}\right)x_1^2\right\} \tag{B.14}$$

Finally, inserting Equations (B.13) and (B.14) into the equilibrium phase diagram equations, Equations (A.7) and (A.8), the final expressions for a section of the phase diagram can be obtained as a function of the three variables and the six subregular solution model constant parameters. The three variables are the temperature, T , and the two mole fractions of the adjacent phases, x_2^α and x_2^L (or x_1^α and x_1^L, since the mole fractions of the two components are related by $x_1^\alpha = 1 - x_2^\alpha$ and $x_1^L = 1 - x_2^L$). All the equations and the data used to calculate the phase diagram should be adjusted depending on the component used.

The final expressions are given by:

$$\begin{aligned}\ln\frac{x_1^\alpha}{x_1^L} + \frac{1}{RT}\Big\{&[A^\alpha + B^\alpha(2x_2^\alpha - 1)]\left(1 - \frac{T}{\tau^\alpha}\right)x_2^{\alpha 2} \\ &- \left[A^L + B^L(2x_2^L - 1)\right]\left(1 - \frac{T}{\tau^L}\right)x_2^{L^2}\Big\} - \frac{\Delta\mu_1^{0,\alpha\to L}}{RT} = 0\end{aligned} \tag{B.15}$$

$$\begin{aligned}\ln\frac{x_2^\alpha}{x_2^L} + \frac{1}{RT}\Big\{&(A^\alpha + 2B^\alpha x_2^\alpha)\left(1 - \frac{T}{\tau^\alpha}\right)x_1^{\alpha 2} \\ &- \left(A^L + 2B^L x_2^L\right)\left(1 - \frac{T}{\tau^L}\right)x_1^{L^2}\Big\} - \frac{\Delta\mu_2^{0,\alpha\to L}}{RT} = 0\end{aligned} \tag{B.16}$$

These two equations need to be solved together on different sections of the phase diagram for the boundaries of the adjacent phases, in the present case for the solidus and the liquidus, depending on the available experimental data of temperature and the mole fractions. For a eutectic system, there are three couples of boundaries to be determined: Solidus and liquidus on the Component 1-rich side, liquidus and solidus on the Component 2-rich side, and the solvus on each side.

If the experimental data and the equations are used in terms of the first component, x_1, the phase boudnary equations are given by:

$$\begin{aligned}\ln\frac{x_1^\alpha}{x_1^L} + \frac{1}{RT}\Big\{&[A^\alpha + B^\alpha(1 - 2x_1^\alpha)]\left(1 - \frac{T}{\tau^\alpha}\right)(1 - x_1^\alpha)^2 \\ &- [A^L + B^L(1 - 2x_1^L)]\left(1 - \frac{T}{\tau^L}\right)(1 - x_1^L)^2\Big\} - \frac{\Delta\mu_1^{0,\alpha\to L}}{RT} = 0\end{aligned} \tag{B.17}$$

$$\begin{aligned}\ln\frac{1 - x_1^\alpha}{1 - x_1^L} + \frac{1}{RT}\Big\{&[A^\alpha + 2B^\alpha(1 - x_1^\alpha)]\left(1 - \frac{T}{\tau^\alpha}\right)x_1^{\alpha 2} \\ &- \left[A^L + 2B^L(1 - x_1^L)\right]\left(1 - \frac{T}{\tau^L}\right)x_1^{L^2}\Big\} - \frac{\Delta\mu_2^{0,\alpha\to L}}{RT} = 0\end{aligned} \tag{B.18}$$

If the experimental data is used in terms of the mole fractions of the second component, x_2, then the equations are given by:

$$\begin{aligned}\ln\frac{1-x_2^\alpha}{1-x_2^L} + \frac{1}{RT}\Big\{&\left[A^\alpha + B^\alpha(2x_2^\alpha - 1)\right]\left(1-\frac{T}{\tau^\alpha}\right)x_2^{\alpha 2}\\ &- \left[A^L + B^L(2x_2^L - 1)\right]\left(1-\frac{T}{\tau^L}\right)x_2^{L^2}\Big\} - \frac{\Delta\mu_1^{0,\alpha\rightarrow L}}{RT} = 0\end{aligned} \tag{B.19}$$

$$\begin{aligned}\ln\frac{x_2^\alpha}{x_2^L} + \frac{1}{RT}\Big\{&\left(A^\alpha + 2B^\alpha x_2^\alpha\right)\left(1-\frac{T}{\tau^\alpha}\right)(1-x_2^\alpha)^2\\ &- \left(A^L + 2B^L x_2^L\right)\left(1-\frac{T}{\tau^L}\right)\left(1-x_2^L\right)^2\Big\} - \frac{\Delta\mu_2^{0,\alpha\rightarrow L}}{RT} = 0\end{aligned} \tag{B.20}$$

Appendix C

Ivantsov Equation Approximation

(Reproduced from References [6, 67])

Ivantsov function is given by:

$$I_v(P) = -Pe^P E_i(P) \tag{C.1}$$

where the exponential integral function $E_i(P)$ is calculated from mathematical approximations.

For $0 \leq P \leq 1$, $E_i(P)$ is given by:

$$E_i(P) = a_0 + a_1 P + a_2 P^2 + a_3 P^3 + a_4 P^4 + a_5 P^5 - \ln P \tag{C.2}$$

where

a0 = -0.57721566
a1 = 0.99999193
a2 = -0.24991055
a3 = 0.05519968
a4 = -0.00976004
a5 = 0.00107857

and for $1 \leq P \leq \infty$,

$$E_i(P) = \frac{P^4 + a_6 P^3 + a_7 P^2 + a_8 P + a_9}{P^4 + b_1 P^3 + b_2 P^2 + b_3 P + b_4} \tag{C.3}$$

where

a6 = 8.5733287401   b1 = 9.5733223454
a7 = 18.0590169730   b2 = 25.6329561486
a8 = 8.6347608925   b3 = 21.0996530827
a9 = 0.2677737343   b4 = 3.9584969228

Appendix D

Nomenclature

1	Major component or solvent, see equation (2.48), page 36
2	Minor component or solute, see equation (2.48), page 36
α	Thermal diffusion constant of the liquid, see equation (2.1), page 23
β_0	Solute trapping kinetic coefficient, a_0/D [s/m], see equation (2.43), page 34
ΔG^*	Interfacial driving force or change if free energy across the interface [J/mol], see equation (2.51), page 37
ΔH_f	Molar enthalpy of fusion, see equation (2.9), page 24
ΔH_{f1}	Latent heat of fusion per mole of pure component (solvent) represented by 1, see equation (2.51), page 37
ΔS_f	Entropy of melting per unit volume [J/K$\cdot$m^3], see equation (2.26), page 28
ΔT	Total bath supercooling [K], see equation (2.0), page 22

ΔT_c	Solutal supercooling [K], see equation (2.18), page 27
ΔT_r	Curvature supercooling [K], see equation (2.28), page 29
ΔT_t	Thermal supercooling [K], see equation (2.15), page 27
$\Delta\mu_2^0$	Standard molar free energy change of the solute [J/mole], see equation (6.3), page 130
ϵ	Amount of computation error, see equation (4.32), page 84
η	Ratio of thermal to solutal diffusivity given by α/D, see equation (2.89), page 48
Γ	Gibbs-Thomson coefficient [K·m], see equation (2.26), page 28
γ	Solid-liquid interface energy [J/m^2], see equation (2.26), page 28
γ_l	Activity coefficient of the solute in the liquid, see equation (6.3), page 130
γ_s	Activity coefficient of the solute in the solid, see equation (6.2), page 129
κ	Partitioning parameter as a measure of the driving force for solute redistribution, see equation (6.17), page 133
λ	Shortest wavelength of perturbation [m], see equation (2.30), page 30
μ	Linear kinetic coefficient [m/K·s], see equation (2.63), page 40
μ_1^L	Chemical potential of the solvent in the liquid phase [J/mole], see equation (2.48), page 36

μ_1^S	Chemical potential of the solvent in the solid phase [J/mole], see equation (2.48), page 36
μ_2^L	Chemical potential of the solute in the liquid phase [J/mole], see equation (2.48), page 36
μ_2^S	Chemical potential of the solute in the solid phase [J/mole], see equation (2.48), page 36
ν_l	Attempt frequency in the liquid, see equation (6.3), page 130
ν_s	Attempt frequency in the solid on the order of an atomic vibrational frequency, see equation (6.2), page 129
ω	Wave number of the perturbation on the interface, $2\pi/\lambda$, see equation (2.36), page 32
Ω_c	Dimensionless supersaturation, see equation (2.9), page 24
Ω_t	Dimensionless thermal supercooling, see equation (2.8), page 24
$\overline{K}_l$	Dimensionless thermal conductivity of the liquid, see equation (2.36), page 32
$\overline{K}_s$	Dimensionless thermal conductivity of the solid, see equation (2.36), page 32
ϕ	Phase (solid or liquid), see equation (3.1), page 59
ρ, θ, ζ	Cylindrical coordinates for paraboloid of revolution, see equation (2.1), page 23

Θ	Unit supercooling equal to $\Delta H_f/c_p$, see equation (2.35), page 31
ξ_c	Solutal stability parameter for the liquid, see equation (2.36), page 32
ξ_l	Thermal stability parameter for the liquid, see equation (2.36), page 32
ξ_s	Thermal stability parameter for the solid, see equation (2.36), page 32
ξ_t	Thermal stability parameter for the liquid, see equation (2.39), page 33
A	Dimensionless parameter equal to C_L^*/C_0, see equation (2.34), page 31
a_0	Length scale of the order of interatomic distance [m], see equation (2.43), page 34
A_k	Dimensionless parameter A ($= C_L^*/C_0$) redefined with k instead of k_0, see equation (2.45), page 35
C_0	Alloy composition [mole fr.], see equation (2.0), page 22
C_L	Equilibrium solute concentration of liquid [mole fr.], see equation (2.18), page 27
C_l	Concentration profile in the liquid, see equation (2.2), page 23
$C_l(t)$	Instantaneous solute concentration in the liquid at the interface, see equation (6.3), page 130
C_L^*	Solute concentration of the liquid at the interface [mole fr.], see equation (2.0), page 22

c_p	Molar heat capacity of the melt, see equation (2.9), page 24
C_s	Concentration profile in the solid, see equation (2.4), page 23
$C_s(t)$	Instantaneous solute concentration in the solid at the interface, see equation (6.2), page 129
C_S^*	Solute concentration of the solid at the interface [mole fr.], see equation (2.0), page 22
C_∞	Solute concentration of the melt at an infinite distance from the interface, see equation (2.2), page 23
D	Mass diffusion constant of the liquid, see equation (2.2), page 23
D_0	Theoretical maximum diffusion coefficient at infinite temperature [m^2/s], see equation (4.12), page 78
E_d	Activation energy for diffusion [J/mol], see equation (4.12), page 78
E_i	Exponential integral function, see equation (2.10), page 25
$F(A)$	Stability function, see equation (2.35), page 31
f_l	Fraction of sites in the liquid monolayer for an atomic jump, see equation (6.3), page 130

f_s	Fraction of sites in the solid monolayer for an atomic jump, see equation (6.2), page 129
G	Conductivity-weighted average temperature gradient ahead of the tip, see equation (2.32), page 30
g	Contour of the paraboloid of revolution geometry, see equation (2.7), page 24
G_c	Concentration gradient in the liquid, see equation (2.31), page 30
G_l	Thermal gradient in the liquid, see equation (2.36), page 32
G_s	Thermal gradient in the solid, see equation (2.36), page 32
i	Chemical species, see equation (3.1), page 59
I_v	Ivantsov function, see equation (2.11), page 25
K	Curvature [m^{-1}], see equation (2.27), page 29
k	Nonequilibrium partition coefficient, see equation (2.43), page 34
k_0	Equilibrium partition coefficient, see equation (2.21), page 28
K_l	Thermal conductivity of the liquid, see equation (2.36), page 32
K_s	Thermal conductivity of the solid, see equation (2.36), page 32
m_L	Liquidus slope [K/mole fr.], see equation (2.19), page 27

m'_L	Kinetic liquidus slope, see equation (2.54), page 38
P	System pressure, see equation (3.1), page 59
P_c	Solutal Péclet number, see equation (2.13), page 25
P_t	Thermal Péclet number, see equation (2.12), page 25
R	Universal gas constant equal to 8.314 J/mol·K, see equation (2.51), page 37
r	Radius of curvature at the dendrite tip [m], see equation (2.0), page 22
T	System temperature, see equation (3.1), page 59
T^*	Interface temperature [K], see equation (2.0), page 22
T_L	Liquidus temperature, see equation (2.14), page 26
T_l	Temperature profile in the liquid, see equation (2.1), page 23
T_s	Temperature profile in the solid, see equation (2.3), page 23
T_∞	Temperature of the melt at an infinite distance from the interface, see equation (2.2), page 23
T_{m1}	Melting temperature of pure component represented by 1, see equation (2.51), page 37
V	Axial growth rate of the solid-liquid interface [m/s], see equation (2.0), page 22

V_0	Maximum crystallization velocity of the melt at infinite driving force, see equation (2.52), page 37
V_D	Diffusive speed [m/s], see equation (6.16), page 133
x	Composition given in molar fractions [mol.fr.], see equation (3.1), page 59

References

1. M. C. Flemings, editor. *Solidification Processing*. McGraw-Hill, New York, 1974.
2. J. Lipton, W. Kurz, and R. Trivedi. Rapid dendrite growth in undercooled alloys. *Acta Metallurgica*, 35:957–964, 1987.
3. R. Trivedi, J. Lipton, and W. Kurz. Effect of growth rate dependent partition coefficient on the dendritic growth in undercooled melts. *Acta Metallurgica*, 35:965–970, 1987.
4. B. J. Boettinger, S. R. Coriell, and R. Trivedi. Application of dendritic growth theory to the interpretation of rapidly solidified microstructures. In R. Mehrabian and P. A. Parish, editors, *Rapid Solidification Processing Principles and Technologies IV*, pages 13–25. Claitor's Publishing Division, Baton Rouge, LA, 1988.
5. A. G. DiVenuti and T. Ando. A dendrite growth model accomodating curved phase boundaries and high Péclet number conditions. *Metallurgical and Materials Transactions A*, 29A:3047–3056, 1998.
6. W. Kurz and D. J. Fisher. *Fundamentals of Solidification*. Trans Tech Publications Ltd, Switzerland, 4th revised edition, 1998.
7. J. W. Christian. *The Theory of Transformations in Metals and Alloys*. Pergamon, 3rd edition, 2002.
8. K. A. Jackson. A review of the fundamental aspects of crystal growth. In H. S. Peiser, editor, *Crystal Growth*, pages 17–24. Pergamon Press Ltd., 1st edition, 1967.
9. J. Lipton, M. E. Glicksman, and W. Kurz. Dendritic growth into undercooled alloy melts. *Materials Science and Engineering*, 65:57–63, 1984.
10. G. P. Ivantsov. Temperature field around spherical, cylindrical, and needle-shaped crystals which grow in supercooled melts. *Dokl. Akad. Nauk SSSR*, 58:567–569, 1947.
11. G. P. Ivantsov. *Dokl. Akad. Nauk SSSR*, 83:573–576, 1952.

12. G. P. Ivantsov. Thermal and diffusion processes in crystal growth. In *Growth of Crystals*, volume 1, pages 76–85. Consultants Bureau, New York, NY, 1958.

13. W. Kurz and D. J. Fisher. Dendrite growth at the limit of stability: Tip radius and spacing. *Acta Metallurgica*, 29:11–20, 1981.

14. R. Trivedi. Morphological stability of a solid particle growing from a binary alloy melt. *Journal of Crystal Growth*, 48:93–99, 1980.

15. J. Lipton, M. E. Glicksman, and W. Kurz. Equiaxed dendritic growth in alloys at small undercooling. *Metallurgical Transactions A*, 18:341–345, 1987.

16. R. Trivedi and W. Kurz. Morphological stability of planar interface under rapid solidification conditions. *Acta Metallurgica*, 34:1663–1670, 1986.

17. J. C. Baker and J. W. Cahn. The thermodynamics of solidification. In *Solidification*, chapter 2, pages 23–58. ASM, Metals Park, OH, 1971.

18. J. C. Baker and J. W. Cahn. Solute trapping by rapid solidification. *Acta Metallurgica*, 17:575–578, 1969.

19. D. Turnbull and B. G. Bagley. Transitions in viscous liquids and glasses. In *Treatise on Solid State Chemistry*, volume 5, pages 513–554. Plenum Press, New York, NY, 1975.

20. M. Suzuki, T. J. Piccone, M. C. Flemings, and H. D. Brody. Solidification of highly undercooled Fe-P alloys. *Metallurgical Transactions A*, 22A:2761–2768, 1991.

21. S.-G. Kim, S.-H. Shin, T. Suzuki, and T. Umeda. Numerical analysis of the rapid solidification of gas-atomized Al-8 wt pct Fe droplets. *Metallurgical and Materials Transactions A*, 25A:2815–2826, 1994.

22. G. X. Wang, V. Prasad, and S. Sampath. An integrated model for dendritic and planar interface growth and morphological transition in rapid solidification. *Metallurgical Transactions A*, 31:735–746, 2000.

23. T. Ando. A review of dendritic growth models and their applications. Internal document, Northeastern University, April 2001.

24. G. P. Ivantsov. Thermal and diffusion processes in crystal growth ii. In *Growth of Crystals*, volume 3, pages 53–60. Consultants Bureau, New York, NY, 1962.

25. J. S. Langer and H. Müller-Krumbhaar. Stability effects in dendritic crystal growth. *Journal of Crystal Growth*, 42:11–14, 1977.

26. J. S. Langer and H. Müller-Krumbhaar. Theory of dendritic growth - I. Elements of a stability analysis. *Acta Metallurgica*, 26:1681–1687, 1978.

27. J. S. Langer and H. Müller-Krumbhaar. Theory of dendritic growth - II. Instabilities in the limit of vanishing surface tension. *Acta Metallurgica*, 26:1689–1695, 1978.

28. J. S. Langer and H. Müller-Krumbhaar. Theory of dendritic growth - III. Effects of surface tension. *Acta Metallurgica*, 26:1697–1708, 1978.

29. W. W. Mullins and R. F. Sekerka. Stability of a planar interface during solidification of a dilute binary alloy. *Journal of Applied Physics*, 35:444–451, 1964.

30. M. J. Aziz. Model for solute redistribution during rapid solidification. *Journal of Applied Physics*, 53:1158–1168, 1982.

31. A. J. C. Wilson. Binary equilibrium. *Journal of the Institute of Metals*, 70:543–556, 1944.

32. W. J. Boettinger, U. R. Kattner, S. R. Coriell, Y. A. Chang, and B. A. Mueller. Development of multicomponent solidification micromodels using a thermodynamic phase diagram data base. In *Modeling of Casting, Welding and Advanced Solidification Processes VII*, pages 649–656, London, UK, 10-15 September 1995.

33. U. Kattner, W. J. Boettinger, and S. R. Coriell. Application of Lukas' phase diagram programs to solidification calculations of multicomponent alloys. *Zeitschrift fur Metallkunde (Germany)*, 87:522–528, July 1996.

34. S. H. Perepezko and W. J. Boettinger. Use of metastable phase diagrams in rapid solidification. In *Materials Research Society Symposia Proceedings*, volume 19, pages 223–240, 1983.

35. J. H. Perepezko. Kinetic processes in undercooled melts. *Materials Science and Engineering A*, 15:374–382, 1997.

36. J. L. Murray. Calculation of the stable and metastable equilibrium diagrams of Ag-Cu and Cd-Zn systems. *Metallurgical Transactions A*, 15A:261–268, 1984.

37. M. Binnewies and E. Milke. *Thermochemical Data of Elements and Compounds*. WILEY-VCH, 1999.

38. C. T. Heycock and F. H. Neville. Complete freezing point curves of binary alloys containing Silver or Copper together with another metal. *Philos. Trans. Royal Society (London) A*, 189:25–69, 1897. As shown in Reference [39].

39. P. R. Subramanian and J. H. Perepezko. The Ag-Cu (Silver-Copper) system. *Journal of Phase Equilibria*, 14(1):62–75, 1993.
40. P. Duwez, R. H. Willens, and W. Klement, Jr. Continuous series of metastable solid solutions in Silver-Copper alloys. *Journal of Applied Physics*, 31:1136–1137, 1960.
41. J. H. Hildebrand. Solubility. XII. Regular solutions 1. *Journal of American Chemical Society*, 51:66–80, 1929.
42. J. B. Thompson, Jr. Thermodynamic properties of simple solutions. In P. H. Abelson, editor, *Researches in Geochemistry*, volume 2, pages 340–361. Wiley, New York, NY, 1967.
43. C. H. P. Lupis and J. F. Elliott. Prediction of enthalpy and entropy interaction coefficients by the "central atoms" theory. *Acta Metallurgica*, 15:265–276, 1967.
44. C.H.P. Lupis. *Chemical Thermodynamics of Materials*. John Willey, 2nd edition, 1983.
45. P. Venkataraman. *Applied Optimization with Matlab Programming*. John Wiley & Sons, Inc., New York, 2002.
46. A. Biran and M. Breiner. *Matlab 5 for Engineers*. Addison-Wesley, 1999.
47. P. M. Pardalos and M. G. C. Resende, editors. *Handbook of Applied Optimization*, chapter Nonlinear Programming. Oxford University Press, Inc., New York, 2002.
48. O. Axelsson. On global convergence of iterative methods. In *Iterative Solution of Nonlinear Systems of Equations*, pages 1–19, 1982.
49. W. Hackbusch. Multi-grid solution of continuation problems. In *Iterative Solution of Nonlinear Systems of Equations*, pages 20–45, 1982.
50. M. D. Greenberg. *Advanced Engineering Mathematics*. Prentice Hall Inc., 2nd edition, 1998.
51. K. A. Jackson and B. Chalmers. Kinetics of solidification. *Canadian Journal of Physics*, 34:473–490, 1956.
52. K. A. Jackson. Kinetics of alloy solidification. *Canadian Journal of Physics*, 36:683–691, 1958.
53. W. G. Pfann. Segregation of two solutes, with particular reference to semiconductors. *Journal of Metals*, 4:861–865, August 1952.

54. A. A. Chernov. Excess impurity trapping during crystal growth. *In Growth of Crystals, edited by A. V. Shubnikov and N. N. Sheftal (Consultants Bureau, New York)*, 3:35–39, 1962.

55. M. J. Aziz. An atomistic model of solute trapping. In R. Mehrabian, editor, *Rapid Solidification Processing Principles and Technologies III*, pages 113–117. Claitor's Publishing Division, Baton Rouge, LA, 1982.

56. M. J. Aziz. Interface attachment kinetics in alloy solidification. *Metallurgical and Materials Transactions A*, 27A:671–686, 1996.

57. M. J. Aziz. Tests of theories for nonplanar growth during rapid alloy solidification. In *Solidification Processes and Microstructures: A Symposium in Honor to Wilfred Kurz*, 2004.

58. J. A. Kittl, P. G. Sanders, M. J. Aziz, D. P. Brunco, and M. O. Thompson. Complete experimental test of kinetic models for rapid alloy solidification. *Acta Materialia*, 48:4797–4811, 2000.

59. M. J. Aziz and T. Kaplan. Continuous growth model for interface motion during alloy solidification. *Acta Metallurgica*, 36:2335–2347, 1988.

60. J. C. Brice. *The Growth of Crystals From the Melt*, chapter 2, page 65. John Wiley & Sons, Inc., New York, 1965.

61. M. Hillert. Solute drag, solute trapping and diffusional dissipation of gibbs energy. *Acta Materialia*, 47:4481–4505, December 1999.

62. R. Abbaschian and W. Kurz. Diffuse solid-liquid interfaces and solute trapping. In *Solidification Processes and Microstructures: A Symposium in Honor to Wilfred Kurz*, 2004.

63. J. W. Cahn. Theory of crystal growth and interface motion in crystalline materials. *Acta Metallurgica*, 8:554–562, 1960.

64. J. W. Cahn, W. B. Hillig, and G. W. Sears. The molecular mechanism of solidification. *Acta Metallurgica*, 12:1421–1439, 1964.

65. R. T. DeHoff. *Thermodynamics in Materials Sience*. McGraw-Hill, Inc., 1993.

66. D. R. Gaskell. *Introduction to the Thermodynamics of Materials*. Taylor & Francis, 3rd edition, 1995.

67. M. Abramowitz and I. A. Stegun, editors. *Handbook of Mathematical Functions*. Dover, 3rd edition, 1965.